6-24-2015

Indentation Behavior of Multilayer Al/SiC Thin Films

Ryan Jamison

Ryan Dale Jamison

Candidate

Mechanical Engineering

Department

This dissertation is approved, and it is acceptable in quality and form for publication: *Approved by the Dissertation Committee:*

Prof. Yu-Lin Shen, Chair

Prof. Mehran Tehrani, Member

Prof. Rafiqul Tarefder, Member

Dr. Jordan Massad, Member

Indentation Behavior of Multilayer Al/SiC Thin Films

by

Ryan Dale Jamison

B.A., Chinese, University of Utah, 2008
B.S., Mechanical Engineering, University of Utah, 2008
M.S., Mechanical Engineering, University of Utah, 2008

DISSERTATION

Submitted in Partial Fulfillment of the
Requirements for the Degree of

Doctor of Philosophy
Engineering

The University of New Mexico

Albuquerque, New Mexico

April 2015

Dedication

For my wonderful wife, Evelyn, and beautiful daugher, Amelia.

Acknowledgments

I would like to express my gratitude to Howard Walther, Dr. Channy Wong, and Dr. Diane Peebles for their support. They encouraged me to pursue a Ph.D. and, without their guidance and help, this would have not been possible.

I would also like to offer my appreciation to my adviser, Professor Yu-Lin Shen, who has patiently guided me during my research. He has offerred valuable advice and guidance through my time at the University of New Mexico. I would also like to thank my committee members: Professor Mehran Tehrani, Professor Rafiqul Tarefder, and Dr. Jordan Massad for giving of their time and knowledge. Furthermore, I would like to thank Harold Madsen (UNM MTTC) as well as my fellow graduate students, Nekoda van de Werken, Ali Nematollahisarvestani, and Abir Hossain, for their assistance in performing experimental measurements.

None of this would be possible without the support of my family. I would like to thank my parents for instilling in me a desire to learn. Most importantly, I would like to express my deepest appreciation for my wife. Without her constant encouragement and support, I would not have been able to accomplish all I have.

Sandia National Laboratories is a multi-program laboratory managed and operated by Sandia Corporation, a wholly owned subsidiary of Lockheed Martin Corporation, for the U.S. Department of Energy's National Nuclear Security Administration under contract DE-AC04-94AL85000.

Indentation Behavior of Multilayer Al/SiC Thin Films

by

Ryan Dale Jamison

B.A., Chinese, University of Utah, 2008
B.S., Mechanical Engineering, University of Utah, 2008
M.S., Mechanical Engineering, University of Utah, 2008

Ph.D., Engineering, University of New Mexico, 2015

Abstract

Nanoindentation is useful for evaluating the mechanical properties, such as hardness and Young's modulus, of bulk and thin film materials. Multilayer thin films are an important subset of materials in which alternating layers of two or more materials are deposited on a substrate. Fabrication of multilayer films can result in imperfect layer geometry, particularly the flatness and thickness of each layer. Traditional nanoindentation techniques alone cannot provide insight into the microstructure of each layer. The finite element method is used to investigate the behavior of multilayer aluminum/silicon carbide thin film composites with imperfect internal geometry when subjected to various loadings. Undulating layered geometry is subjected to various loading scenarios, and the response of the structure is measured. The indentation-derived hardness and modulus are shown to be sensitive to the presence of undulating layers and the relative size of the indenter to the undulation. The amount of equivalent plastic strain in the Al layers also increases in the presence of undulating layers.

These multilayer films exhibit interesting and complex mechanical behavior under indentation type loading and unloading. The derivation of Young's modulus from nanoindentation testing assumes elastic unloading. It is shown that multilayer thin films may not unload elastically, altering the indentation-derived modulus result. The cyclic behavior of the multilayer thin film is studied in relation to the influence of unloading-induced plasticity. It is found that several cycles are required to minimize unloading-induced plasticity. Lastly, the effect of indentation-induced damage on derived hardness and modulus of multilayer films is investigated.

Contents

List of Figures

Glossary

P	Indentation load
h	Indentation displacement
A	Projected contact area
S	Contact stiffness at the onset of unloading
H	Hardness
E	Young's modulus
ν	Poisson's ratio
h_c	Contact depth
E_{eff}	Effective modulus
β	Indenter geometry parameter

Chapter 1

Introduction

Multilayer coatings consisting of alternating ductile metal and high-strength ceramic thin films can possess superior mechanical properties, such as high toughness and high damage tolerance, and thus have been a subject of intensive research [1–11]. Mechanical characterization of thin film and coating materials relies primarily on nanoindentation. However, complexity arises when the indentation technique is applied to multilayer thin films. This is due to the high degree of heterogeneity pertaining to the soft/hard arrangement along with the large interface areas. The deformation field will be different from that of a homogeneous thin film. Internal damage may also be induced by the indentation loading itself [10, 12–14].

1.1 Research Motivation

Nanoindentation of multilayer thin film systems is a useful method to determine the hardness and elastic modulus of a thin film composite. The traditional method, developed by Oliver and Pharr [15], used to derive these quantities assumes that the system remains perfectly elastic during unloading. The assumption of elastic unloading has

been shown to be valid for many thin film applications [16]. Though the assumption of elasticity appears valid for these applications, it is believed that composites of alternating hard and soft layers exist that do not unload elastically. Finite element analysis of a multilayer thin film structure [17] has shown that during unloading the plastic strain actually increases in the metallic layers. This computationally observed phenomenon shows that the unloading-induced plasticity can affect the derived multilayer modulus. Furthermore, the material combinations and geometry variations can affect the unloading-induced plasticity. The focus of this dissertation will be to explore these statements using both computational and experimental methods.

Layer geometry can vary in multilayer thin film applications; therefore, it is important to understand how these changes can affect the response of the structure. Figure 1.1 is an example of aluminum (Al)/silicon carbide (SiC) multilayer thin film with imperfect layer geometry. In this figure, it can be seen that each layer is not perfectly flat and varies in profile. Also, the individual layer thickness can vary as a design parameter or because of geometric tolerances during manufacturing. It is believed that the flatness and thickness of the layers in the internal geometry of a multilayer thin film will influence the indentation-derived elastic modulus and hardness.

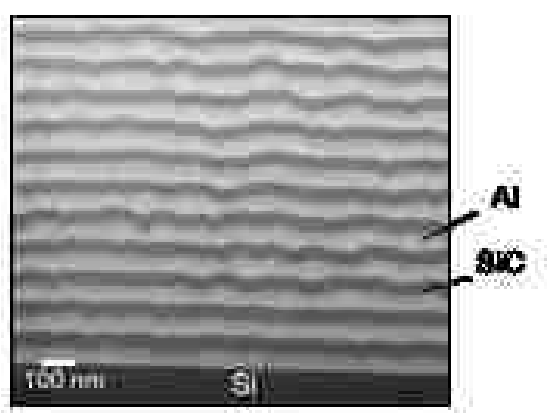

Figure 1.1: Cross-section of Al/SiC multilayer thin film on a Si substrate [18].

In a multilayer thin film application, not only does the geometry affect the indentation-derived response but also the material selection. In many thin film composites, the composite is made up of alternating layers of hard and soft materials, typically a brittle ceramic and a ductile metal, respectively. Under nanoindentation loading, the interaction of the hard and soft layers results in increased stress in the soft layers. Particularly, during unloading, the stiff elastic response of the hard layers can lead to an increase in plastic strain in the soft layers. As part of this study, it is desired to determine what material combination, if any, can alleviate or eliminate the increase in plastic strain during unloading. Undoubtedly, changes to the material combination will have an effect on the response of the composite.

In the microelectronic industry, designers are rarely interested in the single cycle response of their devices. Typically, electronics and microelectronics must function and survive in environments that are cyclic in nature such as vibration and variations in temperature. Structural coatings in machine components, including MEMS devices, may also need to experience repeated contact loads. Cyclic nanoindentation, in which the indenter is cycled between a fixed maximum and minimum load, is a useful method to help understand how these types of devices respond to recurring loads. Previous experimental and computation analysis [19] has shown that in hard/soft material system, the loading-unloading response is a recurring open loop in force-displacement space. In this study, the effect layer geometry and material combination have on the cyclic response is particularly of interest. Variations in layer geometry and material combinations will affect the cyclic response of the composite.

Figure 1.2 shows the post-indent cross section of an Al/SiC multilayer thin film. In the figure, arrows indicate areas where internal damage has occurred between layers. In this particular sample, cracks occur between the Al/SiC layers and at the Al/substrate interface. Currently, it is not clear how internal damage, such as in Figure 1.2, affects hardness and indentation-derived elastic modulus. Cracking

in metals and ceramics is a means of energy dissipation for the system; therefore, it is believed that the occurrence of internal damage will influence the indentation response of the system.

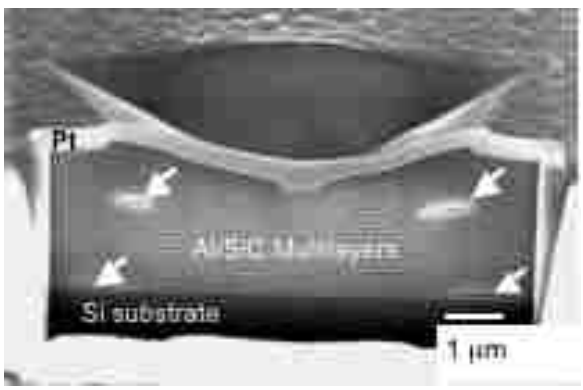

Figure 1.2: Post-indent, cross-sectional image showing internal damage under the indentation in the Al/SiC nanolayers. Cracks in the mid-layer region and at the multilayers/substrate interface, as highlighted, are visible [17].

Throughout many engineering applications and naturally occurring systems, hard and soft materials are combined into composite materials that use the advantages of both materials. Gaining further insight into the physics of the hard/soft material combinations can aid both engineers and scientists in many fields. In the field of engineering, understanding the effect of waviness in the layers will be beneficial for designers of these systems. This information can help them understand the potential changes in the stiffness of the structure and other variabilities in the system. In the field of biology, being able to better understand the sensitivities of these systems will allow scientists and engineers to design superior products. Gaining further insight into the behavior of hard/soft composites will allow the medical community to better understand bone behavior and performance under various loads.

1.2 Overview

The purpose of this dissertation is to address several open questions regarding the performance of multilayer thin films under nanoindentation loading. These questions include the dependence of indentation-derived variables to imperfect layer geometry, variations in film thickness, unloading-induced plasticity, and unloading-induced damage. These topics form the basis of this dissertation research. Both finite element models and experimental techniques are used to elucidate the dependence of indentation-derived variables on these parameters. This document consists of three publication-quality papers as well as supplemental information and analyses. The remainder of the document will proceed as follows.

Section 1.3 of the current chapter provides a high-level overview of the computational and experimental methods used in this study. Following this chapter, Chapter 2 is a review of the related literature. The review covers the history and development of the nanoindentation technique as well as variations and improvements to the technique. A brief history of thin films and their development is provided. The state of Al/SiC research is reviewed and discussed. Lastly, a brief review of cohesive zone fracture modeling is provided.

Chapter 3 provides a basis for evaluating the sensitivity of the indentation-derived variables to variations in geometry and material response. Finite element simulation results for homogeneous, single-layer films and multilayer thin films are presented. The results in this chapter represent nominal geometry and material behavior. Also, this chapter will present results of variations in material selection in a multilayer composite. The subsequent chapters will be variations on these results.

The first dependence presented is that of the effect of layer undulation on the measured hardness and derived modulus of a multilayer thin film. Layer undulation is believed to affect the indentation measured hardness and derived elastic modulus

of the thin film laminate. Varying the thickness of the hard or soft layers will change the effective volume ratio of the hard and soft materials. This will affect the response of the structure. It is also believed that the changes in layer thickness will affect unloading-induced plasticity. Specifically, it is believed that increasing the thickness of the hard layers will lead to an increase in the plasticity in the soft layers. Chapter 4 presents results of studies performed to understand the effect of layer undulation. Through extensive study of multilayer Al/SiC films, it has been observed that the nanoindentation unloading step is not purely elastic. This dissertation aims to determine if the presence of unloading-induced plasticity affects the indentation-derived film properties. It is believed that the presence of unloading-induced plasticity will affect the derived elastic modulus of a multilayer thin film. Through the currently proposed parametric numerical study, it is believed that the effect can be quantified. This may pave the way for devising a procedure to extract the effective elastic modulus of the multilayer composite using indentation unloading even when plastic deformation occurs in the soft layers. Chapter 5 presents results associated with this analysis.

Chapter 6 will present results on how the presence of internal damage affects the indentation response of the thin film composite. The presence of internal damage is believed to lead to hardness and modulus predictions that are lower than those predictions without internal damage. Internal cracks will provide energy dissipation in the system, effectively requiring less force for the same amount of indentation.

Concluding remarks and future work are presented in Chapters 7 and 8, respectively. Results of a preliminary study of the sensitivity of indentation-derived variables to layer thickness is presented in Appendix A. The study includes varying the SiC thickness while maintaining a constant Al film thickness. Indentation-derived hardness and Young's modulus are presented as well as an analysis of unloading-induced plasticity.

Preliminary results from the experimental efforts associated with this work, including single-layer and multilayer film fabrication, are presented in Appendix B.

1.3 Approach

This research effort will focus on the computational aspect of understanding unloading-induced plasticity with supporting experimental work. The finite element method is a useful tool for gaining further insight into how and why plasticity in metal layers may develop during the unloading process. Experimental methods currently are not capable of providing such information during the unloading process as only post-test imaging is available. To test the effect that unloading-induced plasticity has on the derived modulus of the multilayer thin film, a variety of finite element models will be used. All variations will be based on a thin film nanolaminate that is composed of 41 alternating layers of Al and SiC where each layer is 50 nm thick. These 41 layers are on top of a thick silicon (Si) substrate. This model will serve as a good basis for comparison because there exists a body of work that has analyzed this geometry.

Two variations to the model described above will be used to focus on the unloading-induced plasticity. In the first model, all three materials (soft layers, hard layers, and substrate) will have the same elastic modulus. The Al will remain as elastic–plastic with its inherent yield stress and hardening characteristics. The SiC will be assumed elastic perfectly plastic with a yield stress that is equal to one-third the hardness of the material. The Si substrate will remain elastic. This model will serve to relax the internal mechanical constraint imposed on the Al by the stiff Si and SiC. Since the layers and substrate materials have the same elastic modulus, the modulus value can thus be retrieved from the unloading response during indentation if there is no plasticity involved. Any deviation from the known modulus value should be

a consequence of unloading-induced plasticity. Quantification of its effect will be possible through these proposed parametric analyses.

The aim of the second model will be to force the unloading response to be elastic. The Oliver and Pharr method assumes the unloading process is elastic, but previous analysis has shown that plastic deformation can occur during unloading. This second model will, by design, enforce the elasticity assumption during unloading. The loading step of this model will be an exact match to the baseline model. During the unloading phase, the yield stress of both the Al and SiC will be made artificially large to prevent any further yielding in these materials. This will allow for a direct comparison between the baseline model, which allows for unloading-induced plasticity, and a model in which the unloading step is guaranteed elastic. The calculated hardness and derived modulus from this second model can then be compared with the derived parameters from the baseline model, thus providing further understanding of the impact of unloading-induced plasticity.

The variation in the flatness of the individual layers of a multilayer thin film will be considered using a similar finite element model as described above. To simulate the undulated layer geometry, two regular waveforms of the SiC layers are considered in the multilayer thin film. The free surface of the topmost Al film and the interface with the Si substrate are kept perfectly flat. The two waveforms considered are 180° out-of-phase and are referred to as the 'crest' and 'trough' models (see Chapter 4). These labels refer to the point on the wave that is at the symmetry axis, i.e. the crest of the waveform of the SiC layer is at the symmetry axis in the 'crest' model, and similar for the 'trough' model. For each of these two models, each waveform has 60 cycles in the lateral direction, which is equivalent to a wavelength of 0.67 μm. The amplitude of each waveform varies from 10% to 50% of the thickness of a single SiC layer. In addition to the undulating layers, the original flat geometry will be modified such that the thicknesses of the layers vary. The layer thickness will be modified in

terms of a ratio of SiC thickness to Al thickness and will vary between 0.2, 1.0, and 5.0. The total thickness of the specimen will remain constant.

The multilayer thin film nanolaminate used as a baseline in this research is one with alternating layers of Al and SiC on a Si substrate. In order to determine the dependence of the response to material selection, the SiC layers will be replaced with silicon dioxide (SiO_2) layers. Silicon dioxide is less stiff than SiC and will provide a useful material combination to evaluate the response of the hard-soft combination common in nanolaminates. Also, the model with the SiO_2 layers will also provide further information about unloading-induced plasticity as it will relax the material constraint on the Al caused by the more stiff SiC.

Modeling the cyclic response of the various permutations of the multilayer thin films will provide information about the unloading-induced plasticity in the Al layers. Analysis of the cyclic response will include the repeated loading and unloading of the multilayer thin film between a set maximum load and 10% of the maximum load. The load/unload cycle will be completed until a stabilized hysteresis loop is obtained. The baseline model with the nominally flat layers, a model with the undulating layers, and the model with SiO_2 will have cyclic loading applied.

Post-indentation analysis of multilayer composites has shown that delamination is possible under a nanoindentation-type loading. This phenomenon can only be observed after the fracture has already taken place. Finite element analysis can provide a means to study how and when any delamination occurs between the hard and soft layers in a multilayer composite. To capture the internal damage caused by layer delamination, interfacial cohesive zone elements will be used between the hard and soft layers. Cohesive zone elements follow the traction-separation law. These elements are capable of mixed mode failure, taking into account both tensile and shear stresses. By incorporating the possibility of damage into the indentation models,

quantitative insight can be gained into the effect of damage on elastic modulus and hardness measurements.

Lastly, a series of experiments of the Al and SiC thin films will be conducted. Monolayer Al and SiC specimens will be fabricated using magnetron sputtering on a Si substrate. Each film will be nominally 1 μm thick. In addition to the single-layer films, a multilayer Al/SiC film will be fabricated. The fabricated sample will have 41 alternating layers of Al and SiC (similar to the previously described finite element model), each 50 nm thick. The hardness and Young's modulus of both single-layer and multilayer films will be measured using nanoindentation. Furthermore, nanoindentation will be used to measure the cyclic response of the multilayer Al/SiC film.

Chapter 2

Review of Related Literature

2.1 Nanoindentation Technique

Scientists have been studying material response to indentation since the 19th century. Boussinesq [20] and Hertz [21] developed a mathematical model for computing the stress and displacement response of an elastic body loaded by a rigid indenter. Hertz showed how two elastic spherical bodies react when placed in contact. His theories provided a mathematical framework that was later used by Sneddon to analyze the material response of a rigid indenter into an elastic material. Sneddon [22] was able to show that the load-displacement relationship for a variety of simple punch geometries is given by:

$$P = \alpha h^m \tag{2.1}$$

where P is the indenter load, h is the elastic displacement of the indenter, and α and m are material constants. This model assumes that both the loading and unloading steps of the indentation process remain elastic. This relationship has thus proved to be one of the cornerstones of the modern day experimental indentation techniques.

Many scientists were able to further develop models based on Sneddon's work and increase the understanding of indentation. Pogodin-Alekseyev [23] was able to determine the hardness and elastic modulus of a homogeneous isotropic elastic material. Doerner and Nix [24] further improved methods for analyzing the data obtained from indentation experiments to obtain material hardness and elastic modulus. Specifically, Doerner and Nix determined that the contact area remains unchanged as the indenter is unloaded, which allowed for a more accurate measurement of the contact area. As experimental sensing and measuring techniques improved, the methods used to analyze indentation data were continually scrutinized and studied. Oliver and Pharr [15] developed an improved set of experimental techniques and methods to use indentation data to calculate the material hardness and modulus.

The method that Oliver and Pharr developed involves the analysis of the loading and unloading curves typically generated by an indentation test (Figure 2.1). To calculate the hardness, H, of the material, the classical form of the hardness is used

$$H = \frac{P_{max}}{A} \tag{2.2}$$

where P_{max} is the peak indentation load and A is the projected contact area of the impression. Methods to determine the contact area have been studied rigorously [25, 26], and the appropriate technique is dependent on indenter geometry, indenter material, and target material. Determining the contact area at peak load can be difficult to do; therefore, the contact area is determined analytically. The projected contact area is given by

$$A = F(h_c) \tag{2.3}$$

where F is a functional form that must be determined experimentally and h_c is the contact depth. The projected contact area of a perfect Berkovich indenter is:

$$A(h_c) = 24.5h_c^2 \tag{2.4}$$

and can be used as an initial estimate of the contact area. These relationships allow for the determination of the material hardness. The indentation-derived elastic modulus

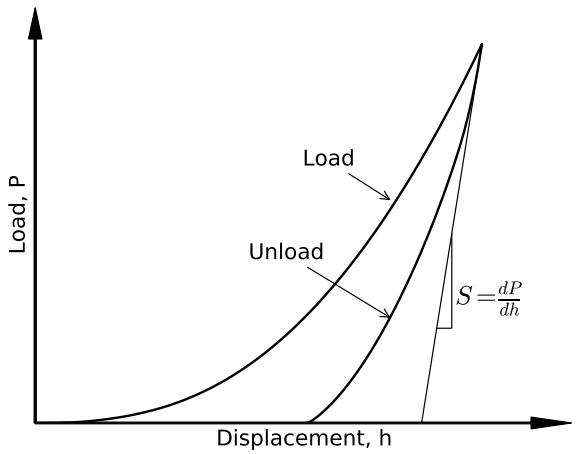

Figure 2.1: Typical indentation load-displacement curve.

of the material is calculated from the analysis of the initial unloading stiffness, S. The initial unloading stiffness, or contact stiffness, was developed by Sneddon and is given as

$$S = \frac{dP}{dh} = \frac{2}{\pi} E_{eff} \sqrt{A} \tag{2.5}$$

where E_{eff} is the effective modulus. It was subsequently discovered that Sneddon's relationship describing the contact stiffness regularly over predicted the elastic modulus by as much as 13% [27,28] To correct for this discrepancy, a constant, β, was included with Sneddon's equation:

$$S = \frac{dP}{dh} = \beta \frac{2}{\pi} E_{eff} \sqrt{A} \tag{2.6}$$

The constant is a function of indenter geometry and specimen material. The value of β is commonly between 1.0 and 1.13. This version of the stiffness relationship is now commonly used for both experimental and computational indentation analysis.

The effective modulus can subsequently be used to calculate the modulus of the test specimen. To account for a non-rigid indenter, Tabor et al. [29,30] proposed the

use of the effective, or reduced, modulus, which is defined as

$$\frac{1}{E_{eff}} = \frac{1-\nu^2}{E} + \frac{1-\nu_i^2}{E_i} \tag{2.7}$$

where E and ν are Young's modulus and Poisson's ratio of the specimen, and E_i and ν_i are the Young's modulus and Poisson's ratio of the indenter. The contact stiffness can be measured experimentally from the initial portion of the unloading data. Once the contact stiffness is measured, Equation 2.6 can be solved for E_{eff}, and Equation 2.7 can be solved for the Young's modulus of the specimen.

Though the contact stiffness, S, can be derived from experimentally obtained load-displacement data, Oliver and Pharr found that the equation given by Sneddon (Equation 2.1) was not sufficient to accurately describe the unloading behavior of many materials. Originally, Sneddon's relationship assumes that a straight line will fit the unloading data. Oliver and Pharr found that when using a straight line fit for nonlinear unloading data, the magnitude of the contact stiffness depends on how much of the unloading data is used in the calculation. Oliver and Pharr observed that the nonlinear unloading data could be described by a power law relationship given as

$$P = C\left(h - h_f\right)^m \tag{2.8}$$

where C and m are constants and h_f is the elastic component of the displacement. These three variables, C, m, and h_f, are calculated from a least squares fitting of the unloading data. This relationship can then be analytically differentiated at the peak load to determine the initial unloading stiffness. Since the inception of this relationship, this is the most commonly used experimental method to calculate the stiffness at the onset of unloading from the indentation load-displacement data.

Further studies conducted by Bolshakov et al. [31] have shown that the relationship describing the unloading behavior proposed by Oliver and Pharr is accurate for both elastic and elastic-plastic alloys as well as other materials. They also proposed the

idea of an effective indenter shape, which is described analytically with a power law relationship. Pharr, Bolshakov, and Oliver [16, 32] further elaborated on the concept of an effective indenter shape. Finite element simulations of elastic-plastic materials with a rigid conical indenter with half-angle of 70.3° showed that during loading the shape of the contact impression matches the shape of the indenter perfectly. For elastic-plastic materials, during unloading the shape of the impression is not perfectly conical but has a slight convex curvature. During reloading, the projected contact area will gradually increase, causing the unloading data to have a nonlinear shape.

The concept of an effective indenter shape was developed in an effort to address the assumption of elastic unloading. During the loading process, both elastic and plastic deformation occurs below the indenter. Therefore, since Sneddon's model assumes elastic unloading, it is important to know if plasticity occurs during unloading. Pharr and Bolshakov [16] showed that for a homogeneous elastic-plastic material unloading-induced plasticity has no significant effect on the shape of the unloading load-displacement curve, hence little influence on the derived modulus. The importance of the assumption of elastic unloading will be discussed further in Chapter 5.

2.2 Expanding the Nanoindentation Paradigm

Classical nanoindentation techniques discussed above are all based on the assumption of an infinite, homogeneous, isotropic half-space with no surface roughness and a perfect indenter (both geometry and material). Ever since Oliver and Pharr published their technique for analyzing indentation load-displacement data, they and other researchers have been investigating which factors or conditions might influence indentation-derived material properties. These areas of research include thin film nanoindentation, cyclic indentation, residual stresses, extraction of material stress-strain curves, statistical methods associated with indentation, and finite element error

analysis. Though these areas of interest are only a sample of the many aspects of nanoindentation extensively studied over the last two decades and a half, these are some of the most pertinent to the current research.

Today the most common use of indentation is to measure mechanical properties of thin film materials. Pharr [33] and Whitehead [34] were among the first to use indentation techniques to measure mechanical properties of thin films. Indentation is a useful technique because of the relatively small size of both the indenter and thin film geometries. Though indentation is commonly used for thin films, a potential source of error is the presence of the film substrate. Methods to address the substrate effect on indentation load-displacement response have been studied extensively. Wei and Zhang [35] developed a simple method to extract both the film and substrate modulus from a single indentation test. They proposed a method that extracts the moduli through statistical curve fitting of the semilogarithmic composite elastic modulus against the indentation depth normalized by the film thickness. Zhou and Prorok [36,37] also proposed a method to account for the substrate effect by modifying the discontinuous elastic interface transfer method. This allows for the use of both the Oliver and Pharr method and does not require the continuous stiffness method, such that any indenter can be used. Though methods exist for addressing the substrate stiffness, they are not commonly used and are not used in this dissertation.

Cyclic indentation is an extended technique to extract material information that may not be observable through single indentation analysis. Oliver and Pharr determined that best practice is to load and unload the indenter multiple times to minimize the possible effect of plastic unloading [15]. This practice has been shown to work well for homogeneous materials or single-layer thin films. When conducting nanoindentation on a normal material, such as a homogeneous elastic-plastic solid, one encounters both elastic and plastic deformation during loading. The elastic strains are recovered in the unloading phase. If the specimen then is cyclically reloaded and

unloaded, the load-displacement curve will follow the prior unloading path, which characterizes the elastic nature of the process [38, 39]. While this is true for most homogeneous elastic-plastic solids and single-layer thin films, it does not always hold true for multilayer thin films. Previous studies have shown that for a multilayer structure the unloading and reloading response is different and results in a hysteretic response [19, 40, 41]. The hysteresis of the load-displacement curve suggests the continual increase in plasticity during both the unloading and reloading phases.

It is common in thin-film materials, as well as bulk materials, that a residual stress is present from the manufacturing process. For example, when manufacturing thin-films, the thermal mismatch between the film and the substrate can lead to residual stress in the material system. LaFontaine et al. [42] showed that the presence of residual stress in a thin-film could affect the indentation-derived hardness by as much as a factor of 2. Inspired by LaFontaine's work, Pharr et al. [43] used both experimental and finite element methods to evaluate the effect of residual stress on both hardness and elastic modulus. It was found that the presence of large compressive residual stresses promotes the pile-up near the indentation site, while tensile residual stresses will decrease pile-up. Therefore, to account for the presence of residual stress, the contact area must be accurately measured.

Tsui and Bolshakov [44, 45] expanded on the work of Pharr in a series of publications that systematically evaluated the effect of residual stress on indentation based results. They confirmed Pharr's findings that residual stress has the most impact on the indenter contact area. They showed that the established relationships defining the contact area, such as Equation 2.4, underestimate the contact area. They found that the contact area could be measured accurately using optical methods. Most significantly, when the proper contact area is used, the residual stress has little effect on the hardness and modulus. As compressive stress is common in thin films, it

was also shown that compressive stresses have the least effect on indentation-derived properties.

Furthermore, Singh et al. [46] showed that for an Al/SiC material system, i.e. the system of interest in this dissertation, the residual stress developed during the fabrication process is largely compressive. This compressive stress is dependent on both the number of alternating material layers as well as layer thickness. The stress state in the Al layers is mostly compressive due to a peening mechanism that occurs when SiC and Argon neutrals bombard the Al during deposition. Since the residual stress in the Al/SiC multilayer were shown to be largely compressive, residual stresses are ignored in the finite element models presented in this dissertation.

The residual stress in the test specimen is just one of many sources of potential error in nanoindentation techniques. In an effort to address size effects in the material, or composite, being tested Constantinides et al. [47] proposed the use of statistical methods. He proposed performing a large number of single indentation tests in a grid and analyzing the resulting hardness and modulus using statistical methods. This method can provide the in situ elastic properties of the test specimen. This technique has been applied to many types of homogeneous and composite materials with good success [48]. This method could be useful when investigating the nanoindentation response of multilayer films where uncertainty remains in geometry and material composition.

Typically nanoindentation has been used to extract the elastic modulus and hardness of a material. Martinez et al. [49] developed a method in which the load-displacement data from a nanoindentation experiment can be converted into an "indentation stress-strain curve." They found that by converting load-displacement data from nanoindentation that the stress-strain behavior of chromium nitride/chromium multilayer coatings could be accurately described. This method has been expanded to include many other materials [50], particularly those materials and composites

that can be described using a power-law hardening material model. Liu et al. [51] expanded on Martinez's work and developed a finite element method (FEM) deconvolution method to more accurately determine the properties of films on substrates. This method uses an iterative method to match FEM results to experimental load-displacement data by optimizing the hardening behavior of the material model input. This technique would allow for a better characterization of the materials considered in this dissertation.

Since the development of the Oliver and Pharr method, finite element analysis has been used to further study nanoindentation. Many of the papers cited above involve the use of the finite element method to elaborate on or enhance the knowledge gleamed from experiments. Though FEM is regularly used to study nanoindentation, as it is in this dissertation, there has not been extensive error analysis performed. To address this lack of information, Kashani [52] performed a rigorous study of the errors associated with the finite element analysis of nanoindentation. He showed that the discretization of the continuum is the key contributor to the accuracy of the finite element predictions. He showed that the contact area increases in discrete jumps as contact changes from element to element. He showed that as the discretization becomes coarser, the hardness prediction continues to increase, as the contact area is not accurately resolved. Also, it was shown that the error associated-convergence tolerance of the finite element solver, i.e. too loose of a tolerance, has little effect on the overall solution and is small compared to discretization error. Results from a mesh convergence study are presented later in this dissertation.

2.3 Thin Films

Thin films have been used in many applications for more than a century. Thin films are single-layers of homogeneous material, or multilayers of more than one material,

that range in thickness from less than a nanometer to several micrometers. As early as 1858, Julius Plucker [53] created a "beautiful metallic mirror" using an early sputtering process to deposit platinum film inside a discharge tube. Since then, a multitude of scientists and engineers have created new applications for thin films and inventing new methods for creating thin films. Today, the most common applications for thin films are in the electronic semiconductor and optical coatings industries and scientists have also began applying thin films to pharmaceuticals.

Single-layer and multilayer thin films have many advantageous properties over macroscale homogeneous materials. They can be designed to have higher strength, durability, toughness, oxidation resistance, and a variety of other mechanical, thermal, or optical traits. In nature, a great example of a thin film is nacre (Figure 2.2), an organic-inorganic composite material that is strong, resilient, and iridescent. Meyers, et al. conducted an extensive study on the structure and properties of biological materials, including many films [54]. There are many examples of multilayer coatings consisting of alternating ductile metal and high-strength ceramic that exhibit superior mechanical properties such as high toughness and high damage tolerance [1–11].

Figure 2.2: Example of natural nacre on a nautilus cutaway [55].

2.3.1 Physical Vapor Deposition

Thin films can be fabricated by chemical deposition, such as plating or chemical vapor deposition, or by physical deposition, such as thermal evaporation or sputtering. Both of these deposition methods originated in the middle of the 20th century. Holland documented the method, then known only as vapor deposition, as early as 1956 [56]. Powell, Oxley, and Blocher coined the term "physical vapor deposition" and "chemical vapor deposition" to differentiate between the two types of deposition methods in 1966 [57]. Since that time, many scientists and engineers have continued to study and hone these techniques for thin film fabrication.

Physical vapor deposition (PVD), perhaps the most common of the two, is a deposition method in which the condensation of a vaporized form of the material is deposited onto a substrate. There are multiple PVD methods used in thin film fabrication and for this dissertation the focus will be on sputtered thin films. There are multiple advantages to sputtered thin films over other methods. Materials with high melt temperature can be easily sputtered compared to evaporation methods. Sputtered films have composition similar to the source material. These films also typically have better adhesion to the substrate material than evaporated films. The most significant disadvantage is that it is difficult to combine sputtered films with lift-off processes to control film structuring.

A simplified schematic of the sputtering process is shown in Figure 2.3. The major components of a magnetron sputtering system consist of a vacuum chamber that contains a substrate for film growth, the sputtering target, and a sputtering gas (e.g. Argon). The method works by creating gaseous plasma from the gas and accelerating the plasma ions into the target material. When the plasma ions impact the target, the target is eroded and material is ejected in the form of neutral particles into the

sputtering chamber. These particles travel in a straight line. When these particles contact the substrate, they coat the substrate, forming a thin film.

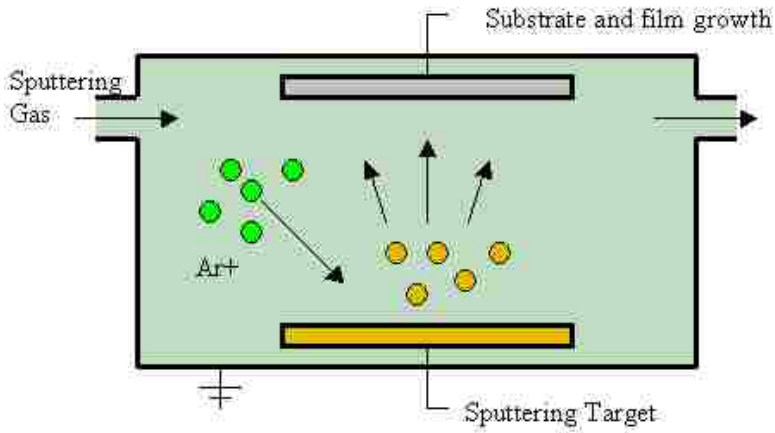

Figure 2.3: Graphical example of magnetron sputtering [58].

2.3.2 Aluminum and Silicon Carbide

There are many materials, and combinations of materials, that are used in thin film applications. In this dissertation, the focus will be on two materials: polycrystalline Al and amorphous SiC, in single-layer and multilayer films. Generally, the multilayer Al/SiC thin film is deposited on a Si substrate and this generality holds true for all further discussion in this chapter. Amorphous SiC has been shown to have applications in optoelectronic devices, solar cells, and high-temperature engineering materials [59]. Together, Al/SiC multilayer thin films are effective as reflective coatings in extreme ultraviolet (EUV) applications. Magnetron sputtered Al/SiC composites exhibit low residual stress, good temporal and thermal stability, and provide good performance in EUV such as monochromatic solar imaging [60].

The mechanical performance of Al/SiC multilayer composites has been studied extensively. Deng, et al. were among the first to fabricate and study the mechanical

behavior of the Al/SiC multilayer using nanoindentation [9]. Aluminum and SiC were deposited using DC and RF magnetron sputtering, respectively. They showed that the Young's modulus of the Al and SiC nanolayer thin films is significantly lower than the macroscale homogeneous material. Furthermore, the Young's modulus of the composite structure is greater than the pure Al layer. Deng, et al. also studied the mechanical properties of both thin film Al and SiC, independently and together [61]. By depositing thin films of each material on Kapton, microtensile tests were performed on both single and multilayer composites of Al and SiC. The stress-strain response of pure Kapton can be subtracted from the response of the composite and thin film tensile properties extracted.

Tang, et al. performed further research on the effective elastic modulus of the Al/SiC multilayer composite for different volume fractions [62]. Using Hooke's law and the rule of mixtures, the modulus of the multilayer composite in the longitudinal and transverse directions was calculated. The Young's modulus obtained from these calculations was compared to the modulus obtained from finite element nanoindentation calculations. It was found that at indentation depths past 8 layers, the indentation-derived modulus and the transverse modulus of the composite were consistent. Tang, et al. also evaluated the stress distribution in the multilayer composite and found that large volumes of the composite exhibit axial tension due to the mismatch in material properties. Lotfian, et al. further evaluated the effect of volume fraction, or relative layer thickness, and temperature on the Al/SiC multilayer mechanical response [63]. At elevated temperatures, the hardness for all volume fractions decreased rapidly due to deformation mechanisms activated at high temperatures. The scratch resistance [64] and residual stress [46], as discussed above, has also been thoroughly researched for the Al/SiC multilayer composite.

Additional research into the nanoindentation response of Al/SiC multilayer composites has been performed over the last few years. Wen and Shen evaluated the

plastic deformation in the Al/SiC multilayer during indentation unloading using a viscoplastic material response [65]. To account for different unloading rates and dwell periods, the Al was modeled as a viscoplastic material. They found that a dwell time would remove any time-dependency during the unloading. Though time-dependency is removed, plastic deformation still occurs in the Al during unloading. Shen, et al. also considered the cyclic behavior of the Al/SiC multilayer [19]. The presence of unloading-induced plasticity results in an open hysteresis load-displacement response. Furthermore, the plasticity in the Al layers continues to increase during each subsequent cycle. This increase in plasticity is due to the mechanical constraint placed on the Al by the SiC layers.

The mechanical constraint between the Al and SiC not only causes unloading-induced plasticity but also can result in damage during the indentation process. Chawla, et al. used experimental techniques to observe the fracture behavior of the Al/SiC multilayer [10]. Samples were sectioned using focused ion beam (FIB) techniques and scanning electron microscopes (SEM) to visualize the cross section. It was observed that the layers exhibit roughness, or waviness, that is caused by the columnar grain structure of the Al. Extensive pile-up was observed caused by bending in the SiC and plasticity in the Al. The FIB showed localized cracking in the SiC and void nucleation and growth in the Al.

Sun, et al. [12] expanded on Chawla's work using transmission electron microscopy. They found that no cracks were present in the as-deposited specimens. After indentation, cracking and bending were confirmed in the SiC layers and delamination between the multilayer/Si substrate. They also confirmed Chawla's finding that the Al/SiC interface exhibits greater strength than does pure material. Lastly, Singh, et al. used FIB tomography to visualize the post-indentation damage [18]. They confirm that the otherwise brittle SiC exhibits very high flexibility and that any localized SiC damage occurs due to large shear stresses built up during indentation.

They were able to observe the shape of cracking in the SiC, void growth in the Al, and delamination between the multilayer and Si. Due to potential delamination, the strength of the interfaces has been studied.

In the Al/SiC multilayer system, there are two interfaces to be considered, Al to SiC and Al to Si. Luo, et al. performed perhaps the earliest study on the behavior of the Al/SiC interface [66]. Using molecular dynamics, they showed that the Al/C interaction is stronger than the Al/Si interface. When combined, the structural bonding is limited to a narrow region near the interface and the structure is similar to that of nanocrystalline Si. Lastly, they showed that the interface is insensitive to variation in the orientation of the atoms, meaning the interface is stable regardless of imperfect orientation. More recently, Dandekar, et al. conducted molecular dynamics simulations to obtain a traction-separation relationship for the Al/SiC interface in both tension and shear loading [67]. They observed that the interface is strong and that ductile failure in the Al largely contributes to deformation of the interface.

Similar to the studies performed on the Al/SiC interface, the Al/Si interface has been modeled using both atomistic and molecular dynamic simulations. Gall, et al. studied the mechanical behavior of the Al/Si interface using atomistic simulation [68]. They developed a continuum fracture mechanics traction-separation relationship that is consistent with the modified embedded atom method (MEAM) simulation. They showed that the interface is dependent on the size and location of the defects near or at the interface. Ward, et al. also evaluated the Al/Si interface and nanocomposites using molecular dynamics. Ideally, the Al/Si interface has no other components but during the sputtering process, Al_2O_3 can form on the exposed Si. Therefore, the mechanical behavior of the Al_2O_3 interface is required. Dandekar, et al. studied the behavior of the Al/Al_2O_3 interface using a molecular dynamics approach [69]. They derived Mode I and II traction-separation relations for an Al/Al_2O_3 interface based on the amount of porosity in the bulk material and temperature.

2.3.3 Indentation-Induced Damage

Post-indentation analysis, as discussed above, of multilayer composites has shown that delamination, fracture, and/or damage are possible under a nanoindentation loading [70–72]. This phenomenon can only be observed after the fracture has already taken place. As discussed above, indentation-induced fracture and delamination has been studied experimentally for the Al/SiC multilayer thin film. Indentation-induced damage has also been studied for many other material systems, such as: Cr/CrN [73], Al/AlN [6], ZnO/Ag/ZnO [74], Al/TiN [75], thin films on ductile substrates [76], and oxide films [77]. For these systems, and other material combinations, delamination between layers is one of multiple possible failure mechanism. Though delamination is a possible failure mechanism under indentation loading, it is very difficult to study experimentally.

Finite element analysis can provide a means to study how and when any delamination occurs between the hard and soft layers in a multilayer composite. To capture the internal damage caused by layer delamination, interfacial cohesive zone elements can be used between the hard and soft layers. Needleman first introduced the concept of a traction-separation relationship [78]. In an effort to understand debonding in metal matrices from a continuum mechanics approach, Needleman suggested a linear model to address crack opening behavior. Tvergaard and Hutchinson expanded on Needleman's work to model crack growth resistance in homogeneous solids and along interfaces [79]. More recently, Park, et al. [80] has developed a potential based framework for modeling the traction-separation relationship across fracture surfaces.

Cohesive zone elements follow the traction-separation law [81]. Cohesive zone elements have an initial stiffness of K until a critical stress (T_{max}), or interface strength, at a displacement δ_0 is reached. After surpassing the interface strength, the elements are able to unload gradually with stiffness less than K until full separation

is reached at δ_{sep}. These elements are capable of mixed mode failure, taking into account both tensile and shear stresses. This capability has been used extensively in both academia and industry to study debonding under various loading conditions. In this dissertation, cohesive elements are used to model interlayer delamination and will be discussed further in Chapter 6.

Chapter 3

Nanoindentation Modeling Preliminaries

3.1 Introduction

Nanoindentation is an effective experimental technique for evaluating the mechanical properties of homogeneous and thin film materials. Experimental nanoindentation methods have been used for decades to study the hardness and elastic modulus of a variety of thin film systems. In this dissertation, a select subset of materials are considered, namely: 1 - homogeneous Al, 2 - Al film on a Si substrate, 3 - SiC on a Si substrate, 4 - multilayer Al/SiC films on a Si substrate, and 5 - multilayer Al/SiO_2 on a Si substrate. In this chapter, the nanoindentation behavior of each of these materials are studied using the finite element method. The results from these simulations act as a basis for variations to these material system described later in Chapters 4-6.

In Section 3.2 the material models for each of these systems is described. In Section 3.3 the nanoindentation behavior of homogeneous Al is discussed. In Section 3.4

the behavior of Al and SiC films on Si substrates are discussed. Section 3.5 discusses the nanoindentation response of multilayer Al/SiC and multilayer Al/SiO_2. Results of a mesh convergence study of the multilayer Al/SiC film is presented in Section 3.6. Lastly, Section 3.7 provides concluding comments on these material systems.

3.2 Model Description

Multiple finite element models were used to study the nanoindentation response of the material systems listed above. The homogeneous Al model is approximately 50 μm thick with no substrate. Both the Al and SiC thin film models consist of both 1.0 and 2.05 μm thick film on a thick Si substrate. The multilayer composites (Al/SiC and Al/SiO_2) have 41 alternating layers, each 50 nm thick, on a Si substrate. For both multilayer composites Al is the top most (in contact with the indenter) and the bottom most most (adjacent to the Si substrate) layer.

A conical diamond indenter with a semi-angle of 70.3° is assumed. This indenter geometry results in the same projected contact area for a given depth as that of a Berkovich indenter in common nanoindentation experiments. Use of the conical indenter is a practical way to model the indentation process in a two-dimensional setting [82]. Each model is axisymmetric with the left boundary being the symmetry axis. Each specimen is 40 μm in the lateral span (radius). A schematic of the multilayer thin film is shown in Figure 3.1. During deformation the left and bottom boundaries are allowed to displace only in the axial and radial directions,respectively. The right boundary is not constrained. The top surface of each specimen, when not in contact with the indenter, is also free to move. When contact with the indenter is established, the surface portion engaged by the indenter directly interacts with the indenter. The coefficient of friction between the indenter and the top surface is 0.1, which is a typical value for the diamond/metal contact surface [83, 84].

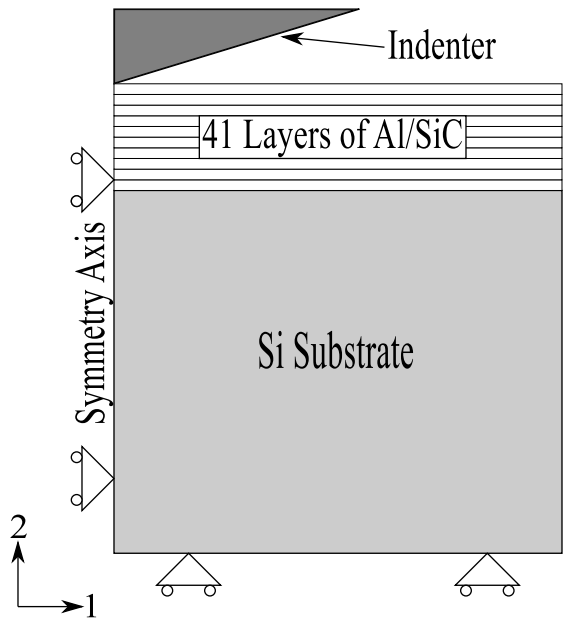

Figure 3.1: Schematic showing the Al/SiC laminates above a Si substrate and the boundary conditions used in the axisymmetric model. The left boundary is the symmetry axis. The entire specimen is 40 μm in lateral span (radius) and 43 μm in height. Each individual Al and SiC layers are 50 nm thick.

A total of 50,000 to 150,000 fully integrated linear axisymmetric elements are used in the finite element model with a finer mesh size near the upper-left corner of the test material (i.e. near the indenter). The element size near the indenter is approximately 6 nm and increases in size far from the indenter. The indenter consists of approximately 8,000 elements with an element size of approximately 10 nm near the tip. The mesh was created using CUBIT (Sandia National Laboratories; Albuquerque, NM). The finite element program ABAQUS (Version 6.13, Dassault Systemes Simulia Corp.; Providence, RI) was used to carry out the analysis.

The Young's modulus for Al is assumed to be 59 GPa. Nanoindentation of single-layer Al provided the modulus for this material. The Poisson's ratios for Al is 0.33. The plastic response of Al was based on the tensile loading data of single-layer

Al with initial yield strength of 200 MPa. Rate-independent isotropic elastic-plastic response was assumed with plastic yielding following the von Mises criterion with isotropic hardening and the incremental flow theory. The piecewise linear strain hardening response features hardening slopes of 199.33 MPa from initial yielding up to the strain of 50.51% and then 39.97 MPa up to the strain of 300.68%, beyond which perfect plasticity ensues.

The Young's modulus for SiC is assumed to be 277 GPa. Nanoindentation of single-layer SiC films provided the modulus. The somewhat lower modulus of SiC, relative to crystalline SiC (which is around 410 GPa), is due to the fact that the physical vapor deposited SiC layers in the present case were amorphous [61]. The Poisson's ratios for SiC is taken 0.17. SiC is a very brittle material; nevertheless, a very high yield point of 8,770 MPa (estimated from the indentation hardness of a single-layer SiC film [9] was used followed by perfect plasticity. This assumption is necessitated by the fact that a purely elastic SiC in the model will generate unrealistically high loads during the indentation simulation, and it is validated by the fact that in the experiment the SiC layers exhibited a glassy/plastic-type response due to the amorphous nature of the film [62].

SiO_2 is a brittle but less stiff material than SiC. The Young's modulus for SiO_2 is assumed to be 69 GPa. The modulus is derived from SiO_2 deposited on a Si substrate [85]. The Poisson's ratio is assumed to be 0.17. Similar to SiC, a very high "yield point" of 2,766 MPa (estimated from the hardness of single-layer SiO_2 on Si substrate) was used followed by perfect plasticity.

Both the Si substrate and diamond indenter are assumed to remain elastic. The Young's modulus and Poisson's ratio of the Si substrate are 187 GPa and 0.28, respectively. The Young's modulus and Poisson's ratio of the diamond indenter are 1,141 GPa and 0.07, respectively. All the interfaces between different materials in the composite structures are modeled as perfectly bonded.

The indentation-derived elastic modulus and hardness were directly obtained from the finite element modeling. The contact stiffness at the onset of unloading, S, is defined as:

$$S = \frac{dP}{dh} = \beta \frac{2}{\pi} E_{eff} \sqrt{A} \tag{3.1}$$

where A is the projected contact area at onset of unloading, β is the indenter geometry-dependent dimensionless parameter, and E_{eff} is the effective modulus. To calculate the contact stiffness at the onset of unloading from the finite element model, a least-squares linear regression is fitted to a portion of the unloading load-displacement data. In the current study, the initial 2% of the unloading curve (based on the peak load) is used to fit the linear regression.

The elastic modulus of the specimen can be calculated from the indentation-derived effective modulus. The effective modulus is defined as:

$$\frac{1}{E_{eff}} = \frac{1-\nu^2}{E} + \frac{1-\nu_i^2}{E_i} \tag{3.2}$$

where E and ν are the Young's modulus and Poisson's ratio, respectively, of the material being indented; and E_i and ν_i are the Young's modulus and Poisson's ratio, respectively, of the diamond indenter. In the simulation, the parameter β was first calibrated with a pure Al body of the same geometry as the specimens presented here, and a value of 1.06 was determined. This was accomplished by making certain the indentation-derived Young's modulus is equivalent to the input value used in the finite element analysis.

When calculating the projected contact area A, the last nodal point on the top surface in contact with the indenter was identified in the deformed mesh. From the last node in contact on the top surface, the radius of projected contact area can be measured. Thus, the effect of pileup was automatically taken into consideration. The determination of the composite modulus E requires a known Poisson's ratio ν. Here a separate finite element analysis of uniaxial loading of the Al/SiC laminates was used

to determine ν, which results in a value of 0.25. For homogeneous and single-layer films, the Poisson's ratio is as given above. Finally, the hardness, H, of the material is calculated from the quotient of the peak load at a given indentation depth and the projected contact area at the same depth. The Young's modulus and hardness are then calculated for various indentation depths.

3.3 Nanoindentation of Homogeneous Aluminum

The nanoindentation response of homogeneous Al is perhaps the most simple of the simulations considered in this dissertation. As described above, indentation of an approximately 50 μm thick homogeneous Al block with a diamond indenter was performed. Both the hardness and Young's modulus of the bulk material is presented. Experimental verification studies have also been performed and are documented in Appendix B.

Figure 3.2 shows the indentation-derived hardness of homogeneous Al. The hardness of the homogeneous film is calculated to be approximately 650 MPa. The assumed yield stress of Al, as described above, is 200 MPa, which is slightly lower than one-third of the derived hardness.

Figure 3.3 shows the indentation-derived Young's modulus of the homogeneous Al. For an indentation depth of 100 nm, the derived Young's modulus of the homogeneous Al is 60 GPa. This is the same as the modulus that was used as input to the model. At much deeper indentation depths, the modulus appears to be converging to approximately 68 GPa. The increase in modulus over indentation depth is due to the axial boundary condition at the bottom of the specimen. Though it is 'far' away, the presence of the boundary condition still affects the indentation-derived modulus.

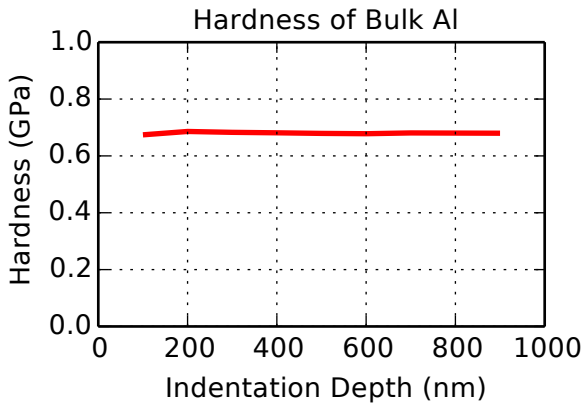

Figure 3.2: Indentation-derived hardness of homogeneous Al

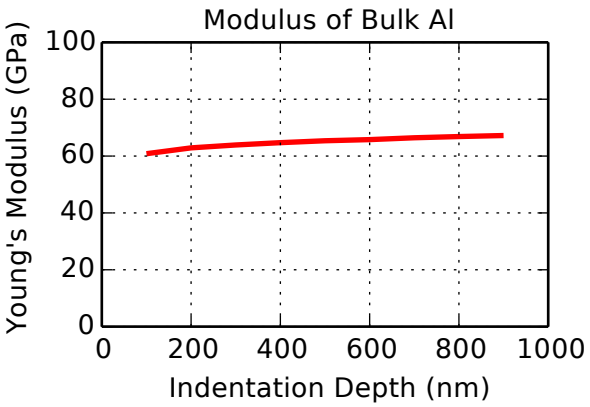

Figure 3.3: Indentation-derived Young's modulus of homogeneous Al

Both the indentation-derived hardness and Young's modulus are consistent with the Young's modulus and initial yield strength of Al used as input to the finite element model. The indentation response of an Al film on a Si substrate is considered next.

3.4 Nanoindentation of Thin Films

3.4.1 Aluminum Film

The indentation-derived hardness and Young's modulus of an Al film on a Si substrate is considered for two film thicknesses, 1.0 μm and 2.05 μm. Though the indentation response of the homogeneous Al matches the input parameters well, the presence of a stiff substrate can affect the indentation-derived results.

Figure 3.4 shows the indentation-derived hardness of thin film Al on a Si substrate as a function of normalized indentation depth. The indentation depth, h, is normalized by the film thickness, t. This normalization is consistent in all Al and SiC film figures. The hardness of the thin film Al is consistent with the homogeneous Al and is independent of film thickness. The difference in hardness at a normalized depth of 0.1 and 0.2 is believed to be due to small differences in the finite element mesh, resulting is slightly different projected contact areas.

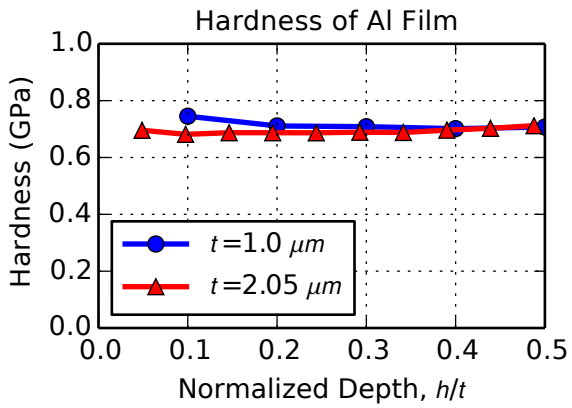

Figure 3.4: Indentation-derived hardness of thin film Al

Figure 3.5 shows the indentation-derived Young's modulus of thin film Al on a Si substrate as a function of normalized indentation depth. The modulus of the Al film is

very sensitive to the substrate effect for both film thicknesses. The modulus continues to increase as indentation depth increases. The substrate effect is well known to the indentation community and has been studied extensively (See Section 2.2). To derive the actual Al film modulus from indentation, more sophisticated methods of indentation data reduction may be used [33, 38].

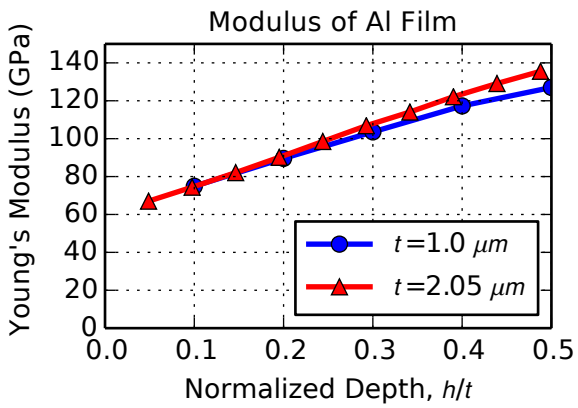

Figure 3.5: Indentation-derived Young's modulus of thin film Al

3.4.2 Silicon Carbide Film

The indentation-derived hardness and Young's modulus of a SiC film on a Si substrate is considered for two film thicknesses, 1.0 μm and 2.05 μm. The SiC is a much more stiff and brittle material than the Al and will exhibit different behavior under indentation loads.

Figure 3.6 shows the indentation-derived hardness of thin film SiC on a Si substrate as a function of normalized indentation depth. The indentation-derived hardness of the SiC film is 20 GPa, independent of indentation depth and film thickness.

Figure 3.7 shows the indentation-derived Young's modulus of thin film SiC on a Si substrate as a function of normalized indentation depth. For a film thickness

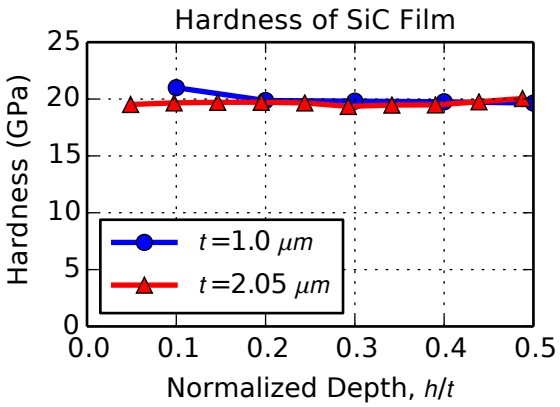

Figure 3.6: Indentation-derived hardness of thin film SiC

of 1.0 μm, the substrate does affect the indentation-derived SiC modulus. The Si substrate is actually less stiff than the SiC film. At deeper indentation depths, the less stiff substrate actually causes a decrease in the indentation-derived modulus. For the thicker film (2.05 μm), the derived modulus is 250 GPa and there is no significant substrate effect. This modulus is 10% lower than the assumed elastic modulus used in the SiC material model and may be attributed to the value assumed for β.

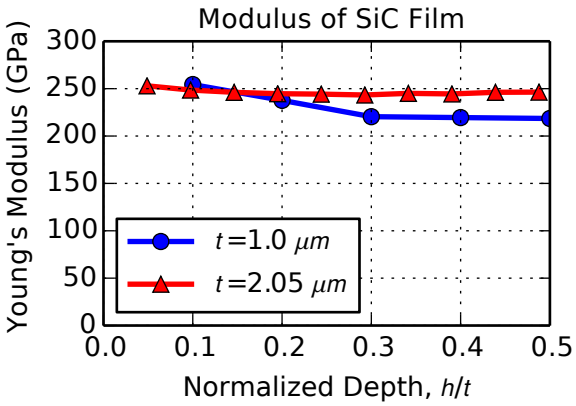

Figure 3.7: Indentation-derived Young's modulus of thin film SiC

3.5 Nanoindentation of Multilayer Thin Films

The nanoindentation response of multilayer thin films can be much more complicated than single-layer films or homogeneous materials. When loading multilayer films with a sharp indenter, the interaction between the layers can create interesting and complex stress fields throughout the film. Though this research is focused on the multilayer Al/SiC film, results for both multilayer Al/SiC and Al/SiO_2 films are shown here.

3.5.1 Aluminum/Silicon Carbide Multilayer Film

The history of the study of multilayer Al/SiC films is extensive and has been covered in Section 2.3.2. In this section, only the nanoindentation-derived hardness and modulus is presented. Further variations and discussions thereon are covered in subsequent chapters. Figure 3.8 shows the indentation-derived hardness of the multilayer Al/SiC film. The hardness of the multilayer Al/SiC exhibits a strong substrate effect. The hardness increases with indentation depth from 1.5 GPa to 6 GPa at 1000 nm. As expected, the multilayer hardness is much greater than the single-layer Al film and less than the SiC film. As the indentation depth increases, the number of SiC layers that affect the indentation data also increases.

Figure 3.9 shows the indentation-derived Young's modulus of the multilayer Al/SiC film. Similar to the single-layer Al film, the multilayer Al/SiC exhibits a strong substrate effect. The modulus increases with indentation depth up to 800 nm where it begins to slowly decrease with indentation depth. The complex behavior can be attributed to the interaction between the relatively soft Al and the much stiffer SiC in combination with existing substrate effect. Further analysis of the indentation-derived Young's modulus of the multilayer Al/SiC film is presented in Chapter 5.

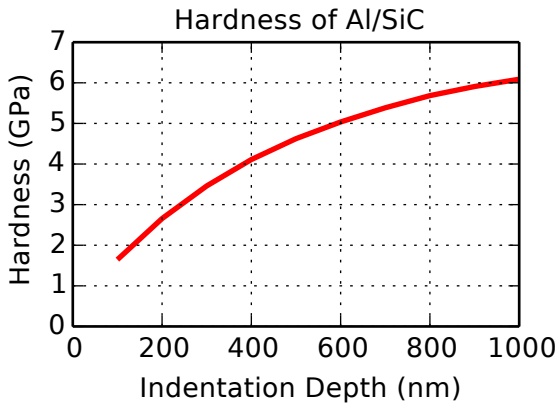

Figure 3.8: Indentation-derived hardness of Al/SiC multilayer film

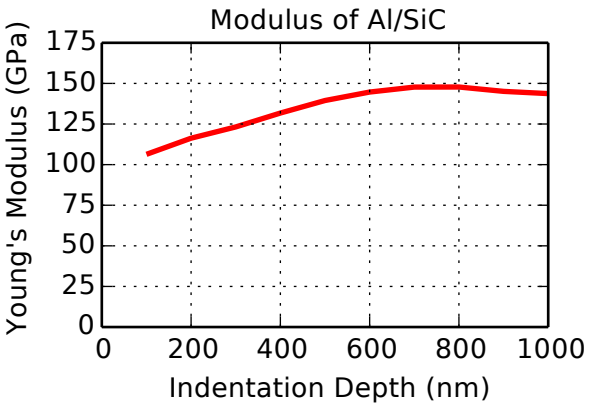

Figure 3.9: Indentation-derived Young's modulus of Al/SiC multilayer film

3.5.2 Aluminum/Silicon Dioxide Multilayer Film

Similar to multilayer Al/SiC, multilayer Al/SiO_2 can be used in a variety of applications. A common application for Al/SiO_2 is in anti-reflection coatings in optics [86]. Though SiO_2 is much tougher and more brittle than Al, it is nearly as stiff as Al. Combining SiO_2 with Al provides an interesting juxtaposition to the multilayer Al/SiC film. In the Al/SiO_2 film, each layer has nearly identical elastic modulus but the effective yield strength of each layer is very different. In this section, the indentation-derived hardness and Young's modulus is presented while further discussion of the

comparisons between the two multilayers can be found in Chapter 5. In this section, the finite element model used is identical to that shown in the previous section.

The indentation-derived hardness of multilayer Al/SiO_2 is shown in Figure 3.10. The hardness increases from 1.25 to nearly 3.0 GPa over the indentation range of 100 to 900 nm. The shape of the hardness curve is similar to that of the multilayer Al/SiC while the magnitude of the hardness is nearly half. As expected, though the moduli of the two materials are very similar, the difference in yield strength causes an increase in hardness.

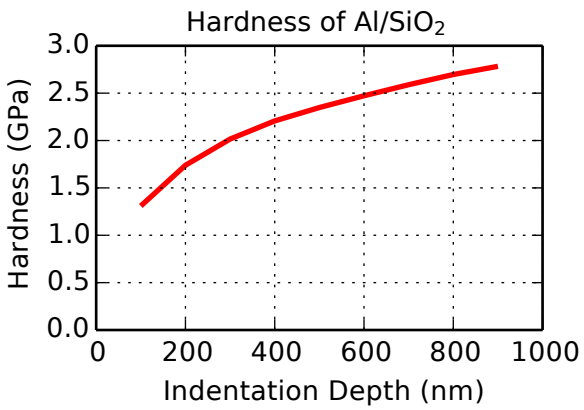

Figure 3.10: Indentation-derived hardness of Al/SiO_2 multilayer film

Figure 3.11 shows the indentation-derived Young's modulus of the multilayer Al/SiO_2 film. The derived modulus increases linearly from 70 to 120 GPa with indentation depth. The modulus at 100 nm is very close to the elastic modulus of the Al and SiO_2. At deeper indentation depths, the substrate effect becomes more prominent. Even though both materials have very similar elastic moduli, the substrate effect causes an increase in modulus with indentation depth.

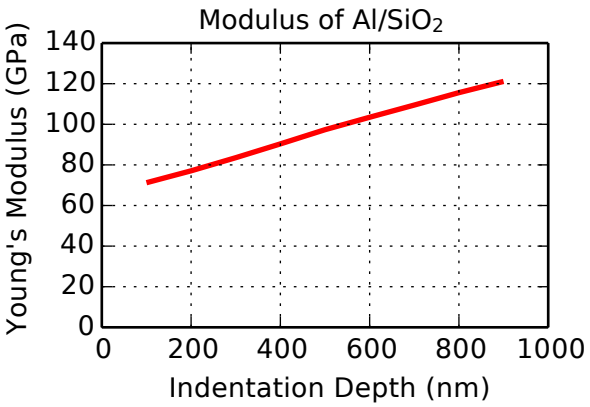

Figure 3.11: Indentation-derived Young's modulus of Al/SiO_2 multilayer film

3.6 Mesh Convergence of Multilayer Thin Film

Lastly, results for a mesh convergence study of the multilayer Al/SiC film are presented. Kashani showed that the projected contact area, along with other derived values, calculated from finite element simulations are subject to discretization error [52]. Furthermore, in the multilayer thin films, large deformation and material nonlinearities are present, both of which require a higher level of discretization.

To evaluate the convergence of the finite element solution as applied to the multilayer Al/SiC film, 5 models with increasingly fine meshes are considered. The most coarse mesh has two elements through the thickness of each layer near the indenter and only one element through each layer away (both radially and axially) from the indenter. The finest mesh has 10 elements through the thickness of each layer near the indenter and three elements through each layer away (both radially and axially) from the indenter. The smallest element edge length in each model (from most coarse to most fine) is 25 nm, 12.5 nm, 8.33 nm, 6.25 nm, and 5 nm. For each level of refinement, the smallest element edge length in the indenter near the tip is approximately twice that of the smallest in top layer. Furthermore, the aspect ratio,

as well as other elemental quality metrics, are consistent as the element edge length decreases.

The indentation-derived hardness of the multilayer Al/SiC for increasing levels of mesh refinement is shown in Figure 3.12. The only significant variation in derived hardness is for the least refined finite element mesh (25 nm). Nonetheless, there is only a small difference between the least and most refined mesh. Based on these results, a minimum edge length of 12.5 nm is sufficient to resolve the indentation-derived hardness.

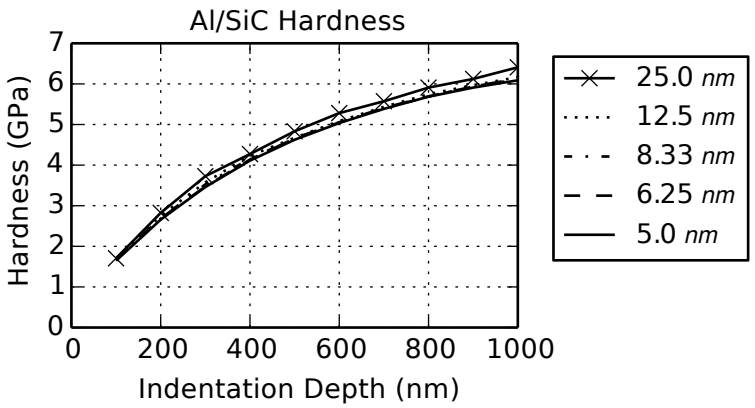

Figure 3.12: Indentation-derived hardness of multilayer Al/SiC film for various mesh refinement levels

The indentation-derived Young's modulus of the multilayer Al/SiC for increasing levels of mesh refinement is shown in Figure 3.13. Similar to the hardness, the only significant variation in derived modulus is for an element edge length of 25 nm. The modulus for models with a minimum element edge length of 12.5, 8.33, 6.25, and 5 nm are very similar.

Based on both the hardness and Young's modulus results, a minimum element edge length less than 12.5 nm is sufficient for resolving the indentation-derived variables.

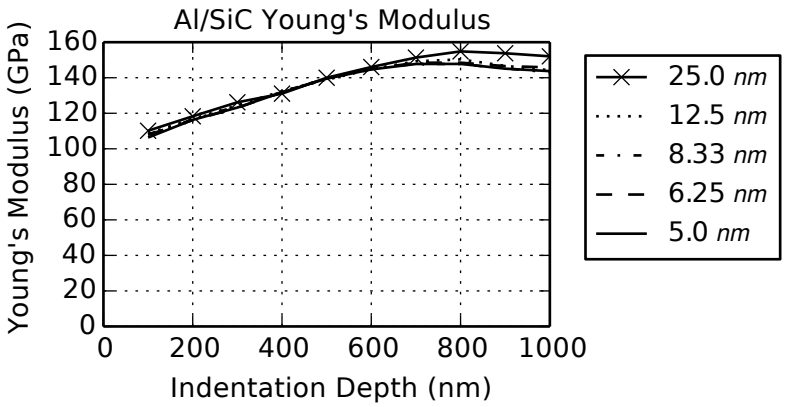

Figure 3.13: Indentation-derived Young's modulus of multilayer Al/SiC film for various mesh refinement levels

Nearly all results in this dissertation are from models with a minimum edge length of less than 6 nm; therefore, the error associated with discretization is minimized.

3.7 Conclusion

Indentation-derived hardness and Young's modulus of homogeneous Al, as well as, single-layer Al and SiC films was shown. The hardness of both films showed little substrate effect. The Young's modulus of the single-layer Al film exhibited a very strong substrate effect, while the much stiffer SiC film was shown to be independent of substrate effect. Indentation-derived results for multilayer Al/SiC and Al/SiO_2 were also presented. The hardness and modulus of both multilayer films increases with indentation depth. The multilayer Al/SiC film has a greater hardness and modulus than the Al/SiO_2 film. Both multilayer films presented here are susceptible to substrate effect. Lastly, mesh convergence was shown for the multilayer Al/SiC film. Based on the mesh refinement results, a minimum edge length of less than 12.5 nm, or a minimum of 6 elements through each layer, provides a sufficiently converged indentation-derived hardness and modulus.

Chapter 4

Indentation Behavior of Multilayered Thin Film Composites: Effect of Undulating Layer Geometry

The contents of Chapter 4 are based on two previously published manuscripts. Therefore, in an effort to preserve self-sufficiency, certain remarks and discussion also appear elsewhere in the dissertation manuscript.

4.1 Introduction

Multilayer coatings consisting of alternating ductile metal and high-strength ceramic thin films can possess superior mechanical properties such as high toughness and high damage tolerance, and thus have been a subject of intensive research [1–11, 60, 87]. Mechanical characterization of thin film and coating materials relies primarily

on nanoindentation techniques. However, complexity arises when the indentation technique is applied to multilayered thin films. This is due to the high degree of heterogeneity pertaining to/ the soft/hard arrangement along with the large interface areas. The deformation field will differ from that of a homogeneous thin film. Internal damage may also be induced by the indentation loading itself [10, 12–14, 73–75].

Numerical finite element analyses have been conducted on the Al/SiC nanolaminates to examine the internal deformation field and its correlation with the overall indentation response [17, 88]. It was found that a layered thin film structure responds to indentation loading in a complicated manner. Unique hardness and trustworthy elastic modulus values (derived from the indentation test) may not be obtained, even if the indenter penetrates deep into multiple layers [17]. Despite the predominant compressive stresses directly below the indentation contact, significant tensile stresses along the axial direction were found to exist at certain locations. The observed tensile stress helps to explain local fracture observed experimentally in post-indented specimens. Furthermore, plastic deformation in the Al layers continues to occur during the unloading phase of indentation modeling. This was attributed to the internal mechanical constraint resulting from the hard SiC layers in the composite as well as the development of a unique stress pattern within the layers. Although the finding was based on numerical modeling, it serves to raise awareness that in actual indentation testing the unloading process may no longer be considered simple elastic recovery as in a homogeneous material. The same study also concluded that when performing numerical modeling of indentation loading, it is important to incorporate the explicit multilayered structure rather than using a homogenized approach [17].

The present study seeks to extend the previous work and examine the effect of imperfect layer geometry on the nanoindentation response [89]. Specifically, we consider the undulating (wavy) appearance of the layers, which inevitably exists when at least one film material is of polycrystalline nature and the individual layer

thickness is in the nanometer range. Figure 4.1 shows an example of layered Al and SiC films above a Si substrate with the individual nominal film thickness of 50 nm [17]. The interfacial roughness is due to the newly deposited SiC following the surface contour of the underlying Al film, which has the columnar grain structure. How this layer undulation can quantitatively influence the indentation behavior is unknown and is the primary objective of this study. Numerical models of multilayer thin films with varying extents of undulation are considered and subjected to both uniaxial and nanoindentation loadings. Uniaxial loading of the multilayer thin films are used to provide a baseline understanding of the bulk response of the undulating structure to compressive loadings applied parallel and perpendicular to the layers. The indentation response and its associated internal deformation fields of the undulating thin films are investigated. Implications of the numerical findings to physical experimental measurements are also discussed.

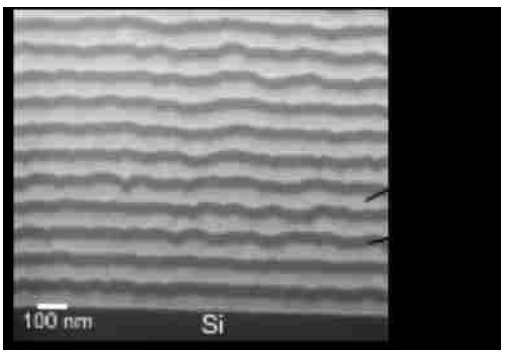

Figure 4.1: SEM Cross section of Al/SiC multilayer thin films on a Si substrate [17].

4.2 Model Description

4.2.1 Multilayer Thin Film Subjected to Uniaxial Loading

A schematic of the model used to study the effect of undulating layers on the bulk response of the multilayer thin films in compression is shown in Figure 4.2. A two-dimensional, generalized plane strain model is assumed, which accounts for a uniform deformation in the vertical direction. The sample is 3.0 μm wide and 3.05 μm thick consisting of 61 alternating layers of soft/hard material. The top and bottom layers are the soft material. The 61 layers are assumed to represent an 'infinite' multilayer film. Each layer is 50 nm thick, measured strictly along the 2-direction. The undulating layers are made from a regular waveform with amplitude of 25 nm, effectively half the thickness of each layer. The top and bottom layers both have perfectly flat free surfaces. The wavelength of the waveform is varied in the lateral direction (1-direction) between 60 nm and 667 nm (50 to 4.5 cycles in the lateral direction, respectively). The amplitude is left constant because previous simulations, not shown here, have shown little variation in elastic modulus for low amplitudes.

For these simulations, the soft material is assumed to be Al and the hard material is assumed to be SiC. The Young's moduli for Al and SiC are taken to be 59 GPa and 277 GPa, respectively. The Al and SiC modulus is lower than the bulk modulus as the thin film properties of both materials are lower than the bulk properties. Nanoindentation of single-layer Al and SiC films provided the moduli for these materials [61]. The somewhat lower modulus of SiC, relative to crystalline SiC (which is around 410 GPa), is due to the fact that the physical vapor deposited SiC layers in the present case were amorphous [61]. The Poisson's ratios for Al and SiC were taken as 0.33 and 0.17, respectively. The plastic response of Al was based on the tensile loading data of single-layer Al with initial yield strength of 200 MPa. Rate-independent isotropic elastic-plastic response was assumed, with plastic yielding following the von Mises

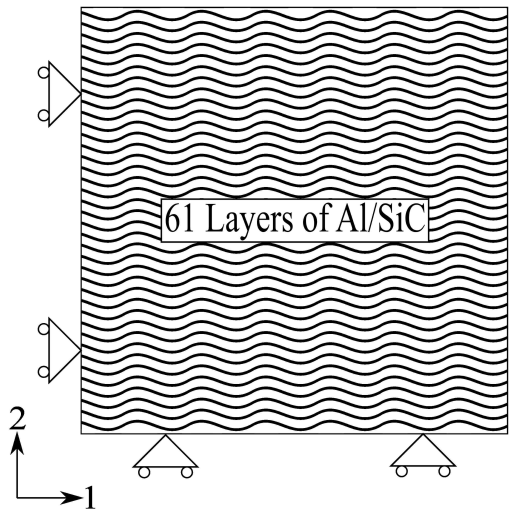

Figure 4.2: Schematic of thin film sample consisting of 61 alternating layers of Al (31 layers) and SiC (30 layers). The sample is 3.0 μm wide and 3.05 μm thick. Each layer is 50 nm thick. The amplitude of each layer is 25 nm.

criterion with isotropic hardening and the incremental flow theory. The piecewise linear strain hardening response features hardening slopes of 199.33 MPa from initial yielding up to the strain of 50.51% and then 39.97 MPa up to the strain of 300.68% beyond which perfect plasticity ensues [17]. SiC is a much more brittle material. Nevertheless, a very high yield point of 8,770 MPa (estimated from the indentation hardness of a single-layer SiC film) was used followed by perfect plasticity [9]. This assumption is necessitated by the fact that a purely elastic SiC in the model will generate unrealistically high loads during the simulation, and this is validated by the fact that in experiment the SiC layers exhibited a glassy/plastic-type response due to the amorphous nature of the film [12].

The left and bottom boundaries are fixed in the lateral and axial directions, respectively. The model is compressed 400 nm in both the lateral and vertical directions (independently), which is the equivalent of 8 layers in the vertical direction. A prescribed boundary condition is used to enforce the displacement. The model is meshed

with 10 elements through the thickness of each layer, resulting in approximately 1.4 million nodes and 1.4 million generalized plane strain elements. Simulations are performed using the commercial finite element code ABAQUS (Version 6.12, Dassault Systemes Simulia Corp., Providence, RI).

4.2.2 Multilayer Thin Film Subjected to Nanoindentation Loading

The finite element model used in the indentation analysis consists of 41 alternating Al and SiC thin films on a substrate of Si. This corresponds to the actual nanolayered system studied previously [17]. A schematic of the baseline model with a perfect geometry (no undulation) is shown in Figure 4.3. Both the top layer (to be in contact with the indenter) and the bottom layer (adjacent to the Si substrate) are Al. A conical diamond indenter with a semi-angle of 70.3° is assumed. This indenter geometry results in the same projected contact area, for a given depth, as that of a Berkovich indenter in common nanoindentation experiments. Use of the conical indenter is a practical way to model the indentation process in a two-dimensional setting [82]. The model is axisymmetric with the left boundary being the symmetry axis. The overall size of the entire specimen is 40 μm in lateral span (radius) and 43 μm in height. The thicknesses of the individual Al and SiC layers are 50 nm each. During deformation, the left and bottom boundaries are allowed to displace only in the axial and radial directions, respectively. The right boundary is not constrained. The top Al surface, when not in contact with the indenter, is also free to move. When contact with the indenter is established, the surface portion engaged by the indenter follows the frictional contact law. The coefficient of friction between the indenter and the top surface is 0.1, which is a typical value for the diamond/metal contact surface [83, 84]. It is assumed that the top layer Al remains intact and the indenter does not contact the SiC.

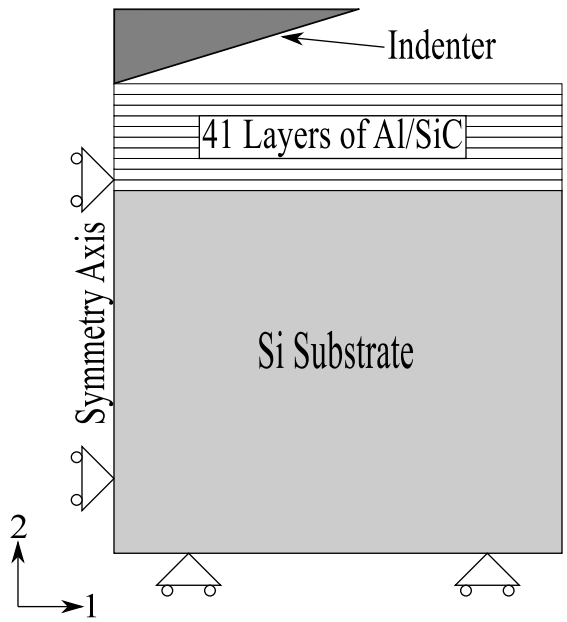

Figure 4.3: Schematic showing the Al/SiC laminates above a Si substrate and the boundary conditions used in the axisymmetric model. The left boundary is the symmetry axis. The entire specimen is 40 μm in lateral span (radius) and 43 μm in height. Each individual Al and SiC layers are 50 nm thick.

To simulate the undulated layer geometry, two regular waveforms of the SiC layers are considered in the multilayer part of the model shown in Figure 4.3. The free surface of the topmost Al film and the interface with the Si substrate are assumed to be perfectly flat. In reality, the topmost Al film very well may exhibit waviness, but it is made flat as a simplifying assumption. The two waveforms considered are 180° out-of-phase and are referred to as the 'crest' and 'trough' models. These labels refer to the point on the wave that is at the symmetry axis, i.e. the crest of the waveform of the SiC layer is at the symmetry axis in the 'crest' model and similar for the 'trough' model. For each of these two models, the wavelength in the lateral direction varies between 200 nm and 667 nm. Two amplitudes of the waveform are considered: 12.5 nm and 25 nm (or 25% and 50%, respectively, of the thickness of an individual layer).

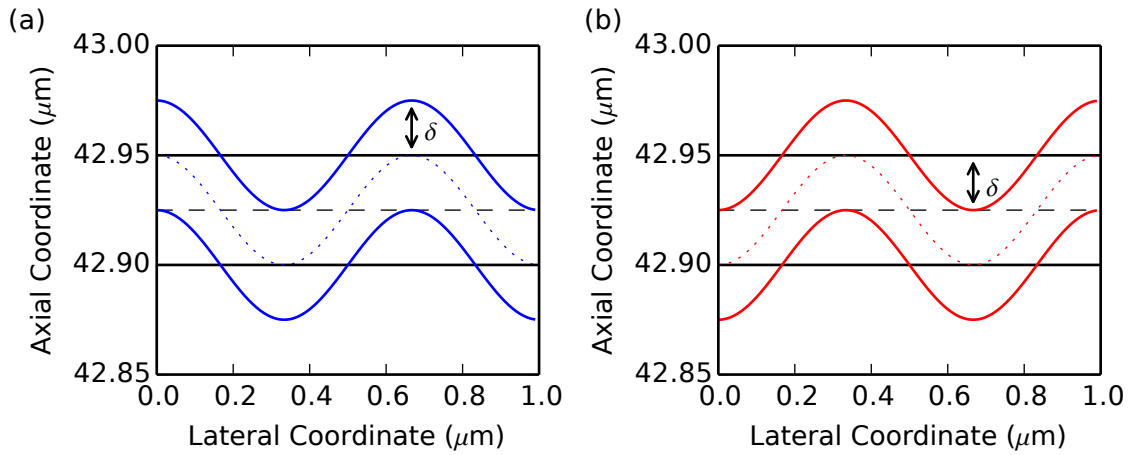

Figure 4.4: Representative waveform images for the (a) crest model and (b) trough model. The amplitude is represented by δ.

Figure 4.4 shows a representation of the crest and trough waveform geometries at the indentation location. In images Figure 4.4(a) and (b), the solid black lines represent the original flat geometry, the colored lines represent the crest and trough type SiC layers, respectively, and the dotted lines represent the centerline of the SiC layer. The ordinate represents the axial coordinate of the geometry, and the topmost free surface of Al is at 43 μm. The top surface of the first SiC layer is displaced a distance δ while the thickness of the layer is held constant at 50 nm. This profile is then propagated through the rest of the layers.

There are approximately 125,000 fully integrated linear axisymmetric elements used in the nanolaminate model with a finer mesh size near the upper-left corner of the test sample. The element size near the indenter is 5 nm and increases in size far from the indenter. The indenter consists of 7,454 elements with an element size of 10 nm near the tip. The mesh was created using CUBIT (Sandia National Laboratories, Albuquerque, NM).

The material properties used for both Al and SiC are the same as those used in the uniaxial loading described in the previous section. Both the Si substrate and the

indenter are assumed to remain elastic. The Young's modulus and Poisson's ratio of the Si substrate are 187 GPa and 0.28, respectively. The Young's modulus and Poisson's ratio of the diamond indenter are 1,141 GPa and 0.07, respectively. All the interfaces between different materials in the composite structure are assumed perfectly bonded. Although in actual materials internal damage can occur during indentation loading, the present analysis assumes an intact multilayer structure for the purpose of gaining baseline understanding of the deformation features [17].

The indentation-derived elastic modulus and hardness were directly obtained from the finite element modeling. Figure 4.5 shows a typical loading and unloading curve from an indentation simulation. The contact stiffness at the onset of unloading, S, can be calculated using Equations 4.1 and 4.2 [15]

$$S = \frac{dP}{dh} = \beta \frac{2}{\pi} E_{eff} \sqrt{A} \tag{4.1}$$

with

$$\frac{1}{E_{eff}} = \frac{1-\nu^2}{E} + \frac{1-\nu_i^2}{E_i} \tag{4.2}$$

where A is the projected contact area at onset of unloading, β is the indenter geometry-dependent dimensionless parameter, E and ν are the Young's modulus and Poisson's ratio, respectively, of the material being indented, and E_i and ν_i are the Young's modulus and Poisson's ratio, respectively, of the diamond indenter. In the simulation, the parameter β was first calibrated with a pure Al body of the same geometry as the entire multilayers/substrate assembly (Figure 4.3), and a value of 1.06 was determined. This was accomplished by making certain that the indentation-derived Young's modulus is equivalent to the input value used in the finite element analysis. When calculating the projected contact area A, the last nodal point on the top surface in contact with the indenter was identified in the deformed mesh. Thus, the effect of pileup was automatically taken into consideration. The determination of the composite modulus E requires a known Poisson's ratio, ν. A separate finite element

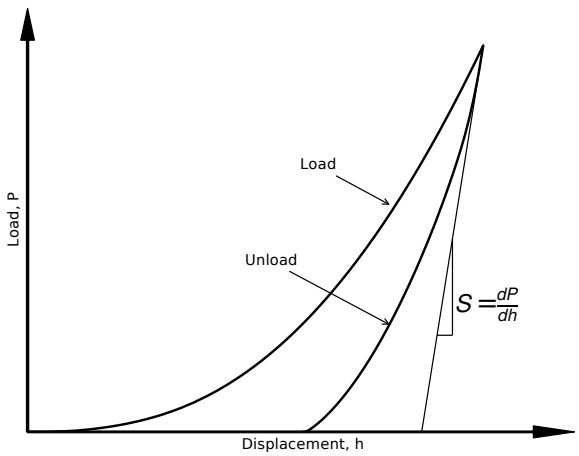

Figure 4.5: Typical load-displacement curve from a nanoindentation simulation.

analysis of uniaxial loading of the Al/SiC laminates was used to determine ν [62, 90]. Finally, the hardness of the material, H, is given by Equation 4.3

$$H = \frac{P_{max}}{A} \tag{4.3}$$

with P_{max} being the load at a given indentation depth and the corresponding projected contact area is A.

4.3 Uniaxial Response of the Undulating Multilayer Thin Film

4.3.1 Elastic Modulus and Stress/Strain Response

For multilayer composites, the mechanical response will be direction dependent, even if both materials are considered isotropic. Since the composite will be transversely isotropic, the elastic modulus in the lateral (1-axis) and vertical (2-axis) directions will be different. For the composite without layer undulation, the lateral modulus

(E_{11}) and the vertical modulus (E_{22}) can be estimated by assuming the isostrain condition (Voigt model) and the isostress condition (Reuss model), respectively [90]. The lateral and vertical moduli are given in Equations 4.4 and 4.5, respectively.

$$E_{11} = E_{Al} f_{Al} + E_{SiC} f_{SiC} \tag{4.4}$$

$$E_{22} = \left[\frac{f_{Al}}{E_{Al}} + \frac{f_{SiC}}{E_{SiC}} \right]^{-1} \tag{4.5}$$

In both equations, E_{Al} and E_{SiC}, are the Young's Modulus for Al and SiC, respectively. The volume fractions for each material are given as f_{Al} and f_{SiC}, respectively. Each equation is derived based on a one-dimensional assumption. When applying these equations to a two- or three-dimensional structure, the predicted moduli will not take into account stress in the other directions. Not accounting for the stress in the perpendicular directions can lead to errors when using the above equations [90]. Although errors may be present, these formulas can provide a good starting point for analysis of a multilayer structure.

Equations 4.4 and 4.5 result in, for lateral (E_{11}) and vertical (E_{22}) moduli for the flat 61-layer composite, 166 GPa and 96 GPa, respectively. In this sample, there is a nearly equal number of layers for both materials (31 Al and 30 SiC layers); therefore, the volume fractions for Al and SiC are 0.508 and 0.492, respectively. In the lateral direction, the composite modulus is nearly the average of the two materials and is significantly stiffer than the vertical modulus.

Due to the limitations of the one-dimensional assumption above, the finite element method provides a technique for capturing the stress in the perpendicular directions and more accurately determining the moduli. The elastic modulus of the composite is calculated by determining the initial slope of the true stress-true strain curves. The elastic moduli in the lateral and vertical directions calculated from the finite element model are shown in Figure 4.6. In this figure, the horizontal solid lines are the moduli

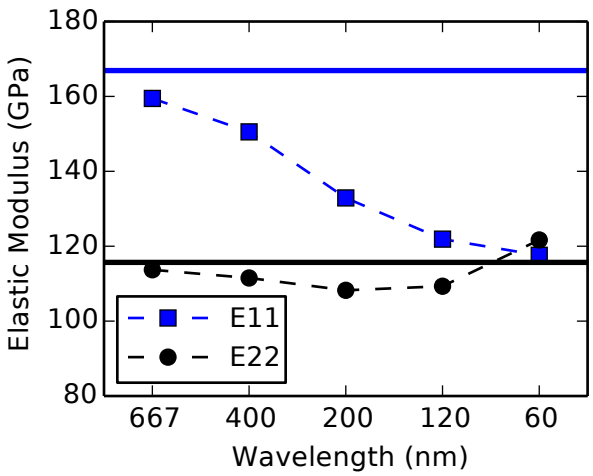

Figure 4.6: Predicted elastic modulus for 61 layer thin film composite for compressive loadings in both the vertical and lateral directions. Solid lines represent predicted elastic moduli for flat geometry (black vertical, blue horizontal).

for the case of perfectly flat geometry, obtained from the finite element analysis. The lateral modulus (E_{11}) and the vertical modulus (E_{22}) for the flat case are 167 GPa and 116 GPa, respectively. In the lateral direction, the flat-layer finite element model and the one-dimensional analytical model differ by less than 1%. The vertical moduli are quite different with the finite element model modulus approximately 27% larger.

The moduli for geometry with undulating layers are also given in Figure 4.6. The line marked by the squares represents E_{11} and the line marked by circles represents E_{22} predictions. The lateral modulus is the more sensitive of the two moduli. As the wavelength of the wavy feature decreases, the modulus decreases from 159 GPa to 118 GPa. In the lateral direction, the wavy features decrease the stiffness of the composite. To best explain how the wavy features contribute to the softening of the composite, consider the flat geometry as a homogeneous solid bar and the wavy geometry as a homogeneous material with similar wavy features (such as a spring). The solid bar (flat geometry) is very stiff in the axial direction compared to something such as a spring. The wavy features in the planar direction allow the geometry to

more easily compress in the same direction. At smaller wavelengths, the peaks and troughs get closer together, resulting in minimal lowering of stiffness with decreases in wavelength similar to a spring with a low pitch.

In the vertical (E_{22}) direction, the elastic modulus is much less sensitive to the undulating layers. There is a moderate variation in the elastic modulus as the wavelength decreases, but the overall change is less than 10%. For wavelengths greater than 200 nm, the wavy feature causes a slight decrease in the elastic modulus. The wavy features effectively soften the sample in the lateral direction and normal directions. For wavelengths less than 200 nm, the modulus increases relative to the modulus for the 200 nm wavelength. At the smallest wavelength (or largest number of cycles), the modulus actually increases to 122 GPa, greater than the modulus for the flat geometry. At this small wavelength, the wavy features effectively restrict the expansion of the sample in the lateral direction, increasing the force required to deform the sample.

The true stress-true strain response of the sample with undulating layers under compression is shown in Figure 4.7 and Figure 4.8 for vertical and lateral loading, respectively. The curves display forward loading (in compression) up to the strain of 0.18 followed by unloading and then reversed loading well into the tension regime. In both figures, the solid black line represents geometry with zero waviness, or perfectly flat layers. The remaining data represent wavy geometry from the least wavy geometry (wavelength = 667 nm) to the waviest geometry (wavelength = 60 nm). The response in Figure 4.7 shows that as the frequency of the wavy feature increases, the flow stress decreases and the apparent plastic yielding during reversed loading appears earlier. An examination of internal stress field reveals that, for each value of wavelength modeled, every Al layer remains in compression in all three orthogonal directions. In each SiC layer, both tensile and compressive stresses are present. Overall, the

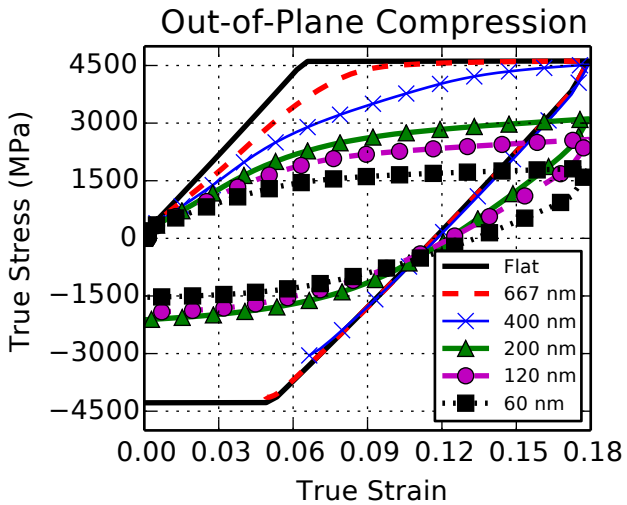

Figure 4.7: Compressive true stress-true strain response of the 61 layer thin film composite with varying waviness loaded in compression in the vertical direction. Here the positive sign represents compressive stress or strain.

addition of wavy features in vertical (22) compression causes a decrease in flow stress with little overall change in elastic modulus.

Figure 4.8 shows the stress-strain response for lateral compression of a sample with varying numbers of wavy cycles. In this loading direction, the presence of the wavy features has an immediate effect on the strength of the sample. For the two largest wavelengths (or the two lowest cycle counts), the post-yield behavior of the composite is not significantly different from that of the smaller wavelengths composites. Generally, the composites with wavy features under lateral compression behave similar to a buckled beam. Euler buckling theory suggests after buckling under a critical load, only small loads are required for relatively large displacements. When the layers are loaded in the lateral direction, buckling does occur (Figure 4.9). With the larger wavelengths, the buckling occurs much earlier than for the smaller wavelengths, which triggers the lowering of flow stress for larger-wavelength samples.

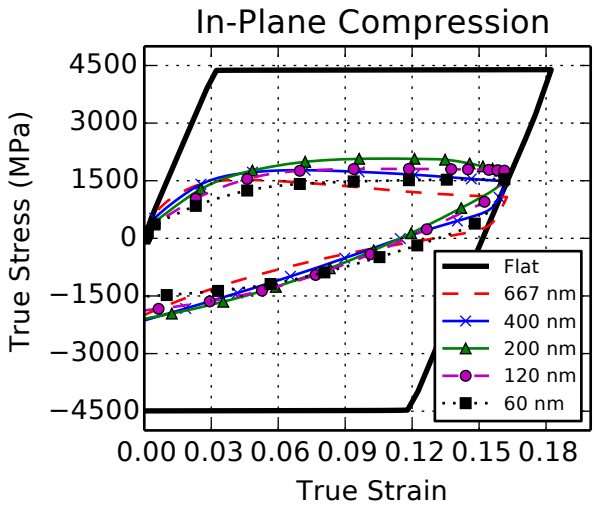

Figure 4.8: True stress-strain response of the 61 layer thin film composite with varying waviness loaded in compression in the lateral direction.

Overall, the presence of wavy features affect the post-yield behavior as well as result in a significant decrease in the lateral stiffness in the lateral direction.

Figure 4.9 shows the deformed state of the multilayer thin film with wavy layers subjected to lateral compression for wavelengths 120 nm to 667 nm and for flat layers. In the figure, each image shows the deformed state at true strain values of 0.1823 and 0.1625 for the flat and wavy cases, respectively. For each wavelength, the layer/layers that have buckled are different. For the larger wavelength, the buckling occurs in the horizontal center of the composite and emanates outward. The three other wavelengths have buckling patterns that run diagonally through the composite. The evolution of buckling leads to shear bands where subsequent deformation is localized. For a wavelength of 400 nm, the buckling begins in the top-right corner and moves towards the bottom-left corner. For a wavelength of 120 nm, the buckling region goes from the bottom-center and moves upward in a diamond pattern through approximately the center of the composite. The shape of the shear bands is dependent

on the wavelength of the undulating feature. This buckling phenomenon, leading to plastic instabilities, is what drives the decreased flow stress seen in Figure 4.8.

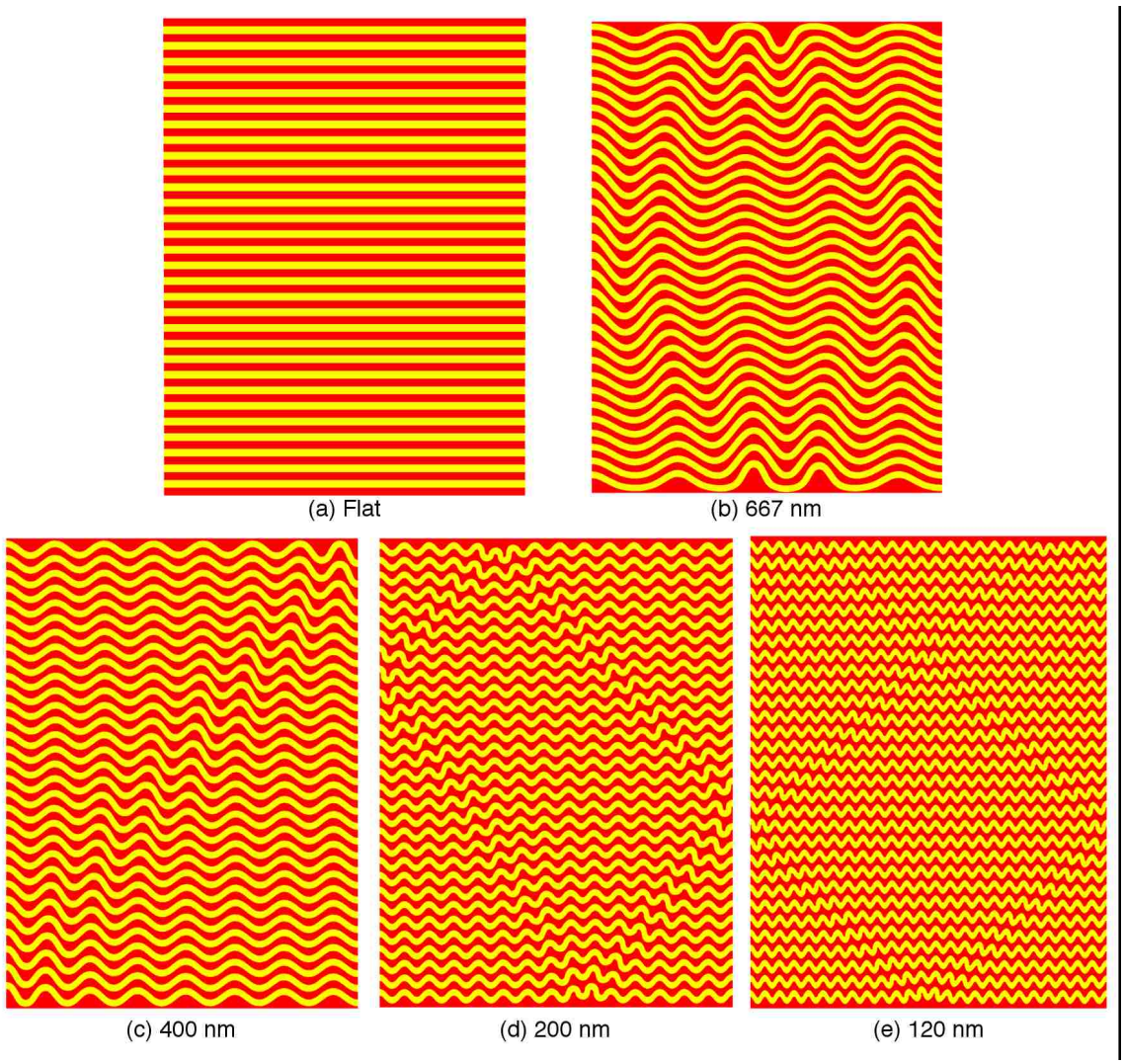

Figure 4.9: The deformed state of the thin film composite for compression in the 11-direction for various wavelengths. In the images, the top and bottom layers are Al.

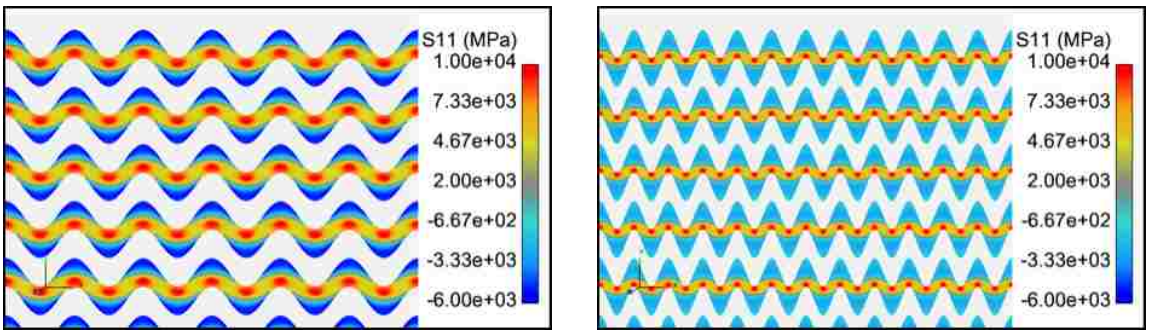

(a) Wavelength = 120 nm (b) Wavelength = 60 nm

Figure 4.10: SiC stress in the lateral direction at an overall true strain of 0.08 for two different wavelengths under vertical compression. Stress in the Al layers is not shown.

4.3.2 Evolution of Stress and Deformation Fields

Both the lateral (11) and vertical (22) compressive loadings show that the presence of undulating layers affects both the elastic modulus and the strength of the composite. Although both loading conditions have provided interesting results, the remainder of this section will focus on the vertical compressive loading, as it most closely resembles nanoindentation loading. As discussed above, for vertical compressive loading, all the Al layers are in compression in all three orthogonal directions for all variations in the geometry. The SiC in the layered composite causes the Al to remain in compression even though the lateral deformation is positive. The SiC layers are in tension laterally for the flat geometry while, with wavy geometry, the SiC layers exhibit both tension and compression. Figure 4.10 shows the lateral stress (S11) in the SiC layers for wavelengths of 120 nm and 60 nm when the overall compressive true strain is at 0.08. In the flat geometry, the lateral stress is uniform, tensile, and has a magnitude of 4.8 GPa. The wavy features result in a stress field that ranges from -6 GPa to greater than 10 GPa. Also, the largest tensile stresses in the SiC are oriented such that Mode I cracking would be possible with sufficient stress.

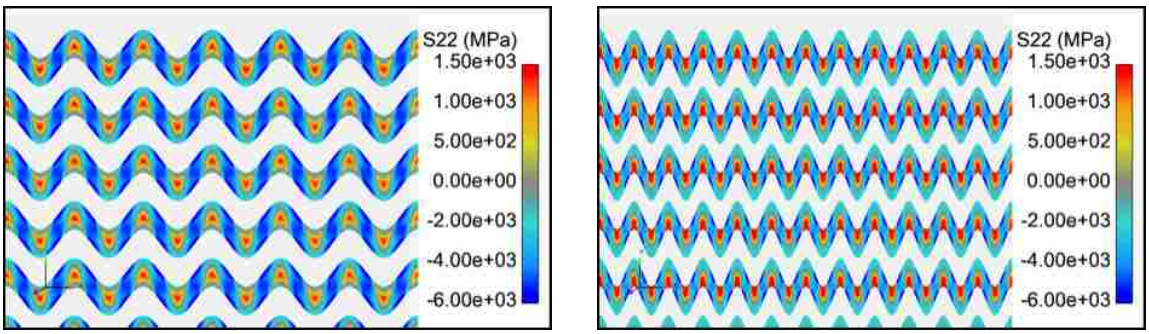

(a) Wavelength = 120 nm (b) Wavelength = 60 nm

Figure 4.11: SiC stress in the vertical direction at an overall true strain of 0.08 for two different wavelengths under vertical compression. Stress in the Al layers is not shown.

The vertical stress (S22) in the SiC is shown for two different wavelengths for vertical compression in Figure 4.11. The vertical stress in the SiC for flat geometry is uniform, compressive, and has a magnitude of 5.3 GPa. As seen in the figure, the wavy features induce a tensile axial stress greater than 1.5 GPa in the SiC. Also, the size of the tensile stress field becomes relatively larger as the wavelength gets smaller, and the tensile field shifts from the interior toward the interface region at the 'valley' positions.

Another useful metric to consider in the uniaxial loading case is the equivalent plastic strain (EQPS) developed in the Al layers. Figure 4.12 shows the EQPS in the Al layers under vertical compression for wavelengths of 120 nm and 60 nm when the overall compressive true strain is at 0.08. In the flat geometry, the EQPS in the Al layers is uniform and has a magnitude of 0.11. The presence of wavy features in the geometry causes an increase in the EQPS in the Al layers. With a wavelength of 120 nm, the peak EQPS in the Al layers is approximately 0.5. For a wavelength of 60 nm, the peak EQPS in the Al layers is well over 0.5. The location of the peak EQPS in the Al layers for all variations of wavelength is always at the Al/SiC interface.

The location implies that the Al/SiC interface is a preferred location for initiation of damage.

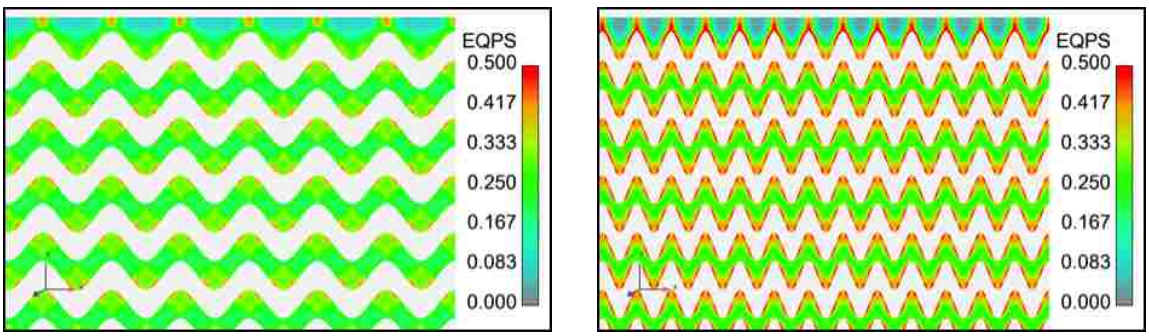

(a) Wavelength = 120 nm (b) Wavelength = 60 nm

Figure 4.12: Equivalent plastic strain in the Al layers at an overall true strain of 0.08 for two different wavelengths under vertical compression. Strain in the SiC layers is not shown.

4.4 Effect of Layer Undulation on Nanoindentation Response

The effect of undulating layer geometry on nanoindentation response is now considered. The analysis is a follow-up of the preliminary study [89] in which only one amplitude and wavelength combination was considered. In the present study, the amplitude and wavelength of the waveform is varied to determine the sensitivity of the nanoindentation response to changes in the geometry. The indentation-derived hardness and modulus, as well as internal stress and plastic strain distribution, will be compared for various values of amplitude and wavelength.

4.4.1 Indentation-derived Hardness

The main quantities of interest when performing nanoindentation are the composite hardness and elastic modulus. Therefore, these two metrics will be used to determine what effect the undulating layer geometry has on nanoindentation response. Figure 4.13 and 4.14 show the indentation-derived hardness as a function of indentation depth for the crest and trough waveforms, respectively, with varying amplitudes and wavelengths. In both cases, the presence of undulating layers results in deviation of the predicted hardness from the flat geometry. For both the crest and trough variations, undulating layers with amplitude of 12.5 nm have little effect on the predicted hardness of the multilayer structure, Figures 4.13(a) and 4.14(a). At most indentation depths, the 12.5 nm amplitude waveform changes the predicted hardness by less than 5%. The largest difference in the predicted hardness occurs at an indentation depth of 100 nm and is greater than 10%.

Figures 4.13(b) and 4.14(b) illustrate that larger amplitude undulations (25 nm) have a more pronounced effect on the predicted hardness of the multilayer thin film. For a wavelength of 400 nm and 667 nm, the sensitivity of the hardness is dependent on the geometry orientation (crest vs. trough), while the response of the 200 nm wavelength waveform is similar for both the crest and trough models. For a wavelength of 200 nm in both geometry orientations, the hardness increases as compared to the flat geometry for indentation depths less than 300 nm. For depths greater than 300 nm, the hardness is the same or less than the flat case. This suggests that when the undulation is sufficiently large, a slight softening effect exists as the frequency of the undulations increases.

For the crest orientation at an indentation depth of 100 nm, the derived hardness is very similar for all cases except the 200 nm wavelength. The 200 nm wavelength undulation results in a structure that is 1.5 times as hard (Figure 4.13(b)). This

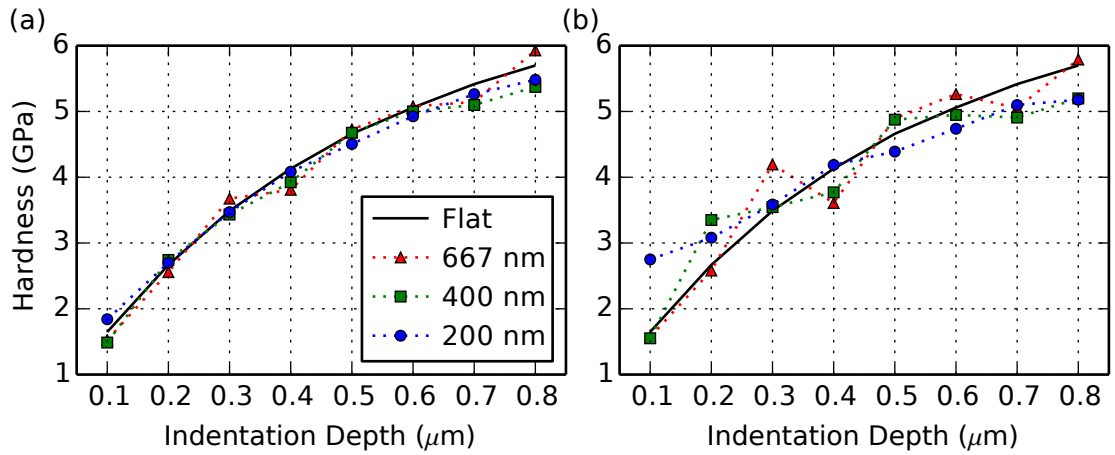

Figure 4.13: Indentation-derived hardness as a function of the indentation depth for the crest type waveform. The crest model waveform has amplitude of (a) 12.5 and (b) 25 nm, respectively, with wavelengths of 200, 400, and 667 nm.

increase in hardness is attributed to the multiple crests that are beneath the indenter during this shallow indentation depth. This is also seen in the trough orientation for all wavelengths. In the trough model and an indentation depth of 100 nm, the 200 nm and 667 nm wavelengths are approximately 30% harder while the 400 nm wavelength model is nearly 70% harder (Figure 4.14(b)). The difference in hardness is caused by the orientation of the wavy feature and the number of crests/troughs beneath the indenter for a given indentation depth.

From the results presented in Figures 4.13 and 4.14, it is evident that a stable effective hardness value of the Al/SiC layered composite does not exist. The hardness continues to increase with the indentation depth due to the combined effect of multilayer geometry and influence from the substrate material. With regard to the effect of layer undulation, no correlation between the indentation hardness response and uniaxial compression flow stress can be observed.

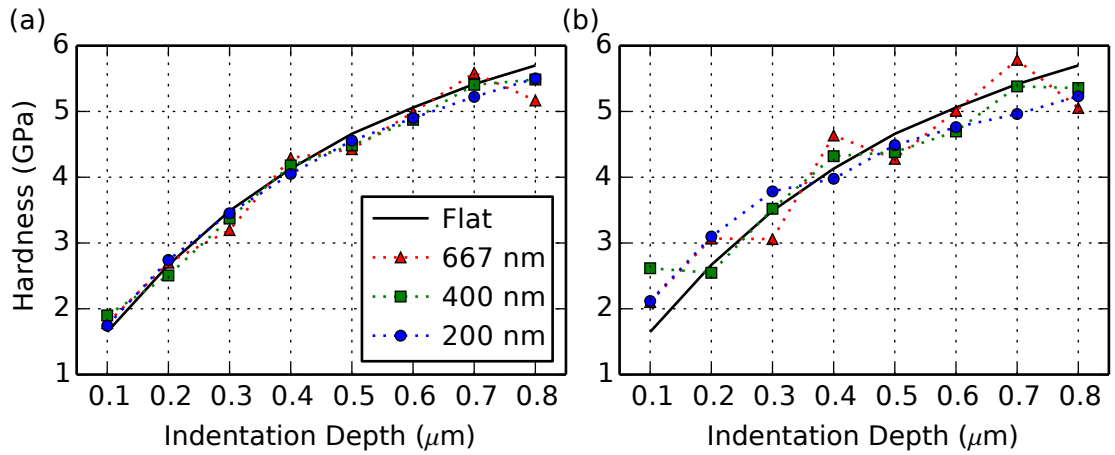

Figure 4.14: Indentation-derived hardness as a function of the indentation depth for the trough type waveform. The trough model waveform has amplitude of (a) 12.5 and (b) 25 nm, respectively, with wavelengths of 200, 400, and 667 nm.

4.4.2 Indentation-derived Elastic Modulus

Figure 4.15 and 4.16 show the indentation-derived Young's Modulus as a function of indentation depth for the crest and trough waveforms, respectively. In each figure, results for the flat geometry and wavelengths of 200, 400, and 667 nm are shown for amplitudes of 12.5 and 25 nm. For all geometry variations, while the elastic modulus is most sensitive to the largest wavelength (667 nm), the two smaller wavelengths (200 and 400 nm) undulations both result in a change to the derived modulus. With the crest type waveform (Figure 4.15), waveform amplitude of 12.5 nm has little effect on the modulus below the indentation depth of about 400 nm. For these indentation depths, the variations of the internal geometry do not cause any significant change in the contact stiffness or the projected contact area. At deeper indentation depths (above 400 nm), the internal geometry begins to have a greater influence on the contact stiffness and area. At these depths, the undulating layers with wavelengths of 667 and 400 nm effectively soften the contact stiffness. This behavior is also seen

in the uniaxial loading in the previous section; that is, the structure is less stiff in the 22-direction with undulating layers (Figure 4.6).

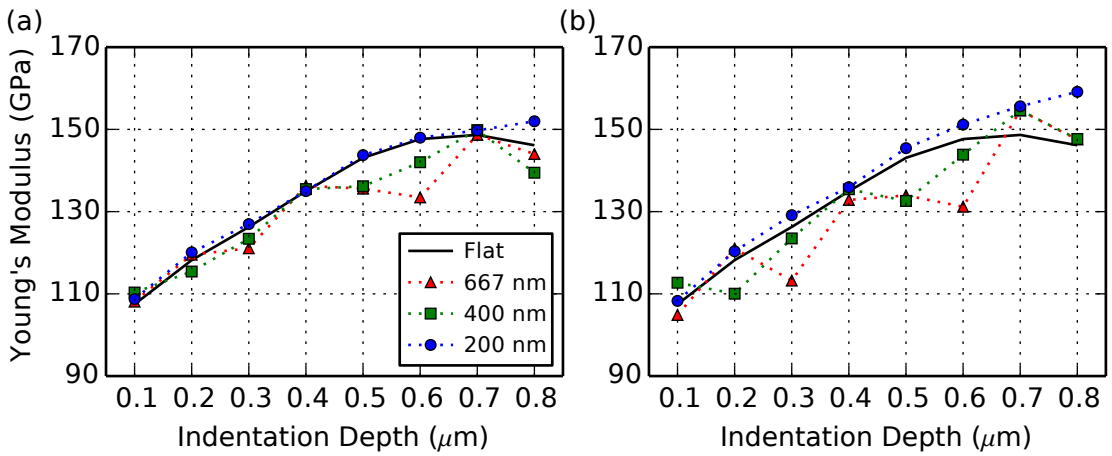

Figure 4.15: Indentation-derived Young's Modulus as a function of the indentation depth for the crest type waveform. The crest model waveform has amplitude of (a) 12.5 and (b) 25 nm, respectively, with wavelengths of 200, 400, and 667 nm.

The larger amplitude undulations shown in Figure 4.15(b) have a greater impact on the derived modulus of the composite with the crest waveform. For both amplitudes, the 667 nm wavelength has the most prominent effect on the modulus. The 400 nm wavelength undulations behave similarly to the 667 nm case but with less change to the modulus. For the smallest wavelength models (200 nm), the indentation-derived modulus has a trend similar to that of the flat geometry. For these models, the effect of the undulating layers is less pronounced for indentation depths less than 600 nm, resulting in a small increase in the modulus. The small change in the modulus is related to the frequency of the undulation and the size of the indenter. When the undulation frequency is high, the geometry imperfections are effectively minimized, resulting in no oscillatory response. At deeper indentation depths, the effects of the undulating geometry are more pronounced and stiffen the composite.

The trough waveform response shown in Figure 4.16 is similar to the crest waveform response. The 667 nm wavelength waveform results in the overall largest percent difference between the flat and undulating geometries, particularly at indentation depths greater than 100 nm, for both amplitudes considered. The small amplitude with a wavelength of 400 nm has the most impact at deep indentation depths, resulting in a 6% change in the modulus. The 200 nm wavelength models have the least influence on the derived modulus. For both the 12.5 and 25 nm amplitudes with the trough waveform, the 200 nm wavelength case results in a slight increase to the modulus at depths less 600 nm. At depths greater than 600 nm, the 200 nm wavelength undulations result in a 5% increase of the modulus. The 200 nm wavelength combined with the 12.5 nm amplitude has the least effect on the modulus for all indentation depths and geometry considered. Regardless of waveform orientation, wavelength, or amplitude, the indentation-derived elastic modulus is affected by the presence of undulating layers.

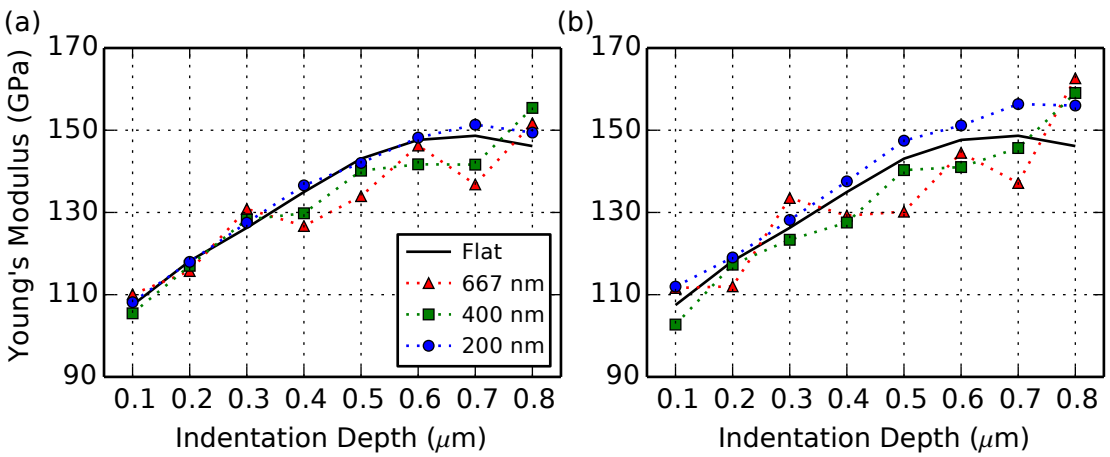

Figure 4.16: Indentation-derived Young's Modulus as a function of the indentation depth for the trough type waveform. The trough model waveform has amplitude of (a) 12.5 and (b) 25 nm, respectively, with wavelengths of 200, 400, and 667 nm.

The oscillatory behavior of the hardness and modulus is also worth noting. For low frequency undulations, the hardness and modulus response has an oscillatory

nature to it. Both the hardness and elastic modulus values oscillate about the values predicted by the flat geometry, and this oscillation is dependent on indentation depth. This behavior decreases as the frequency of the undulations increases. It is believed that this behavior is associated with the relative size of the indenter to the wavelength of the undulation. As the undulations increase, the indenter encompasses a greater number of peaks/valleys, resulting in a bulk response of the system as opposed to a response driven by internal geometry.

4.4.3 Evolution of Stress and Deformation Fields

From previous work [17] it was found that the maximum principal stress, axial stress, EQPS (in the metallic layers), and von Mises stress were useful parameters to consider when evaluating the stress/strain evolution in the layered structure. The images shown in Figures 4.17 to 4.19 are all for indentation depth of 500 nm, $\delta = 25$ nm, and $\lambda = 667$ nm. The maximum principal stress for flat, crest, and trough models in a loaded state is shown in Figure 4.17. In the nominal flat geometry, the material under the indenter is in compression and as the distance in the radial direction increases, tension is developed in the SiC layers. This same pattern exhibits itself in the undulating layers. Approximately the first ten SiC layers show elevated levels of stress (maximum principal stress $>$ 5,000 MPa) in the flat geometry, while in the undulating layers, every layer shows some areas of elevated maximum principal stress greater than 5,000 MPa. Furthermore, the tensile stress pattern developed in the SiC for the flat geometry is altered in the undulating layers.

The maximum principal stress (Figure 4.17) in the models with undulating layers exhibit a more diverse distribution of tension in the SiC layers when compared to the nominal flat layers. In the flat geometry, there is a region of high tensile stress under the indenter that propagates through multiple SiC layers. This area of tensile stress

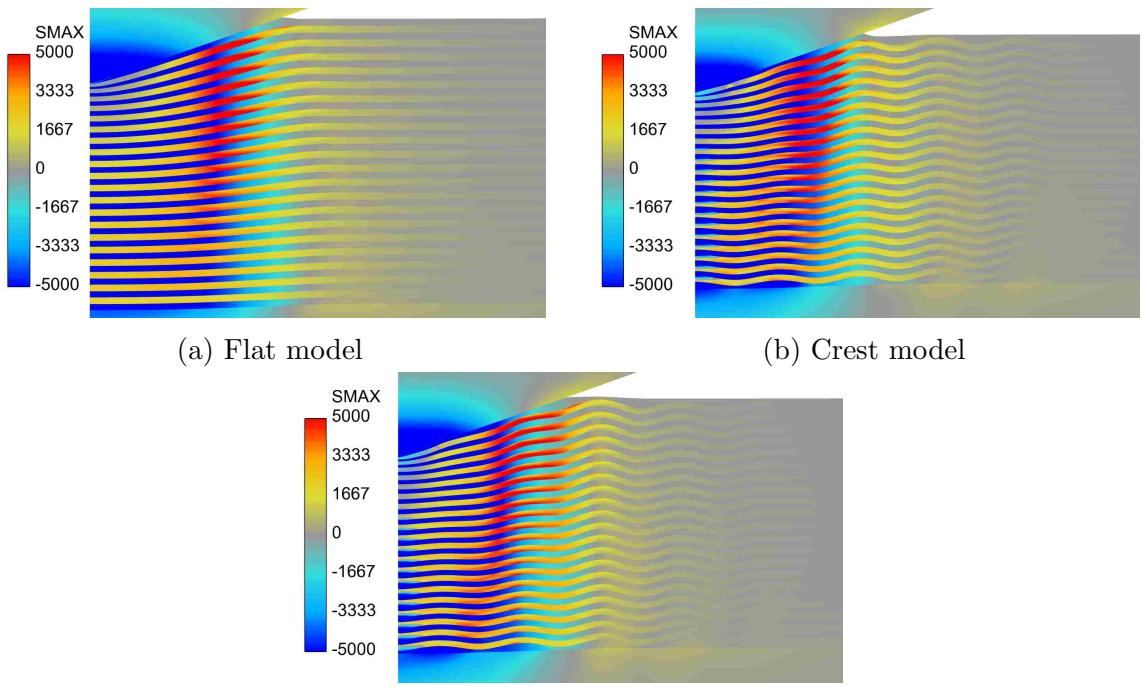

(a) Flat model

(b) Crest model

(c) Trough model

Figure 4.17: Contour images of the maximum principal stress (SMAX - MPa) near the indentation site at an indentation depth of 500 nm for various geometries: (a) the nominal flat model, (b) the crest model, and (c) the trough model. The amplitude is 25 nm and wavelength is 667 nm.

is generated by large hoop stresses (σ_{33}). The undulating layer geometries exhibit something similar but the area of high stress is larger and affects nearly every SiC layer. An increase in the hoop as well as radial stresses leads to a broader field of high tensile stress. While under compression, the wavy features are forced flat, creating large radial stresses that contribute to higher levels of maximum principal stress. Lastly, directly under the tip of the indenter, the undulating layers have significant compression unlike the flat layers, again caused by the flattening of the layers.

The axial stress (σ_{22}) for the flat, crest, and trough models in a loaded state is shown in Figure 4.18. In the flat model shown in Figure 4.18(a), all the layers directly under the indenter are in compression. Away from the symmetry axis and towards

the Si substrate interface, a large area of tension (approximately 200 MPa and higher) is developed. The undulating layers create a very different pattern of tension in the layers. In the crest model, Figure 4.18(b), three areas of tension are developed, separated by bands of axial compression. These bands shift as the waveforms that make up the undulating layers rise and fall. Similar patterns are developed in the trough model, Figure 4.18(c), particularly in the upper layers.

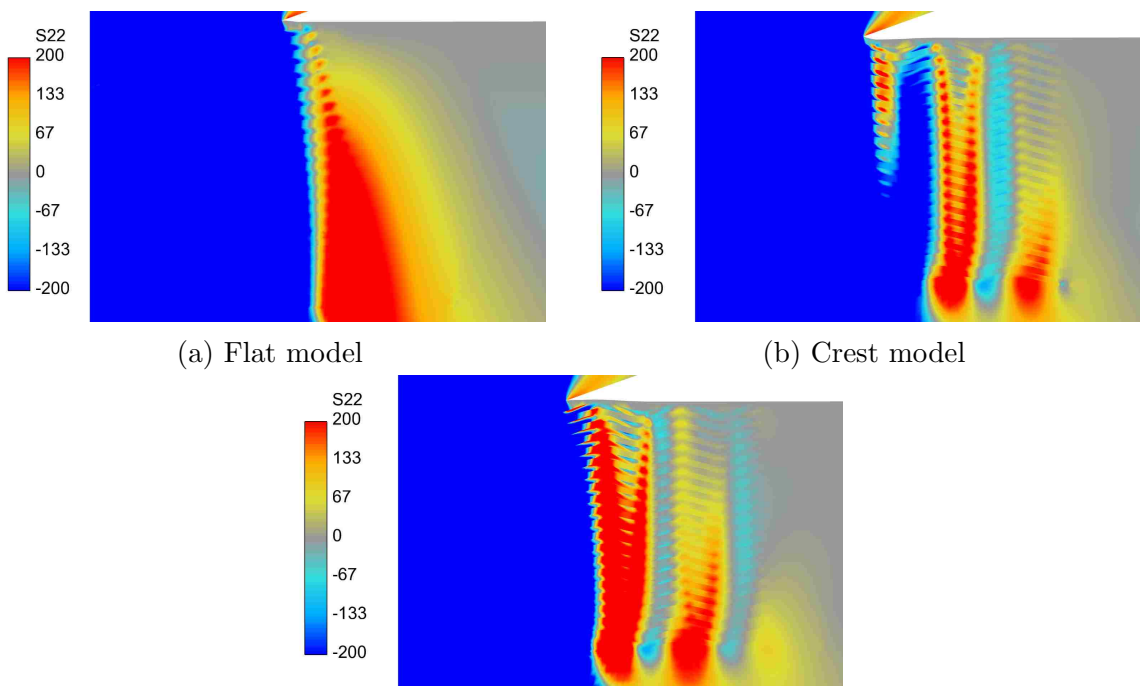

(a) Flat model

(b) Crest model

(c) Trough model

Figure 4.18: Contour images of axial stress (S22 - MPa) near the indentation site at an indentation depth of 500 nm for various geometries: (a) the nominal flat model, (b) the crest model, and (c) the trough model. The amplitude is 25 nm and wavelength is 667 nm.

The area of large axial stress in the structure with undulating layers is increased compared to that of the nominal flat structure. In the nominal structure, high levels of axial stress are focused along the Al-substrate interface. Nearly two-thirds of the layers (from the bottom-up) show high levels of axial stress as well as the substrate.

In structures with undulating layers, the wavy layers redistribute the high stress and decrease the area of large axial stress in the substrate. Specifically, the undulating layers result in bands of tensile and compressive axial stress.

The EQPS in the metallic layers for the three geometries is shown in Figure 4.19. In the flat geometry, there is a large amount of plastic strain developed in the first three layers directly below the indenter. High strain values are also present along the Al/SiC interfaces, particularly along the bottom of the Al layers. In the undulating layers, high levels of EQPS are developed through all the Al layers. This occurs in two particular locations for both the crest and trough models: First, in every layer at locations that corresponds to crests and troughs in each layer of the structure; second, at the Al-substrate interface, in which a large area of EQPS is developed in both undulating layer structures.

Equivalent plastic strain, for a structure in the loaded state, is highest along the Al/SiC interface for all variations in geometry. In the flat structure, the EQPS in each metal layer is greatest along the bottom Al/SiC interface. For structures with undulating layers, all the metallic layers show relatively high levels of plastic strain. Particularly, the bottom of the Al/SiC interface at a crest exhibits higher levels of EQPS. The SiC layers being flattened, hence creating large stresses at the interface, is responsible for this deformation pattern. Also, at locations where the bottom most layer of Al is thinnest, the Al-substrate interface exhibits high plastic strain. At these locations, the stiffer substrate is constricting the motion of the thin section of Al, generating these large plastic strains.

Figure 4.20 shows contour images of the von Mises stress near the indentation site for an indentation depth of 100 nm, in the trough model, for all wavelength cases considered with an amplitude of 25 nm. In the figure, one can see the effect the wavy features have on the stress distribution, particularly in the SiC layers of the composite. For this indentation depth, the undulating layers increase the hardness of

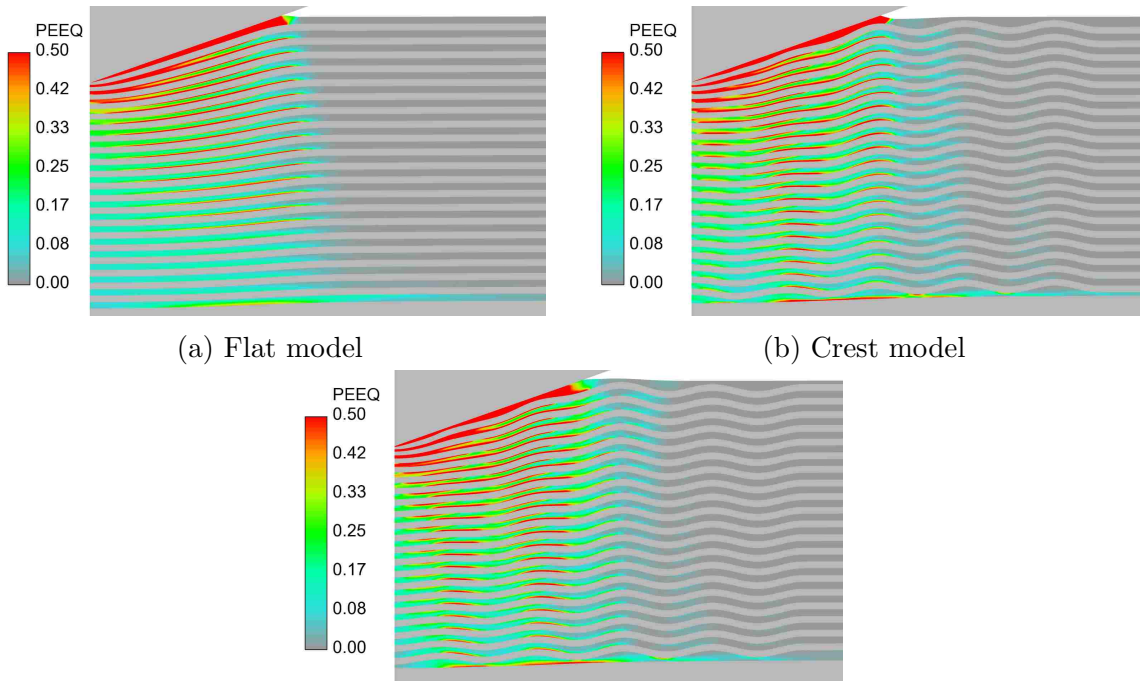

(a) Flat model

(b) Crest model

(c) Trough model

Figure 4.19: Contour images of the equivalent plastic strain in the metallic layers near the indentation site at an indentation depth of 500 nm for: (a) the nominal flat model, (b) the crest model, and (c) the trough model. The amplitude is 25 nm and wavelength is 667 nm.

the composite (Figure 4.14(b)), while the 200 and 667 nm wavelengths increase the stiffness and the 400 nm wavelength decreases the stiffness (Figure 4.16(b)). For the 667 nm wavelength undulation, the largest stress is only in the first SiC layer, unlike the first two layers of SiC as in the flat geometry. The smaller wavelength cases also have a more complex stress field as compared to the flat geometry case. With the smallest wavelength, there are large stresses in the first three layers of the SiC.

The unloading-induced plasticity is driven by multiple stress components in the Al during the unloading process. Of particular interest is the axial stress post-indentation. Figure 4.21 shows the axial stress in the layered structure after unloading. After unloading, the number of bands of tensile axial stress in the undulating layers increases

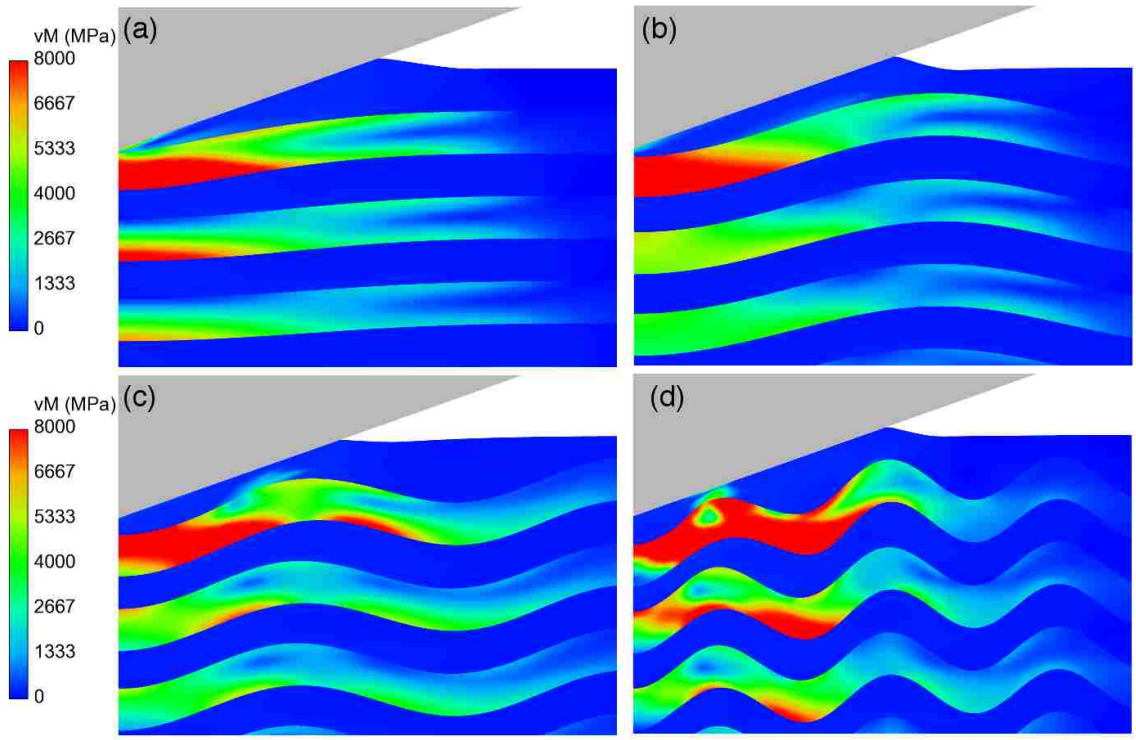

Figure 4.20: Contour images of the von Mises (vM) stress in the trough model near the indentation site in the loaded state for an indentation depth of 100 nm for various wavelengths: (a) flat layers, (b) 667 nm, (c) 400 nm, and (d) 200 nm. The contours in each image are based on the legends in (a) and (c).

and shift towards the center of the structure. Similar to the loaded state, the bands of tensile axial stress occur along the positive slope portions of the waveform. The multiple bands of tensile axial stress could likely lead to cracks between the Al/SiC layers.

In this multilayer Al/SiC film, unloading-induced plasticity occurs in the Al layers. The elastic unloading of the SiC layers, which lead to further plastic deformation of the Al layers, causes the unloading-induced plasticity. Figure 4.22 shows the EQPS in the metallic layers after the indenter has been completed unloaded for an amplitude of 25 nm and wavelength of 667 nm. The two structures with undulating layers have much larger areas of high plastic strain compared to the flat structure. As the

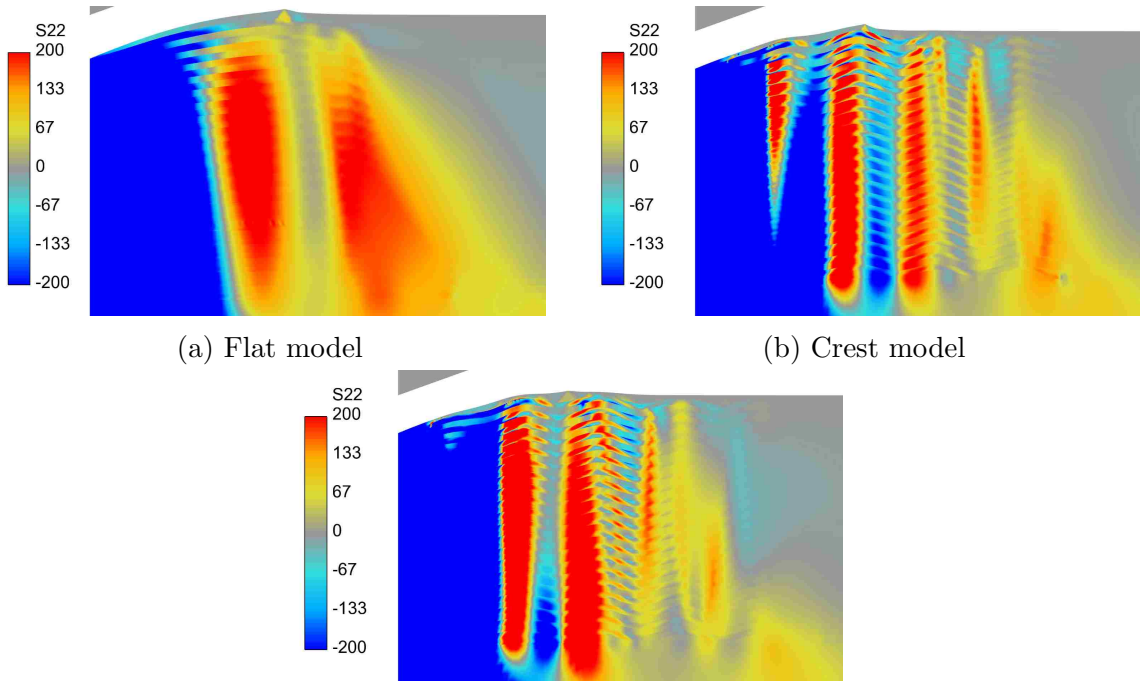

(a) Flat model

(b) Crest model

(c) Trough model

Figure 4.21: Contour images of the axial stress (S22 - MPa) near the indentation site in the unloaded state after an indentation depth of 500 nm for: (a) the nominal flat model, (b) the crest model, and (c) the trough model. The amplitude is 25 nm and wavelength is 667 nm.

wavy SiC layers unload elastically, they attempt to return to their original shape, causing the already strained Al to develop larger amounts of plastic strain. Also, the Al-substrate interface experiences an increase in the plastic strain, particularly at the thinnest portion of Al. This is consistent between both the crest and trough models. The unloading phase is therefore far from being a simple elastic recovery process. The finding implies that, compared to the ideal case of flat layers, there is even greater uncertainty in using the indentation unloading response to determine the elastic modulus of the multilayers when layer undulation exists.

Figure 4.23 shows the change in equivalent plastic strain (ΔEQPS) in the Al between the unloaded and loaded state for an indentation depth of 500 nm. Note

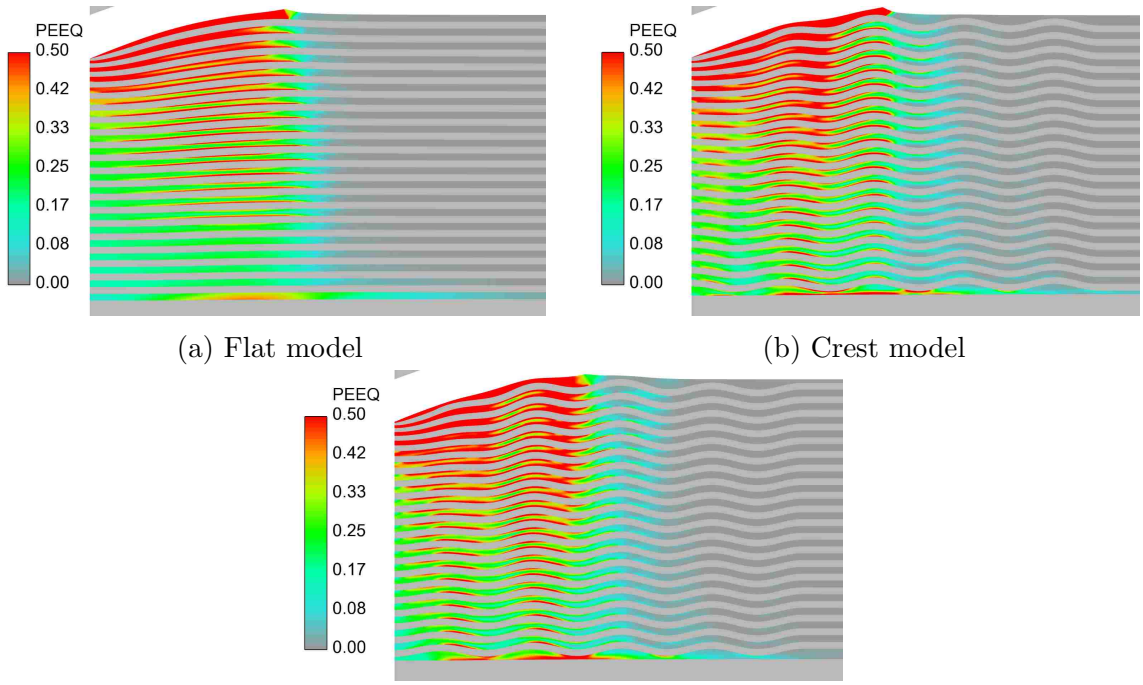

(a) Flat model

(b) Crest model

(c) Trough model

Figure 4.22: Contour images of the total equivalent plastic strain in the metallic layers near the indentation site in the unloaded state after an indentation depth of 500 nm for: (a) the nominal flat model, (b) the crest model, and (c) the trough model. The amplitude is 25 nm and wavelength is 667 nm.

that ΔEQPS represents plastic deformation occurring during the unloading phase of indentation, which is caused by the mechanical constraint imposed by SiC on the soft Al layers [17,88]. In this figure, there are four different geometry configurations of the crest model: the flat case and three progressively smaller wavelength waveforms. The SiC is colored gray and does not correspond to the legend in each image. From the contour images, it can be seen that the ΔEQPS increases as the wavelength decreases. The wavelength also influences where the maximum ΔEQPS occurs in the composite. From the flat geometry to the smallest wavelength, the location of the maximum ΔEQPS moves radially towards a location corresponding to the maximum contact radius of the indenter. In addition, the number of layers with large amounts of plastic

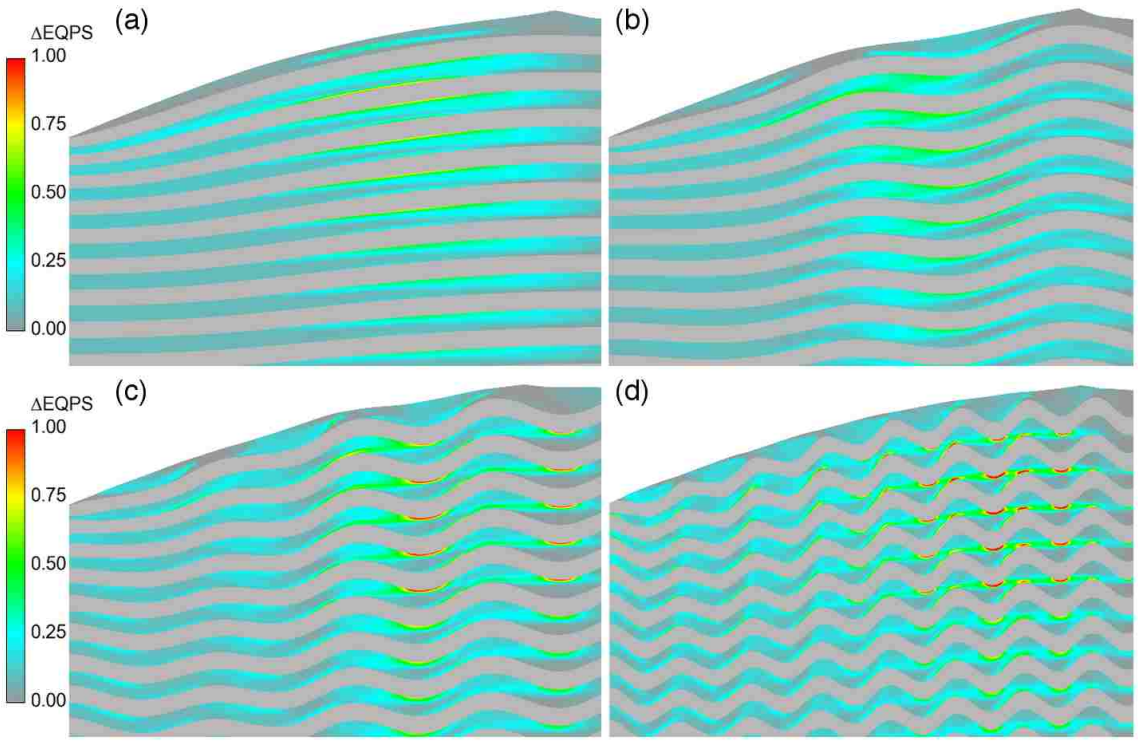

Figure 4.23: Contour images of the change in equivalent plastic strain between the unloaded and loaded state in the metallic layers near the indentation site after unloading for an indentation depth of 500 nm for the crest models with various wavelengths: (a) flat layers, (b) 667 nm, (c) 400 nm, and (d) 200 nm. The contours in each image are based on the legends in (a) and (c).

strain increases as the wavelength decreases. Also, the highest ΔEQPS occurs in the troughs of the metallic layers. The peak ΔEQPS in these models increases from 0.92 for the flat geometry to 2.08 for the 200 nm wavelength geometry. There is also a high level of ΔEQPS in the bottommost Al layer at the Al/SiC interface.

Figure 4.23 reveals that the unloading-induced plasticity in the metallic layers is enhanced by the undulated layer geometry. Because the unloading is not purely elastic, the composite modulus as measured by indentation unloading will be affected. It is not clear in what way and to what extent the indentation-derived elastic modulus is actually affected. Thus, further studies are needed. It suffices to conclude that,

due to the localized nature of indentation loading and the associated spatial variation of deformation field, the indentation-derived modulus presents no direct correlation with that obtained from overall compression loading.

4.4.4 Effect of Silicon Substrate

The relatively high stiffness of the substrate in thin film applications can impact the derived hardness and elastic modulus of the structure. For the case of a multilayer thin film laminate with wavy layers, the substrate effect is still present. The substrate effect is dependent on indentation depth and leads to higher predicted values of hardness and elastic modulus. For shallow indentation depths (less than 250 nm), the difference in hardness and elastic modulus is less than 5% and 8%, respectively, when comparing a Si substrate and an approximated substrate that represents the layered geometry. At deeper indentation depths (greater than 250 nm), the difference can be as high as 15%. Though the substrate does indeed result in higher predicted hardness and modulus, the trends seen in Figures 4.13 to 4.16 are still present. Therefore, the results obtained from the model with wavy features still provide useful insight into the overall effect of the wavy geometry.

4.4.5 Comparison with Experiment

This chapter has presented a variety of results demonstrating the effect of imperfect layer geometry on indentation-derived variables. Under ideal circumstances, it would be prudent to compare the results for the undulating geometry to experimentally obtained data from similar geometry. Currently, there is no method to fabricate a multilayer structure with fixed-pattern waviness. In order to provide a link between the model and experiment, a subset of the data from the undulating geometry model is compared to indentation data obtained from testing [17] of the specimen

shown in Figure 4.1. Note that the specimen used in the indentation experiment has no intentional, regular undulation pattern and was fabricated using established magnetron sputtering techniques.

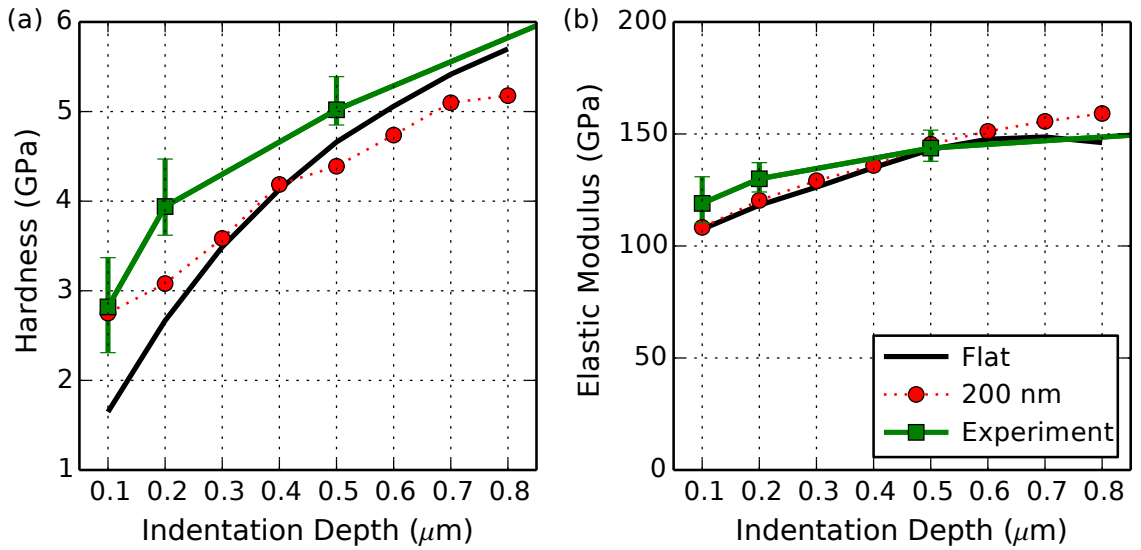

Figure 4.24: Comparison of the experimental [17] and model indentation-derived hardness and elastic modulus. The undulating model results shown here are for the crest model with amplitude of 25 nm and wavelength of 200 nm.

The indentation-derived hardness and elastic modulus for the multilayer structure from both models and experimental results are shown in Figure 4.24. In this figure, the only data for undulating geometry is the crest model with amplitude of 25 nm and wavelength of 200 nm. For both the flat and wavy models, the agreement with the experimental results is reasonable. The largest discrepancy between the nominally flat model and experimental data is seen in the indentation-derived hardness for shallow indentations. The data from the wavy model more closely matches the experimental results. This suggests that there is uncertainty associated with the assumption of a perfectly flat geometry for this specimen. It is possible that the layers were not perfectly flat near the indentation site, which could have caused an increase in the hardness. The elastic modulus for both models and experiments compare well.

Although the physical specimen had no intentional, regular undulation pattern, the wavy model data better match the experimental data compared to the flat model data for shallow indentations. The comparison indicates that differences in model and experimental data may be attributed, at least partially, to imperfect layer geometry in the physical specimen.

4.5 Conclusions

Numerical finite element modeling was performed to determine the effect of undulating SiC layers on the mechanical response and the stress/deformation fields in metal-ceramic multilayered thin film composites. Two models were considered. First, 61 undulating layers of alternating hard and soft material were subjected to overall uniaxial compressive loadings in the lateral (11) and vertical (22) directions. The lateral loading caused a decrease in the composite stiffness as the frequency of the undulations increased. In-plane loading also causes shear bands to develop, decreasing the flow stress in the composite and leading to plastic instabilities. The composite modulus was less sensitive in the vertical direction to the presence of the undulating layers, though there was a progressive loss of flow strength in the composite as the frequency of the undulation increased. From these results, it is shown that the presence of undulating layers does indeed affect the mechanical properties of the multilayer thin film composite.

The second model consists of 41 alternating layers of 50 nm thick Al and SiC on a Si substrate subjected to axial (22) nanoindentation loading. For undulation amplitude of 12.5 nm the effect on the indentation-derived quantities were minimal, particularly at shallow indentation depths. For an amplitude of 25 nm, the crest and trough models lead to indentation-derived hardness and modulus values that differ from the nominal flat geometry by as much as 10%. The variation in hardness and modulus is

dependent on indentation depth and the phase of the waveform. The indentation-derived Young's Modulus becomes less sensitive to wavelength as wavelength decreases (i.e. more undulations in the geometry), at shallow indentation depths. The modulus is most sensitive to the undulation frequency and amplitude for deep indentations. Also, the stress fields in both materials become more complex as the number of undulations increases. The indentation-derived modulus and hardness generally display no direct correspondence with those obtained from uniaxial compression loading. Overall, greater uncertainty exists when using the indentation unloading response to determine the elastic modulus of multilayered thin film composites.

Chapter 5

Indentation-Derived Elastic Modulus of Multilayer Thin Films: Effect of Unloading-Induced Plasticity

The contents of Chapter 5 are based on a previously published manuscript. Therefore, in an effort to preserve self-sufficiency, certain remarks and discussion also appear elsewhere in the dissertation manuscript.

5.1 Introduction

Natural and engineered multilayer structures can exhibit intriguing properties and functionalities [91]. As an example, lamellar structures (α ferrite/Fe_3C cementite) on the microscopic scale are the foundation for the combination of strength and toughness of steels. Some structures in nature, such as mollusk shells, derive their high strength

and toughness from ceramic layers bonded together by an organic glue [92]. Multilayer thin films may now actually be viewed as a new class of materials. With a thickness of up to tens of microns and layer thicknesses of a few to hundreds of nanometers, these structures have a wide range of applications including optical devices, high-performance capacitors, ultrahigh-strength materials, thermo-electric materials, high wear resistance and low friction coatings for gears, bearings, cutting tools, and thermal protective layers in aircraft and automobile engines [93–98]. In addition, certain systems, such as the Al/SiC nanolayers, are being considered as reflective coatings in ultraviolet applications [60, 99, 100]. Compared to traditional materials systems, these materials can offer higher strength-to-weight ratios, less friction and wear, higher operation temperatures, corrosion resistance, and fracture toughness. Therefore, designing and manufacturing multilayered structures at the micro- and nano-scales is an attractive strategy for developing a new generation of protective and infrastructure materials, and thus have been subjects of intensive research [7–9, 11, 87, 101, 102].

The scale and complexity of these multilayered structures often makes it difficult to characterize mechanical behavior. Nanoindentation is a commonly used experimental technique to determine the composite hardness and elastic modulus. The hardness can be derived directly from the peak indentation load and projected contact area. On the other hand, the indentation-derived elastic modulus is determined from the projected contact area and the contact stiffness at the onset of unloading. Various experimental and analytical methods exist to determine accurately the projected contact area of indentation. The method proposed by Oliver and Pharr [15] is traditionally the accepted procedure for calculation of the contact stiffness. One of the fundamental assumptions regarding the contact stiffness behavior is that the unloading remains elastic particularly during the initial unloading [22, 24, 103].

Because of the dependency of the derived elastic modulus on the contact stiffness at the onset of unloading, nanoindentation unloading has received significant

attention [16, 28, 31]. It has been determined that for indentation of homogeneous materials, as well as single-material thin films on substrates, plastic deformation has a negligible influence on the unloading response. Thorough experimental and analytical studies have shown that methods such as that developed by Oliver and Pharr are only valid if the material remains largely elastic during the unloading process [32]. Although the validity of elastic unloading of homogeneous materials has been determined, recent analytical observations suggest that significant plastic deformation can occur in a multilayered structure during unloading [17, 19, 65]. It was observed that under quasi-static, viscoplastic, and cyclic indentations, the plastic deformation in the metallic layers of a multilayered structure increases during the unloading phase of the indentation. The discovery of unloading-induced plastic deformation results in an inherent degree of uncertainty in the indentation-derived elastic modulus of multilayered structures.

The objective of this chapter is to address the variation in the indentation-derived elastic modulus due to the presence of unloading-induced plasticity. Using prior nanolayered material as a model system, the effect of unloading-induced plasticity on the indentation-derived modulus is studied numerically. To provide a baseline, the indentation-derived hardness and modulus of the model system is calculated using the finite element method. The unloading-induced plastic strain at various stages of the unloading process is presented and compared. A theoretical framework is applied to elucidate the difference between the true and apparent moduli derived from indentation. Lastly, cyclic indentation is explored as an effective technique to obtain the indentation-derived modulus. Implications of the numerical findings in relationship to experimental techniques are also discussed.

5.2 Model Description

The model system considered in this study consists of alternating layers of Al and SiC created by physical vapor deposition (PVD) sputtering on a Si substrate. The system contains 41 layers, and each layer is approximately 50 nm thick. The microstructure of the individual layers was characterized using a dual beam focused ion beam (FIB) technique and scanning electron microscopy (SEM). A SEM-generated cross-sectional view of the material system is shown in Figure 5.1.

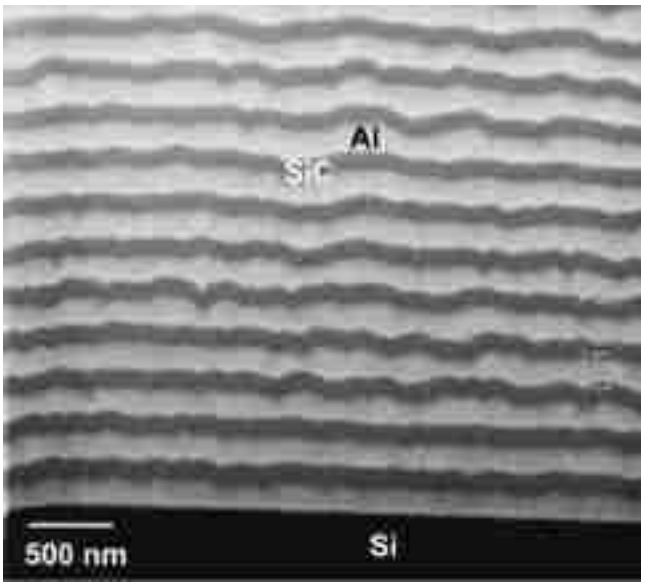

Figure 5.1: Scanning electron micrograph of the cross-section of Al/SiC multilayer thin films on a Si substrate [10].

The finite element model used in the indentation analysis consists of 41 alternating Al and SiC thin films on a substrate of Si. This corresponds to the actual nanolayered system studied previously [17]. A schematic of the baseline model is shown in Figure 5.2. Both the top layer (in contact with the indenter) and the bottom layer (adjacent to the Si substrate) are Al. A conical diamond indenter with a semi-angle of 70.3° is assumed. This indenter geometry results in the same projected contact area for a given depth as that of a Berkovich indenter in common nanoindentation

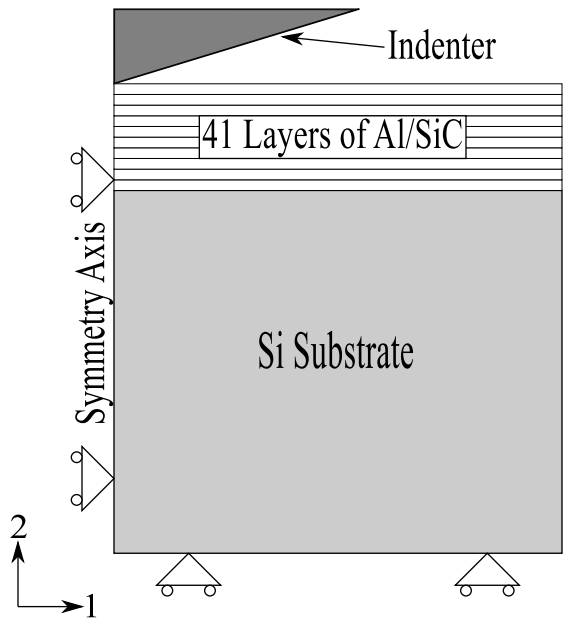

Figure 5.2: Schematic showing the Al/SiC laminates above a Si substrate and the boundary conditions used in the axisymmetric model. The left boundary is the symmetry axis. The entire specimen is 40 μm in lateral span (radius) and 43 μm in height. Each individual Al and SiC layer is 50 nm thick.

experiments. Use of the conical indenter is a practical way to model the indentation process in a two-dimensional setting [82]. The model is axisymmetric with the left boundary being the symmetry axis. The entire specimen is 40 μm in lateral span (radius) and 43 μm in height. The thicknesses of the individual Al and SiC layers are 50 nm each. During deformation the left and bottom boundaries are allowed to displace only in the axial and radial directions, respectively. The right boundary is not constrained. The top Al surface, when not in contact with the indenter, is also free to move. When contact with the indenter is established, the surface portion engaged by the indenter directly interacts with the indenter. The coefficient of friction between the indenter and the top surface is 0.1, which is a typical value for the diamond/metal contact surface [83, 84].

Approximately 125,000 fully integrated linear axisymmetric elements are used in the finite element model with a finer mesh size near the upper-left corner of the test material. The element size near the indenter is 5 nm and increases in size far from the indenter. The indenter consists of approximately 8,000 elements with an element size of 10 nm near the tip. The mesh was created using CUBIT (Sandia National Laboratories; Albuquerque, NM). The finite element program ABAQUS (Version 6.13, Dassault Systemes Simulia Corp.; Providence, RI) was used to carry out the analysis.

The Young's moduli for Al and SiC are assumed to be 59 GPa and 277 GPa, respectively [61]. Nanoindentation of single-layer Al and SiC films provided the moduli for these materials. The Al and SiC modulus is lower than the bulk modulus as the thin film properties of both materials are lower than the bulk properties. The somewhat lower modulus of SiC, relative to crystalline SiC (which is around 410 GPa), is due to the fact that the physical vapor deposited SiC layers in the present case were amorphous [61]. The Poisson's ratios for Al and SiC were taken as 0.33 and 0.17, respectively. The plastic response of Al was based on the tensile loading data of single-layer Al with a yield strength of 200 MPa. Rate-independent isotropic elastic-plastic response was assumed with plastic yielding following the von Mises criterion with isotropic hardening and the incremental flow theory. The piecewise linear strain hardening response features hardening slopes of 199.33 MPa from initial yielding up to the strain of 50.51% and then 39.97 MPa up to the strain of 300.68%, beyond which perfect plasticity ensues. SiC is a much more brittle material. Nevertheless, a very high yield point of 8,770 MPa (estimated from the indentation hardness of a single-layer SiC film [9]) was used followed by perfect plasticity. This assumption is necessitated by the fact that a purely elastic SiC in the model will generate unrealistically high loads during the indentation simulation, and it is validated by the fact that in the experiment the SiC layers exhibited a glassy/plastic-type response due to the amorphous nature of the film [12]. Both the

Si substrate and the indenter are assumed to remain elastic. The Young's modulus and Poisson's ratio of the Si substrate are 187 GPa and 0.28, respectively. The Young's modulus and Poisson's ratio of the diamond indenter are 1,141 GPa and 0.07, respectively. All the interfaces between different materials in the composite structure are modeled as perfectly bonded. Although internal damage can occur during indentation loading [10], the present analysis assumes an intact multilayer structure for the purpose of gaining a baseline understanding of the deformation features.

The indentation-derived elastic modulus and hardness were directly obtained from the finite element modeling. Figure 5.3 shows the modeled load-displacement curve at indentation depths of both 500 and 1000 nm. The contact stiffness at the onset of unloading, S, is defined as [15]:

$$S = \frac{dP}{dh} = \beta \frac{2}{\pi} E_{eff} \sqrt{A} \tag{5.1}$$

with

$$\frac{1}{E_{eff}} = \frac{1-\nu^2}{E} + \frac{1-\nu_i^2}{E_i} \tag{5.2}$$

where A is the projected contact area at onset of unloading; β is the indenter geometry-dependent dimensionless parameter; E and ν are the Young's modulus and Poisson's ratio, respectively, of the material being indented; and E_i and ν_i are the Young's modulus and Poisson's ratio, respectively, of the diamond indenter. In the simulation the parameter β first was calibrated with a pure Al body of the same geometry as the entire multilayers/substrate assembly (Figure 5.2), and a value of 1.06 was determined. This was accomplished by making certain the indentation-derived Young's modulus is equivalent to the input value used in the finite element analysis. When calculating the projected contact area A, the last nodal point on the top surface in contact with the indenter was identified in the deformed mesh. Thus, the effect of pileup was automatically taken into consideration. The determination of the composite modulus

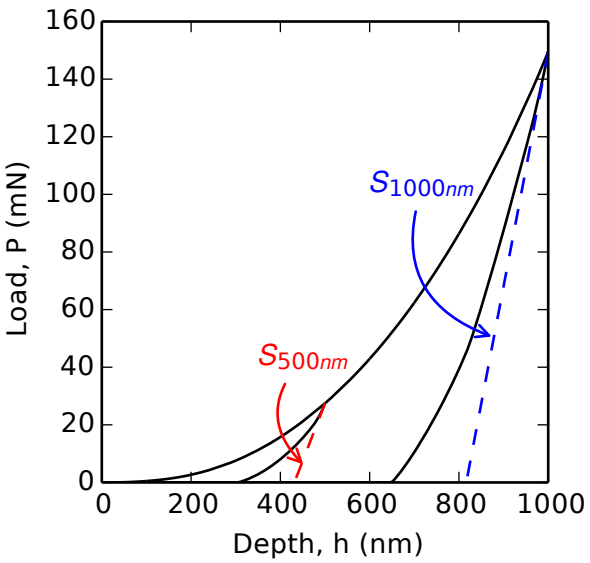

Figure 5.3: Load-displacement curves for indentation depths of 500 and 1000 nm. The contact stiffness S at the onset of unloading is also shown for both indentation depths.

E requires a known Poisson's ratio ν. Here a separate finite element analysis of uniaxial loading of the Al/SiC laminates was used to determine ν [62, 90], which results in a value of 0.25. Finally, the hardness of the material H was calculated from

$$H = \frac{P_{max}}{A} \tag{5.3}$$

with P_{max} being the load at a given indentation depth and A being the corresponding projected contact area.

The contact stiffness at the onset of unloading, S, for a Berkovich indenter is traditionally calculated experimentally using the relationship formulated by Oliver and Pharr [15]. The unloading load-displacement data is described by

$$P = C\,(h - h_f)^m \tag{5.4}$$

where P is the load, $(h - h_f)$ is the elastic displacement, and C and m are material constants. The contact stiffness is then found by analytically differentiating Equa-

tion 5.4 and evaluating the derivative at the peak load and displacement. To calculate the contact stiffness at the onset of unloading from the present finite element model, a least-squares linear regression is fitted to a portion of the unloading load-displacement data. In the current study, the initial 2% of the unloading curve (based on the peak load) is used to fit the linear regression unless stated otherwise. An example of the fit is shown in Figure 5.3 for indentation depths of 500 and 1000 nm and is denoted by S. While it is possible to use the Oliver and Pharr method to calculate the contact stiffness, fitting a linear regression to the initial portion of the model unloading is efficient and provides an accurate measurement of the contact stiffness at the onset of unloading. Furthermore, the unloading data calculated from the finite element model is smooth as opposed to experimental data which can be quite noisy; therefore, it is practical to use a linear regression to calculate the contact stiffness.

For the metal-ceramic multilayer systems in question, not only will plasticity develop during the indentation, but plasticity can continue to develop during the unloading as mentioned in the introduction. To determine if unloading-induced plasticity affects the indentation-derived modulus, modifications are made to the material models discussed above. During the loading step, the materials are as described above, but during unloading the materials are artificially enforced to remain elastic for this additional consideration. This is accomplished by setting the yield strength of all materials during unloading to be very large. Thus, results can be compared with the regular models where plastic deformation in the metallic layers does occur during unloading.

5.3 Results and Discussion

5.3.1 Evolution of Plastic Strain Field

The development of plastic strain during the indentation process is a known phenomenon. Plasticity commonly occurs in homogeneous materials directly beneath the indenter as well as at the film-substrate interface for thin metallic films. For the multilayer system considered, a more complex deformation pattern exists. Figure 5.4 shows the equivalent plastic strain (EQPS) in the model system for an indentation depth of 1000 nm. At the maximum indentation depth, the plastic strain directly beneath the indenter is highest. There are also large amounts of plastic strain at the Al/SiC interface in each Al layer and at the interface between the bottom Al layer and Si substrate. In the unloaded state, the plastic strain distribution changes. The volume of material with large plastic strain (EQPS>1) increases. Also, there is a large increase in the plastic strain at the Al/Si interface. This shows that the unloading process does indeed result in an increase in plastic strain. To better understand the change in plastic strain from loaded to unloaded state, the net change of equivalent plastic strain, ΔEQPS, will be considered subsequently.

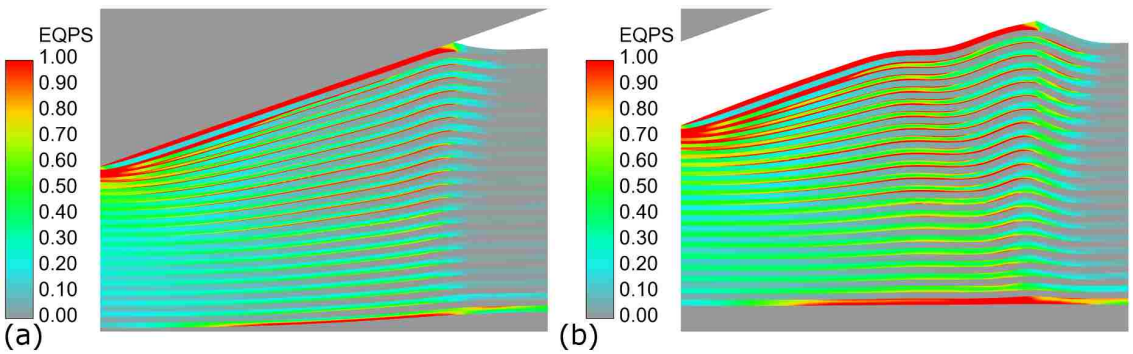

Figure 5.4: Equivalent plastic strain contours for an indentation depth of 1000 nm in the (a) loaded and (b) unloaded states.

Though plastic strain is common during the indentation, it is the presence of unloading-induced plasticity that will affect the indentation-derived modulus. During indentation, the metallic layers flow away from the center of indentation. This, in conjunction with the metallic layers on both sides of the ceramic, allows the ceramic to bend significantly [18]. This interaction results in a very complex unloading scenario. Unlike homogeneous systems in which material is able to relax during unloading, the metallic layers in the multilayer system are constrained by the ceramic layers during unloading. This extra constraint imposed by the hard ceramic layers not only alters the elastic unloading behavior of the metallic layers but also results in significant plastic strains at the metal/ceramic and bottom-metal/substrate interfaces–particularly for relatively deep indentation depths.

The increase in EQPS due to unloading, ΔEQPS, is shown in Figure 5.5 for indentation depths ranging from 200 to 1000 nm. For indentation depths of 200 and 500 nm, the peak increase in EQPS is 0.5 and 0.9, respectively. The location of the peak in both cases is in the second metallic layer at its interface with the ceramic. The distribution of the increase in plastic strain is focused mostly beneath the indentation location except for the bottommost metallic layer. For indentation depths of 800 and 1000 nm, the increase in plastic strain is much more distinct. At 800 and 1000 nm, the plastic strain in the metallic layer increases by 1.4 and 2.2, respectively, and is located in the bottommost metallic layer. The plastic strain near the top of the system and directly beneath the indentation is consistent for indentations at and above 500 nm. Note that buckling of the top layers occurs during unloading for deep indentations, and strong unloading-induced plasticity in the upper layers appears to be associated with the buckling deformation. In the bottommost metallic layer, the largest increase in plastic strain occurs at the Al/SiC interface–not the Al/Si interface. The deeper indentation results in an increase in plastic strain away from the indentation site with an increase radially outward from the indentation. Particularly at 1000 nm, the increase in plastic strain is most complex with the maximum ΔEQPS values greater

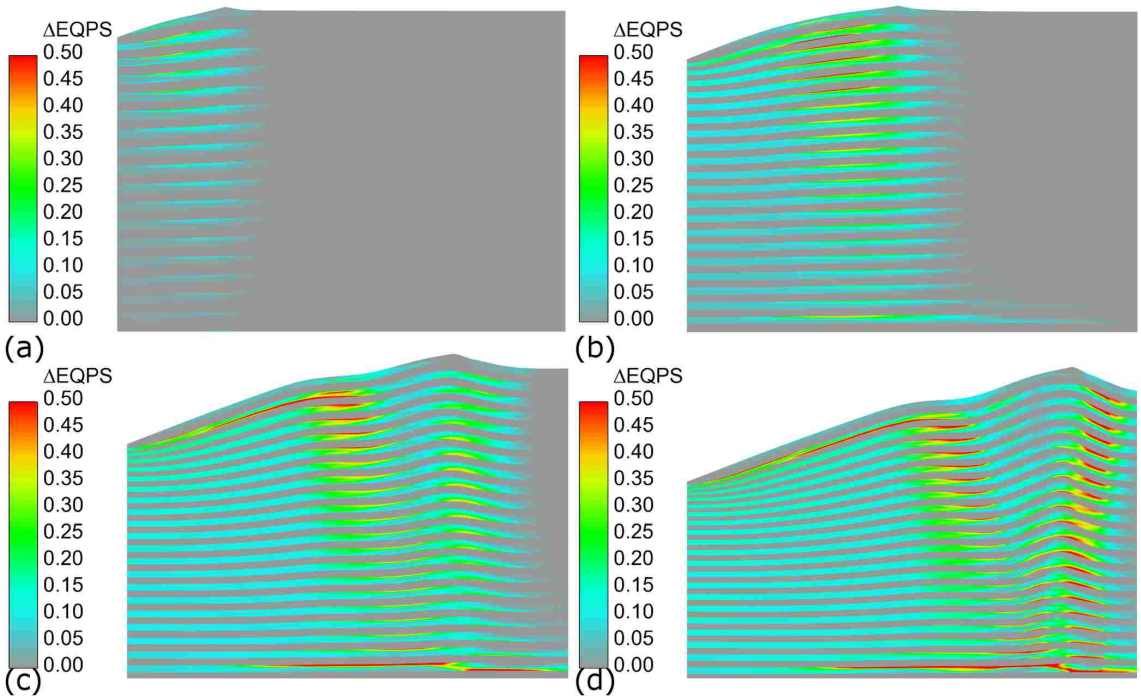

Figure 5.5: Contour images of the difference in equivalent plastic strain (ΔEQPS) between the unloaded and loaded state in the metallic layers near the indentation site after unloading for indentation depths of (a) 200 nm, (b) 500 nm, (c) 800 nm, and (d) 1000 nm.

than 0.5 in each metallic layer. At this penetration depth, the bottommost metallic layer has formed a clear shear band between the SiC and Si. Although there is a significant increase in plastic strain during the entire unloading phase, the amount that occurs during the onset of unloading needs to be investigated.

The increase in plastic strain during unloading at various stages of unloading is shown in Figure 5.6 for an indentation depth of 1000 nm. As discussed previously, the contact stiffness at the onset of unloading is calculated from the finite element model by linear regression of 2% of the unloading curve. Image (a) shows the increase in plastic strain after the indenter is unloaded 2% from the peak load. At the 2% unloaded state, the maximum increase in plastic strain is approximately 0.05 and is focused

radially outward from beneath the indenter. At (b) 5% and (c) 10% unloaded states, the maximum increase in plastic strain is 0.12 and 0.23, respectively. For each case, the increase in plastic strain does not occur directly below the indenter. The largest increase occurs in the second and third metal layers. The increase of plastic strain at the onset of unloading confirms that the assumption of initial elastic unloading is not valid for the multilayer system in question. Therefore, the dependence of the indentation-derived elastic modulus to the presence of unloading-induced plasticity warrants further investigation.

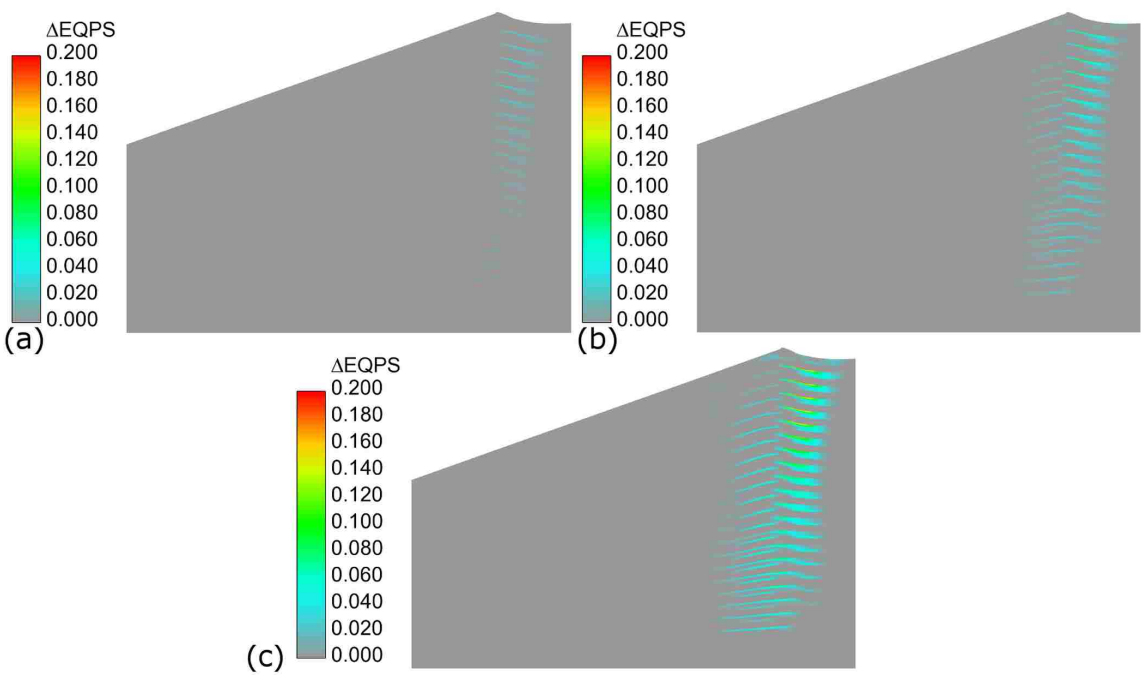

Figure 5.6: Contour images of the difference in equivalent plastic strain (ΔEQPS) between the loaded and (a) 2%, (b) 5%, and (c) 10% unloaded states for an indentation depth of 1000 nm.

5.3.2 Indentation-Derived Elastic Modulus

The previous section established that the plastic strain in the metallic layers of the model system increases at the onset of unloading. In this section, the effect of unloading-induced plasticity on the indentation-derived elastic modulus is presented. To explicate this effect, the indentation-derived modulus is calculated using standard unloading data and artificially enforced elastic unloading data; the resulting data sets are compared. Standard unloading data refer to data obtained from a model that is allowed to develop plasticity during unloading. The artificially enforced elastic unloading data refer to data obtained from a model that is not allowed to develop plasticity during unloading. To establish a basis for the comparison, three cases are presented. First, the indentation-derived elastic modulus of a homogeneous Al film on a Si substrate is considered. Second, the multilayer model system is analyzed. Third, alternating layers of Al and SiC on a different substrate material (bearing the effective property of Al/SiC multilayers, as explained below) is examined. The indentation-derived hardness is not considered because the hardness is not dependent on the contact stiffness at the onset of unloading.

A homogeneous film on a thick substrate is not expected to exhibit any unloading-induced plasticity; therefore, an Al film on a Si substrate is useful for making an initial comparison between standard unloading and forced elastic unloading. Figure 5.7 shows the indentation-derived elastic modulus of an Al film on Si substrate. In the figure, the modulus from standard unloading data using the initial 2% of the unloading curve is compared to the modulus from enforced elastic unloading data using both 2% and 5% of the initial unloading curve. The indentation-derived modulus of the Al film exhibits substantial substrate effects as the modulus monotonically increases as the indentation depth increases. The standard unloading and the forced elastic unloading match exactly. Independent of how much unloading data are used in the

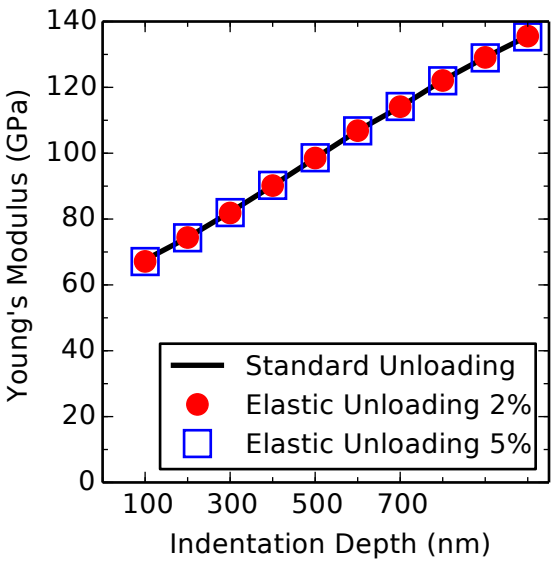

Figure 5.7: Indentation-derived Young's modulus of homogeneous Al film on Si substrate for standard unloading and forced elastic unloading calculated using the top 2% and 5% portions of the unloading curve.

modulus calculation, the forced elastic unloading matches the standard unloading. This confirms that there is no unloading-induced plasticity in the Al film.

The second of three cases considered is the multilayer model system consisting of alternating layers of Al/SiC on a Si substrate. The data in Figure 5.8 show the comparison of standard and forced elastic unloading both for 2% and 5% unloading. For indentation depths less than 500 nm, the difference between the standard and elastic unloading is negligible. There is a small difference between the 2% and 5% unloading above 500 nm. The difference in the standard unloading curves is likely due to the difference in the amount of plasticity that has developed during unloading. Regardless of the amount of unloading considered in the contact stiffness calculation, the modulus-depth response is consistent in shape and only differs in magnitude.

Unlike the standard unloading moduli, the moduli for the forced elastic unloading do not appear dependent on the portion of the unloading curve used in the calculation.

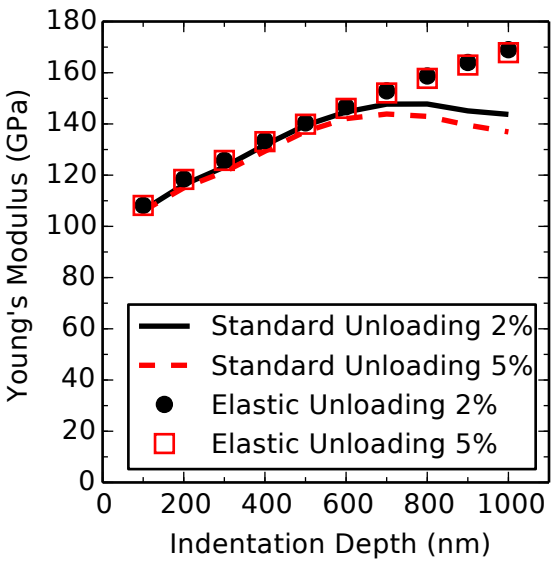

Figure 5.8: Indentation-derived Young's modulus of Al/SiC multilayer system on Si substrate for standard and forced elastic unloading calculated using the top 2% and 5% portions of the unloading curve.

At indentation depths greater than 500 nm, the standard and forced elastic unloading moduli differ substantially. At these depths, the standard unloading response begins to plateau while the forced elastic unloading continues to increase. For an indentation depth of 1000 nm, the two moduli differ by nearly 30 GPa. It was established in Figure 5.6 that the amount of unloading-induced plastic strain at 1000 nm during the initial stages of unloading is relatively small. Nonetheless, this small amount of unloading-induced plastic strain has a significant impact on the derived modulus. Lastly, the four sets of data presented in Figure 5.8 suggest that the difference between standard and forced elastic unloading is not sensitive to the percentage of the unloading curve used in calculating the contact stiffness. Therefore, the presence of unloading-induced plasticity can have a substantial effect on the indentation-derived modulus for this multilayer system.

The relatively high stiffness of the substrate material in thin film applications can impact the indentation-derived hardness and elastic modulus of the structure. The

third case considered evaluates the effect of the substrate on the indentation-derived modulus. In this model, the Si substrate is replaced with a material representing the homogenized Al/SiC composite. The elastic modulus and stress-strain response of the effective substrate was determined from uniaxial compression modeling of an Al/SiC multilayer composite [104]. The modulus of the effective substrate is nearly half that of Si. Figure 5.9 shows the indentation-derived elastic modulus of the multilayer Al/SiC structure on an effective substrate for both standard and elastic unloading. Given a substrate that is approximately the same modulus of the multilayer system, the overall modulus still increases with indentation depth but to a much smaller extent compared to Figure 5.8. With an effective substrate the standard and forced elastic unloading results are essentially identical. This implies that the unloading-induced plasticity exhibits some degree of dependency on a substrate material substantially stiffer than the multilayer thin film structure.

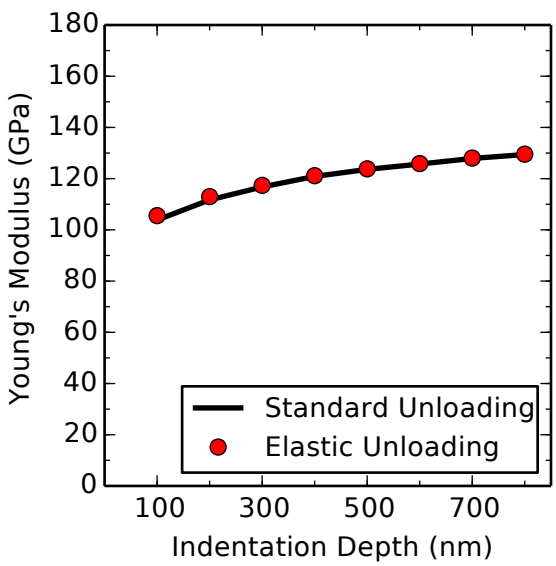

Figure 5.9: Indentation-derived Young's modulus of an Al/SiC multilayer system on an Al/SiC effective substrate [104] for standard and forced unloading.

Based upon these results, the unloading-induced plasticity can have a direct influence on the indentation-derived elastic modulus. At the deepest indentation

depth considered, the presence of plasticity results in an underestimation of actual composite modulus of the multilayers.

5.3.3 Cyclic Indentation Response

A common practice when performing nanoindentation experiments is to load and unload the indenter multiple times to minimize the possible effect of plastic unloading [15]. This practice has been shown to work well for homogeneous materials or single-layer thin films. When conducting nanoindentation on a 'normal' material, such as a homogeneous elasticplastic solid, one encounters both elastic and plastic deformation during loading. The elastic strains are recovered in the unloading phase. If the specimen then is cyclically reloaded and unloaded, the load-displacement curve will follow the prior unloading path, which characterizes the elastic nature of the process [38]. While this is true for most homogeneous elastic-plastic solids and single-layer thin films, it does not always hold true for multilayer thin films. Previous studies have shown that for a multilayer structure the unloading and reloading response is different and results in a hysteretic response [19]. The hysteresis of the load-displacement curve suggests the continual increase in plasticity during both the unloading and reloading phases.

The present study seeks to further investigate the effect of cyclic indentation on the indentation-derived modulus and how this relates to unloading-induced plasticity. To do so, the cyclic indentation response of the multilayer system discussed above will be modeled. The hysteresis of the load-displacement response will be analyzed to determine if it decreases at high cycle counts. The composite modulus derived from cyclic indentation will be compared to both those obtained from the standard and forced elastic unloading response of a single indentation. Lastly, the plastic strain induced by unloading during cyclic indentation will be considered.

Cyclic indentation was simulated by first loading the indenter to 80 mN, which corresponds to an indentation depth of approximately 775 nm. Unloading to 10% of the peak load, 8.0 mN, then follows. Subsequent cycles were carried out between these maximum and minimum loads, and a total of 15 cycles were performed. The simulation was initialized using displacement control boundary conditions. When the indentation load had reached more than 80% of the peak load, the boundary condition was updated to use load control. All subsequent cycles were then simulated using load control. The material properties are consistent with the previous model (Al/SiC multilayers on Si substrate) and forced elastic unloading is not considered.

The simulated load-displacement curves of the Al/SiC multilayer system for a total of 15 cycles is shown in Figure 5.10. In the figure, cycles 5, 10, and 15 are highlighted. For the purpose of clarity, the initial part of the first loading curve is not shown. It can be seen that the load-displacement loop persists from cycle to cycle, but it shifts left-to-right towards larger displacements. In other words, there is a tendency for the indenter to penetrate deeper as cycling continues under a constant load amplitude. This may be viewed as the indentation version of the 'cyclic creep' phenomenon typically observed under uniaxial loading [105]. It should be noted that the present numerical model only includes rate-independent plasticity; hence, increasing penetration is not caused by any viscous effect but purely a consequence of cyclic plasticity under highly constrained conditions. A stabilized hysteresis loop has not been reached after the completion of 15 cycles; however, the rate of change of indentation displacement is decreasing. This suggests that the amount of loading and unloading-induced plasticity in the metallic layers is slowly decreasing towards a constant value.

The indentation-derived elastic modulus was shown in the previous section to be dependent on the presence of unloading-induced plasticity. From Figure 5.10, it is apparent that the plastic state is changing in each cycle. Therefore, it is possible that

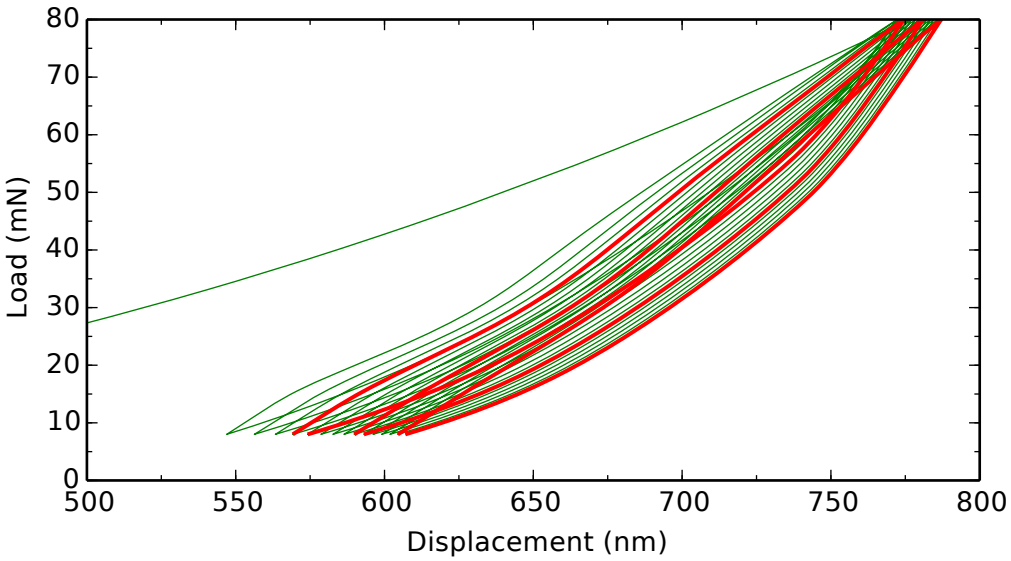

Figure 5.10: Simulated 15 full cycles of indentation load-displacement response for the Al/SiC multilayer system on Si substrate. Cycles 5, 10, and 15 are highlighted.

a relationship exists between the moduli derived from the forced elastic unloading and cyclic indentation. Figure 5.11 shows the indentation-derived elastic modulus for the Al/SiC multilayer system for cyclic as well as single cycle indentation over the indentation range considered. Between 750 and 800 nm, the indentation-derived standard and forced elastic unloading moduli differ by more than 10%. The modulus as derived from cyclic loading increases significantly from cycle 1 to cycle 2. It is noted that from cycle 2 onward, the indentation depth at each peak load increases with cycles. However, there is a decrease in penetration depth from cycle 1 to cycle 2. This may be attributed to the somewhat 'irregular' load-displacement response seen during the loading phase of the second cycle (Figure 5.10, which possibly is associated with the buckling of layers observed in Figure 5.5c).

The increase in the indentation-derived modulus between the first and second cycle is 8% and is the single largest change through the 15 cycles. After the first cycle, the indentation-derived modulus changes by less than 1% each cycle. After

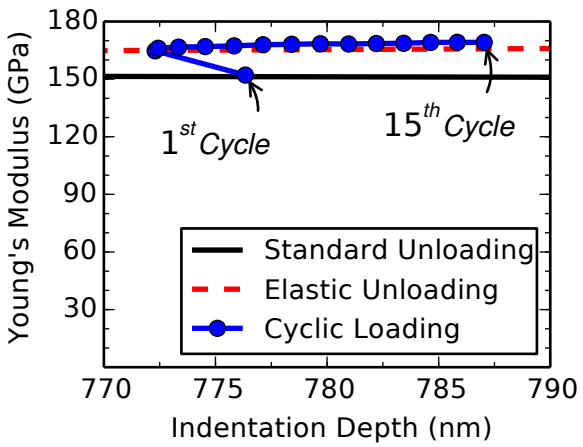

Figure 5.11: Indentation-derived Young's modulus of an Al/SiC multilayer system on Si substrate for cyclic indentation of peak load 80 mN compared to standard and forced elastic unloading of single cycle indentation.

15 cycles, the cycle-to-cycle variation in derived modulus is nearly zero. Although the plastic strain in the structure continues to increase cycle-to-cycle (Figure 5.10), the amount of plasticity that develops during the initial unloading is likely very low. Therefore, for this material system, the indentation-derived elastic modulus will not be affected by unloading-induced plasticity after the second cycle.

The cyclic indentation-derived modulus in Figure 5.11 suggests that the unloading-induced plasticity, at the beginning of the unloading, decreases substantially from cycle to cycle. Figure 5.12 shows the contour plots of the increase in EQPS at the early stages of unloading in different cycles. The figure confirms that with subsequent cycles there is very little plasticity at the beginning of unloading (where the elastic modulus is evaluated). During the first unloading cycle, the maximum amount of unloading-induced plasticity at 2% unloading is 0.015. Upon further cycling, the peak unloading-induced plasticity at 2% unloading decreases to approximately 0.0025 and remains constant through cycle 15. The unloading-induced plasticity between 100% and 98% of the peak load does not occur directly beneath the indenter after the first cycle and is located radially outward from the pile-up. Since the increase in

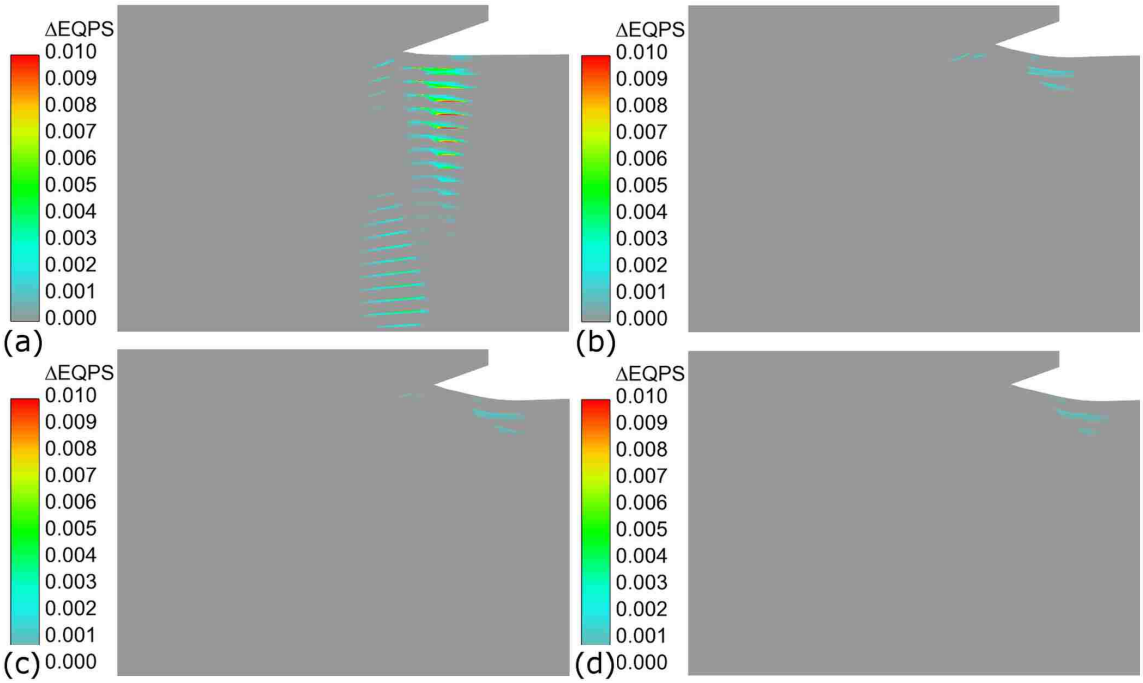

Figure 5.12: Unloading-induced equivalent plastic strain (ΔEQPS) at 98% of the maximum load of 80 mN during cyclic indentation for cycles 1, 5, 10, and 15.

plastic strain is not located directly beneath the indenter, it does not directly affect the modulus evaluation. This is observed in Figure 5.11 as the elastic modulus is nearly constant after the first few cycles.

The correlation between the modulus from the forced elastic unloading and cyclic loading indicates that a method exists to determine the modulus experimentally. For a given indentation depth, using a single cycle indentation result will likely under-predict the indentation-derived elastic modulus. Therefore, it is suggested that in actual nanoindentation testing of metal/ceramic multilayer systems, multiple indentation cycles should be performed to avoid the effect of any unloading-inducted plasticity.

5.3.4 Variations to the Multilayer System

The thickness of individual layers in metal and ceramic multilayer systems can vary depending on application and design. In the material system discussed above, the individual layers are assumed to be of equal thickness. To further explore the effect of unloading-induced plasticity, two variations of the Al/SiC multilayer system are considered. In both variations, the total thickness of the system is maintained to be the same as the original system, 2.05 μm, which consists of 41 alternating layers that are 50 nm thick. Both variations have 41 layers. In the first variation (a), each Al layer is 20 nm and each SiC layer is 80 nm for an Al to SiC thickness ratio of 0.25. In the second variation (b) each Al layer is 80 nm and each SiC layer is 20 nm for an Al to SiC layer thickness ratio of 4.0. Cyclic indentation is performed on each variation of the multilayer Al/SiC system to a similar indentation depth as shown in Figure 5.11.

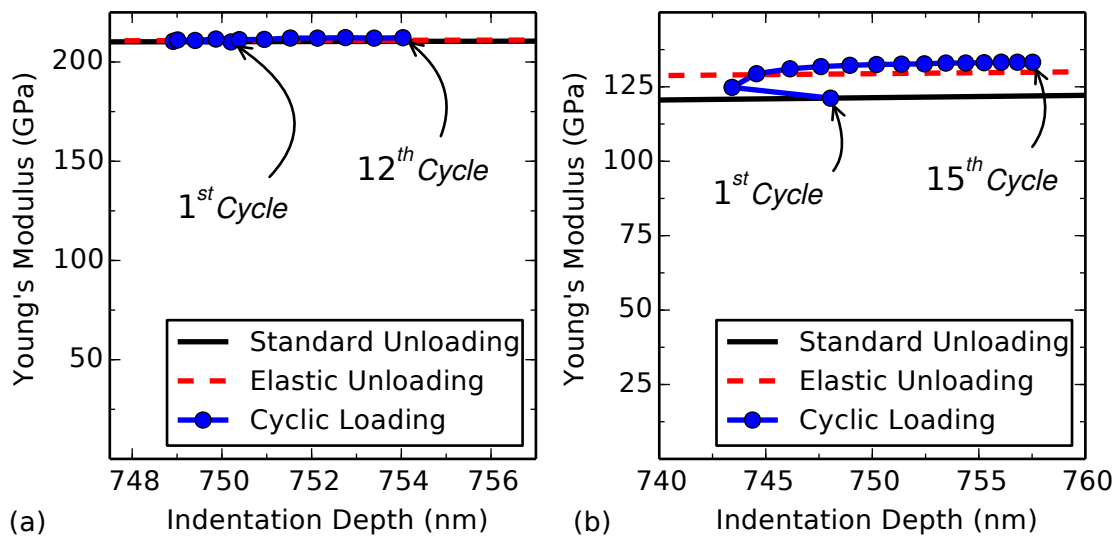

Figure 5.13: Indentation-derived Young's modulus of Al/SiC multilayer system from cyclic loading for varying thickness: (a) Al to SiC thickness ratio of 0.25 and (b) Al to SiC thickness ratio of 4.0.

The cyclic indentation-derived elastic modulus of the variations on the Al/SiC multilayer system is shown in Figure 5.13. Layer thickness ratios of 0.25 and 4.0 are shown in images (a) and (b), respectively. For a low thickness ratio, image (a), there is no appreciable difference between the standard and elastic unloading results. This suggests that, although the Al layers are constrained by thick SiC layer, any possible unloading-induced plasticity is overcome by the high stiffness and high thickness fraction of the SiC layers. The change in the modulus, cycle-to-cycle, is very small, which implies there is essentially no effect of unloading-induced plasticity in the thin Al layers. For a large thickness ratio, image (b), the unloading-induced plasticity does influence the derived modulus. Similar to the results shown in Figure 5.11, the indentation-derived modulus increases cycle-to-cycle. While the SiC layers are thinner than the original system, the SiC layers still impose a constraint on the Al layers causing unloading-induced plasticity. The Young's modulus from the first indentation is 121 GPa, and the final indentation is 133 GPa–an increase of 10%. Lastly, in both models the indentation depth decreases from the 1st to 2nd cycles for reasons discussed previously.

Figures 5.11 and 5.13 show that unloading-induced plasticity can affect the composite modulus of the multilayer system. Figure 5.13(a) shows that thin Al layers allow for very little unloading-induced plasticity, while Figure 5.13(b) shows the opposite. The effect of unloading-induced plasticity on elastic modulus as shown in Figure 5.13(b) is not significantly different than that shown in Figure 5.11. For layers of equal thickness, the modulus increases by 8%. For large thickness ratios (Al/SiC ratio of 4), there is a slightly larger increase in the modulus of 10%.

In addition to varying the thickness of the individual layers, a change in materials is considered. Silica (SiO_2) and Al multilayer films is an alternative to the Al/SiC multilayer film. Silica is much less stiff than SiC. The decrease in stiffness influences how the Al interacts with the surrounding ceramic. Silicon carbide constrains the

deformation of the Al, resulting in an increase in plastic strain. The Young's modulus of the multilayer Al/SiO_2 film is shown in Figure 5.14. The contact stiffness at the onset of unloading is calculated as described above in Section 5.2. The moduli derived from the standard and enforced elastic unloading of the Al/SiO_2 film are nearly identical. This confirms that pairing Al with the stiffer SiC is the source of unloading-induced plasticity.

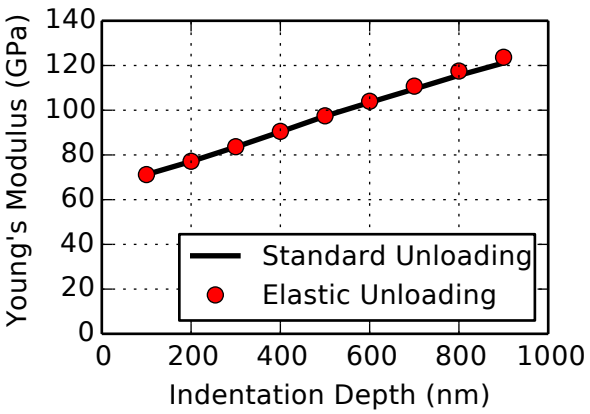

Figure 5.14: Indentation-derived Young's modulus of Al/SiO_2 multilayer system on Si substrate for standard and forced unloading.

Furthermore, the cyclic response of the multilayer Al/SiO_2 film is considered. The cyclic indentation-derived Young's modulus of the multilayer Al/SiO_2 is shown in Figure 5.15. The change in Young's modulus from the first cycle to the 15^{th} cycle is 5 GPa. Similar to the multilayer Al/SiC system, the indentation depth decreases when the indenter is cycled between a constant minimum and maximum load. After five cycles, the derived modulus is constant. Therefore, it is confirmed that using the contact stiffness after multiple indentation cycles to determine the multilayer modulus is a valid and useful approach.

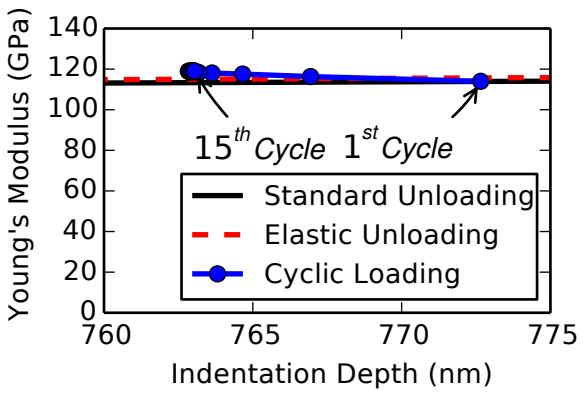

Figure 5.15: Cyclic Indentation-derived Young's modulus of an Al/SiO_2 multilayer system on Si substrate compared to standard and forced elastic unloading of single cycle indentation.

5.4 Conclusions

The effect of unloading-induced plasticity on the indentation-derived elastic modulus of a metal/ceramic multilayer composite was modeled and analyzed. The model system of alternating layers of Al and SiC on a thick Si substrate was the basis for the study. It was shown that plasticity develops during the unloading phase; most importantly, plasticity increases during the initial unloading. To elucidate the difference between standard unloading (which allows for plasticity) and purely elastic unloading, the unloading phase was forced artificially to remain elastic in a separate set of simulations. It was found that the elastic modulus determined by initial unloading is sensitive to the presence of unloading-induced plasticity. For indentation depths greater than 500 nm, the standard and forced elastic unloading results differed by as much as 20%.

Cyclic indentation of the model multilayer system was also analyzed. Beyond the first cycle, the cyclic indentation-derived modulus closely matched that obtained from the forced elastic unloading. After several cycles, the cycle-to-cycle difference in indentation-derived elastic modulus is less than 1%. At 15 cycles, there is no

discernible difference in the derived modulus cycle-to-cycle. Unloading-induced plasticity is also shown to be dependent on the ratio of Al to SiC layer thickness with little effect of unloading plasticity occurring for small ratios. Therefore, to avoid the effects of unloading-induced plasticity, it is suggested that a minimum of several indentation cycles be applied when experimentally characterizing multilayer thin films.

Chapter 6

Indentation-Induced Delamination of Multilayered Thin Films

6.1 Introduction

Multilayer thin films can possess enhanced mechanical properties compared to single-layer films, such as strength, ductility, and high damage tolerance. Though multilayer films have favorable mechanical properties, the interaction between the individual layers can be complex. As described in previous chapters, the complicated stress and deformation fields of multilayer films are strongly dependent on the multilayer geometry and material selection. This complexity can lead to indentation-induced damage in the multilayer thin film. Postmortem analysis of multilayer films have shown indentation-induced damage for various material combinations [6, 73–77]. In this chapter, indentation-induced damage of the multilayer Al/SiC film will be studied. Specifically, how indentation-induced damage may affect the indentation-derived hardness and Young's modulus is considered.

Indentation-induced damage of the multilayer Al/SiC film has been observed experimentally by Chawla [10], Sun [12] and Singh [18]. In these studies, multilayer Al/SiC films consisting of approximately 40-50 alternating layers of material were subjected to indentation with a Berkovich indenter. Focused ion beam (FIB), scanning electron microscopy (SEM), and FIB tomography were used to study the internal structure of the films. Each study found void nucleation and growth in the Al, cracking and bending in the SiC layers, and delamination at the multilayer/Si interface. Because these analyses take place after the indentation has occurred, it is difficult to experimentally measure the effect of damage and delamination on indentation-derived hardness and Young's modulus.

In order to better understand the effect of damage and delamination on indentation-derived hardness and Young's modulus, a series of finite element models were created. The first of these models is a single-layer Al film on a Si substrate (see 3.3). Cohesive elements (described below) are inserted at the Al/Si interface and comparisons of hardness and Young's modulus are made between the perfectly bonded model and cohesive element model. The second set of models are based on the 41-layer Al/SiC multilayer film described in previous chapters. Two variations to the baseline 41-layer model are considered. The first model has cohesive elements at the multilayer/Si interface only and the second model has cohesive elements at both the multilayer/Si interface and at various Al/SiC interfaces. The effects of delamination load-displacement response, hardness, and Young's modulus is measured. Lastly, the effect of cohesive zone model parameters are discussed.

6.2 Model Description

The finite element model used in this series of analyses is similar to that discussed in previous chapters. The single-layer Al film is assumed to be 1 μm thick on a 41 μm

thick Si substrate. Each layer in the multilayer Al/SiC film is assumed to be 50 μm thick on a 41 μm thick Si substrate. Aluminum is the top most (in contact with the indenter) and bottom-most (adjacent to the substrate) material.

A conical diamond indenter with a semi-angle of 70.3° is assumed. This indenter geometry results in the same projected contact area for a given depth as that of a Berkovich indenter in common nanoindentation experiments. Use of the conical indenter is a practical way to model the indentation process in a two-dimensional setting [82]. Each model is axisymmetric with the left boundary being the symmetry axis. Each specimen is 40 μm in the lateral span (radius). During deformation the left and bottom boundaries are allowed to displace only in the axial and radial directions, respectively. The right boundary is not constrained. The top surface of each specimen, when not in contact with the indenter, is also free to move. When contact with the indenter is established, the surface portion engaged by the indenter directly interacts with the indenter. The coefficient of friction between the indenter and the top surface is 0.1, which is a typical value for the diamond/metal contact surface [83, 84].

The Young's modulus for Al is assumed to be 59 GPa. Nanoindentation of single-layer Al provided the modulus for this material. The Poisson's ratios for Al is 0.33. The plastic response of Al was based on the tensile loading data of single-layer Al with initial yield strength of 200 MPa. Rate-independent isotropic elastic-plastic response was assumed with plastic yielding following the von Mises criterion with isotropic hardening and the incremental flow theory. The piecewise linear strain hardening response features hardening slopes of 199.33 MPa from initial yielding up to the strain of 50.51% and then 39.97 MPa up to the strain of 300.68%, beyond which perfect plasticity ensues.

The Young's modulus for SiC is assumed to be 277 GPa. Nanoindentation of single-layer SiC films provided the modulus. The somewhat lower modulus of SiC,

relative to crystalline SiC (which is around 410 GPa), is due to the fact that the physical vapor deposited SiC layers in the present case were amorphous [61]. The Poisson's ratios for SiC is taken 0.17. SiC is a very brittle material; nevertheless, a very high yield point of 8,770 MPa (estimated from the indentation hardness of a single-layer SiC film [9] was used followed by perfect plasticity. This assumption is necessitated by the fact that a purely elastic SiC in the model will generate unrealistically high loads during the indentation simulation, and it is validated by the fact that in the experiment the SiC layers exhibited a glassy/plastic-type response due to the amorphous nature of the film [62].

Both the Si substrate and diamond indenter are assumed to remain elastic. The Young's modulus and Poisson's ratio of the Si substrate are 187 GPa and 0.28, respectively. The Young's modulus and Poisson's ratio of the diamond indenter are 1,141 GPa and 0.07, respectively. The indenter geometry-dependent dimensionless parameter is assumed to be 1.06 and the composite Poisson's ratio used in the calculation of the composite Young's modulus is assumed to be 0.25 (see Section 3.2). All the interfaces between different materials in the composite structures are modeled as perfectly bonded, unless otherwise noted below.

Approximately 100,000 fully integrated linear axisymmetric elements are used in the finite element model with a finer mesh size near the upper-left corner of the test material. The element size near the indenter tip is approximately 8 nm and increases in size far from the indenter. The indenter consists of approximately 8,000 elements with an element size of approximately 15 nm near the tip. The mesh was created using CUBIT (Sandia National Laboratories; Albuquerque, NM). The finite element program ABAQUS (Version 6.13, Dassault Systemes Simulia Corp.; Providence, RI) was used to carry out the analysis.

6.2.1 Modeling delamination

Postmortem analysis has shown that the following damage mechanisms are possible during indentation: void nucleation and growth in Al, cracking in SiC, and delamination at the multilayer/substrate interface. In this study cohesive zone elements are used to model the delamination at the substrate. The cohesive zone approach is uniquely designed to model bi-material interface failure [79, 106]. Though originally designed to model the crack growth in an homogeneous material, it was quickly discovered that the cohesive zone approach was applicable to bi-material interface as well. At this time, no attempt is made to explicitly model the crack nucleation and growth inside both the Al and SiC. Nonetheless, to account for the effect of cracking in the multilayer, cohesive elements are used at the Al/SiC interface. Cracking near the interface and through the thickness of the SiC has been observed; therefore, using cohesive elements at the Al/SiC interface is an idealized approach.

The most common method used to describe the constitutive response of cohesive elements is with a traction-separation law as shown in Figure 6.1. This relationship is useful for modeling delamination because the user can relate stresses to separation at the interface in both the normal and tangential directions. The traction-separation law is composed of two main components, loading and unloading. The relationship has a stiffness of K until a critical stress (t^0), or interface strength, at displacement δ_0 is reached. Upon reaching the critical stress, or elastic limit, damage occurs for $\delta > \delta_0$. Damage continues until a separation distance of δ_{sep} is reached, at which point the fracture energy has been released. At the point of failure, the traction-separation relationship accounts for an amount of energy equal to the critical fracture energy, G_c, of the material or interface. Though the constitutive response has a physical basis, it is nonetheless an engineering representation of complex phenomenon.

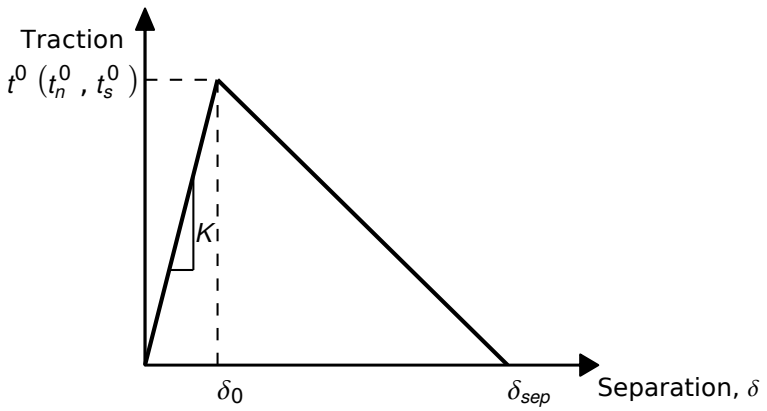

Figure 6.1: A graphical representation of the traction-separation relationship that defines the cohesive element response

ABAQUS has a variety of damage initiation models that can be used in conjunction with cohesive element based on a traction-separation law. The simplest damage initiation relationship available is the maximum nominal stress ratio (`MAXS`). This is a damage model that is based on the maximum ratio of normal and shear tractions to the critical normal and shear tractions. The maximum nominal stress ratio is defined as

$$max \left\{ \frac{\langle t_n \rangle}{t_n^0}, \frac{t_s}{t_s^0} \right\} = 1 \tag{6.1}$$

where t_n is the normal traction modified with the Macaulay bracket with the standard interpretation (i.e. damage does not initiate in a pure compressive state), t_n^0 is the critical normal stress, t_s is the shear stress, and t_s^0 is the critical shear stress. When the maximum of these ratios reach 1.0, damage initiates and the cohesive element begin to accumulate damage.

Once damage initiates, damage evolution is assumed to be linear and based on effective displacement. Damage evolution is controlled by a scalar damage variable, D, which represents the overall damage in the element. The scalar damage variable monotonically evolves from 0 to 1 upon further loading post damage initiation. As

damage evolution is based on separation, it is useful to define an effective displacement which is defined as

$$\delta_m = \sqrt{\langle \delta_n \rangle^2 + \delta_s^2} \tag{6.2}$$

where δ_n is the tensile-only component of the normal separation and δ_s is the shear separation. The scalar damage variable is then defined as

$$D = \frac{\delta_m^f \left(\delta_m^{max} - \delta_m^0\right)}{\delta_m^{max} \left(\delta_m^f - \delta_m^0\right)} \tag{6.3}$$

where δ_m^f is the effective displacement at complete failure, δ_m^0 is the effective displacement at damage initiation, and δ_m^{max} is the maximum value of the effective displacement attained during the loading history. Once D obtains a value of 1, the damage evolution is complete and the element is deleted. The combination of damage initiation and evolution completely define the constitutive behavior of the cohesive element.

Populating the damage initiation and evolution models require material data. Studies have been performed to gain further insight into the interfacial strengths associated with the materials of interest. Dandekar and Shin [67] performed molecular dynamics based simulations to study the Al/SiC interface strength. Gall, et al. [68] studied the Al/Si interface using atomistic simulations. Lastly, Dandekar and Shin [69] also performed molecular dynamics based simulations to study the Al_2O_3/Al interface. The traction-separation relationships these studies produced are shown in Figure 6.2. Of these three interfaces, the Al/Si interface is the strongest. All the derived traction-separation appear much stronger than the bulk material. Chawla, et al. [10] observed that voids do not originate between the Al and SiC layers. This suggests that the strength of the Al/SiC interface (the weakest of the three interfaces) is higher than the stress required for void formation in the Al.

Simulations were performed using the traction-separation data shown in Figure 6.2. The models showed that the interface is indeed much stronger than the bulk material

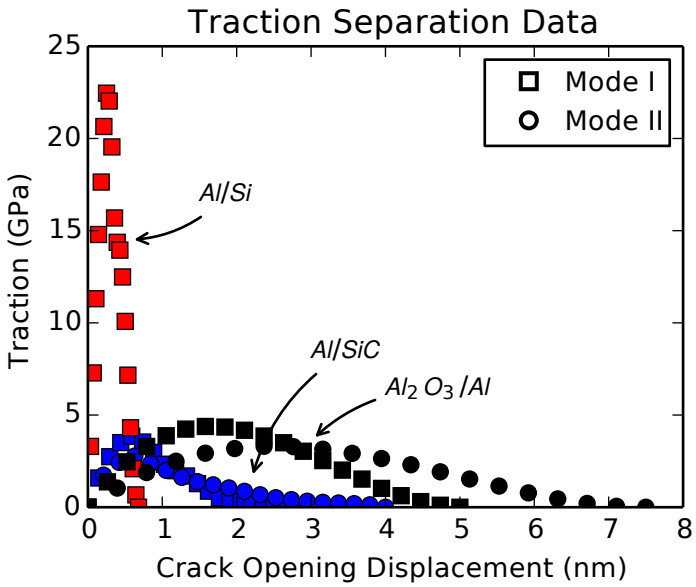

Figure 6.2: Derived traction-separation data for the (FCC) Al/(3C-SiC) SiC [67], [100] Al/[100] Si [68], and (R3-c) Al_2O_3/(FCC) Al [69] material interfaces. Squares represent data for Mode I separation and circles represent data for Mode II separation.

as damage never initiated in the cohesive elements. With cohesive elements based on these traction-separation data, the Al and SiC behave as though the layers are perfectly bonded (i.e. the original assumption). Though simulations have shown that the Al/Si interface is ideally stronger than the bulk Al or Si, delamination at the Al/Si interface has been observed experimentally. It is theorized that delamination occurs at the Al/Si because of imperfections, such as oxides, in the interface or in the surrounding bulk material very near the interface. Currently, the fidelity of the current modeling approach cannot capture possible imperfections; therefore, a weaker interface is assumed to provide insight into the relationship between delamination and indentation-derived variables.

To study the effect of delamination at the Al/Si interface, the critical normal, t_n^0, and shear stress, t_s^0, were based on the bulk properties of Al. The nominal value of both the critical normal and shear traction at the Al/Si interface was assumed to be

200 MPa. The critical separation, δ_{max}, is assumed to be 0.4 nm. The critical normal and shear tractions were varied between 200 and 400 MPa to gain greater insight into how the interface behaves. The elastic properties of the cohesive element are based on the bulk Al properties. The elastic moduli in the normal and shear directions are 59 and 28 GPa, respectively. These properties apply to both the single-layer and multilayer film models. For the model with cohesive elements at the Al/SiC interface, the Al/SiC interface was assigned similar properties.

In the finite element model, the cohesive element is a separate element block that is placed at a material interface. Since the physical thickness of the material interface is nearly zero, the cohesive element is assumed to have zero initial thickness. In both the Al film and multilayer Al/SiC models, cohesive elements are inserted at the Al/Si substrate interface. For the multilayer model with cohesive elements at multiple Al/SiC interfaces, the cohesive elements are located between the first four layers from the substrate as well as between six layers approximately 1.33 μm from the substrate.

Previous studies have shown that in ABAQUS Standard, it may be difficult to obtain a converged solution because as cohesive elements fail a "zipper effect" occurs [106]. Refining the entire mesh at the interface can reduce this effect but is costly. Alternatively, a more efficient approach is to use a concept referred to as *over-meshing*, where the cohesive elements have a higher mesh density than the surrounding structure. The cohesive elements are then attached to the surrounding structure using tied contact (`*TIE`). For all simulation results shown here, there are three cohesive elements for every one element in the surrounding structure, for an over-mesh of 3 to 1. Furthermore, to aid in convergence, viscous regularization is applied to the cohesive elements. In all models, the viscous coefficient is 0.01%. Sensitivity studies showed that the value of the viscous coefficient had negligible effects on the load-displacement response but greatly aided in convergence. Also, it was found that when cohesive elements are loaded in compression, they are prone

to inverting. To prevent cohesive element inversion, `NODE TO SURFACE` contact was enforced between each Al and SiC layer as well as the Si substrate.

6.3 Model Results

To study the effect of delamination at material interfaces in a thin film, two models are analyzed. First, a single-layer Al film on a Si substrate with cohesive elements at the film/substrate interface is considered. Second, two variations on the multilayer Al/SiC film are considered. The load-displacement response of the models with cohesive elements and those without are compared. The indentation-derived Young's modulus and hardness are calculated and compared to properties from a model with perfectly bonded layers. The normal and shear tractions at a single element are also analyzed. Finally, the stress distribution throughout the multilayer film with and without cohesive elements is considered.

6.3.1 Single-layer Al Film

The single-layer Al film presented in Section 3.4.1 was used to study the behavior of a single-layer film with cohesive elements. The single-layer film model is a useful tool to determine if the presence of the cohesive elements have any effect on the load-displacement response. The Al is 1 μm thick and is joined to a thick substrate with cohesive elements. See Section 3.4.1 for further information about the single-layer Al film model.

The load-displacement response of the single-layer Al film with and without cohesive elements is shown in Figure 6.3 for an indentation depth of 500 nm. It can be seen that the load-displacement response of both models are identical. This suggests two things. First, the use of cohesive elements and film-to-substrate contact

at the interface does not affect the indentation modeling results. Second, as expected, the single-layer film is not susceptible to delamination at the Al/Si interface.

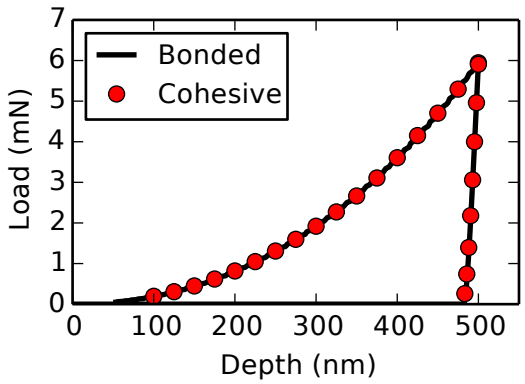

Figure 6.3: Indentation load-displacement data for a single-layer Al film with and without cohesive elements for an indentation depth of 500 nm. 'Bonded' refers to a perfect interface (no cohesive elements) and 'Cohesive' refers to an interface composed of cohesive elements.

The indentation-derived hardness and Young's modulus for the single-layer film is shown in Figure 6.4 for an indentation range of 10 to 50% of film thickness. In each image, the results of the model with cohesive elements are very similar to the model without. Though they are similar, they are not identical. The small difference in both the hardness and modulus can be attributed to the interfacial compliance at the film/substrate interface, which includes both local sliding and Mode I 'opening' that is below the critical traction. The cohesive elements allow for the interface to shear. The shear at the interface leads to a small change in the projected contact area; hence, the small difference in the models. During both loading and unloading, the cohesive elements remain elastic, as damage is never initiated. The presence of cohesive elements at the film/substrate interface in a single-layer Al film was shown to have little effect on indentation-derived variables.

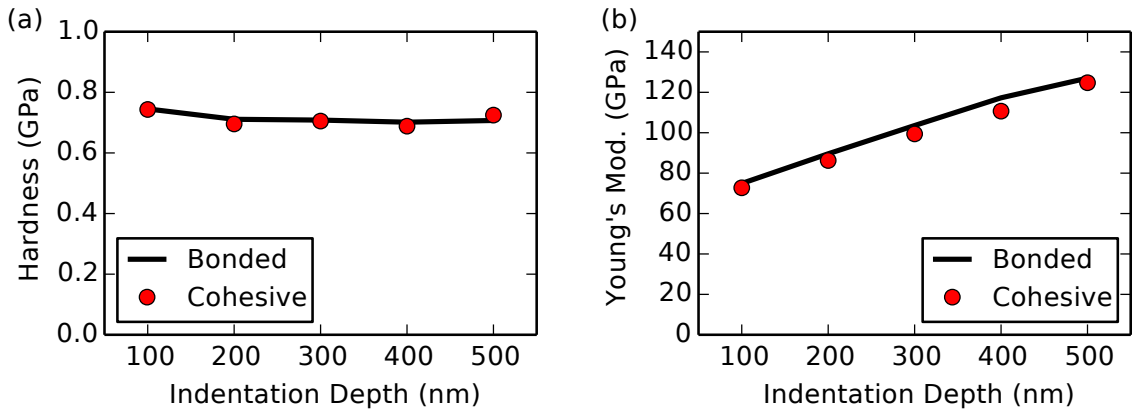

Figure 6.4: Indentation-derived (a) hardness and (b) Young's modulus of a single-layer Al film with and without cohesive elements. 'Bonded' refers to a perfect interface (no cohesive elements) and 'Cohesive' refers to an interface composed of cohesive elements.

6.3.2 Multilayer Al/SiC Film

The multilayer structure in the Al/SiC results in a much more complex indentation response. As discussed previously, delamination and void growth has been experimentally observed in Al/SiC specimens. To study the effect of delamination in the multilayer film, cohesive elements are used at the multilayer/substrate interface as well as between Al and SiC layers. The indentation load-displacement response, hardness, Young's modulus, and stress-time histories for the multilayer film are presented.

The load-displacement response of the multilayer Al/SiC film with cohesive elements at only the multilayer/substrate interface is shown in Figure 6.5. In this figure, the critical normal and shear stress is varied between 200 and 400 MPa, respectively. Red circles denote the load at which delamination occurs. In images (a-c), delamination occurs at one loading and unloading event. In image (d), delamination occurs once during loading and twice during unloading.

In Figure 6.5(a-b) the normal critical traction is held constant at 200 MPa. In both images, delamination occurs at 23 and 12 mN during loading and unloading, respectively. The increase in the shear critical traction (image b) does not cause a change in the load at which delamination occurs. This suggests that delamination

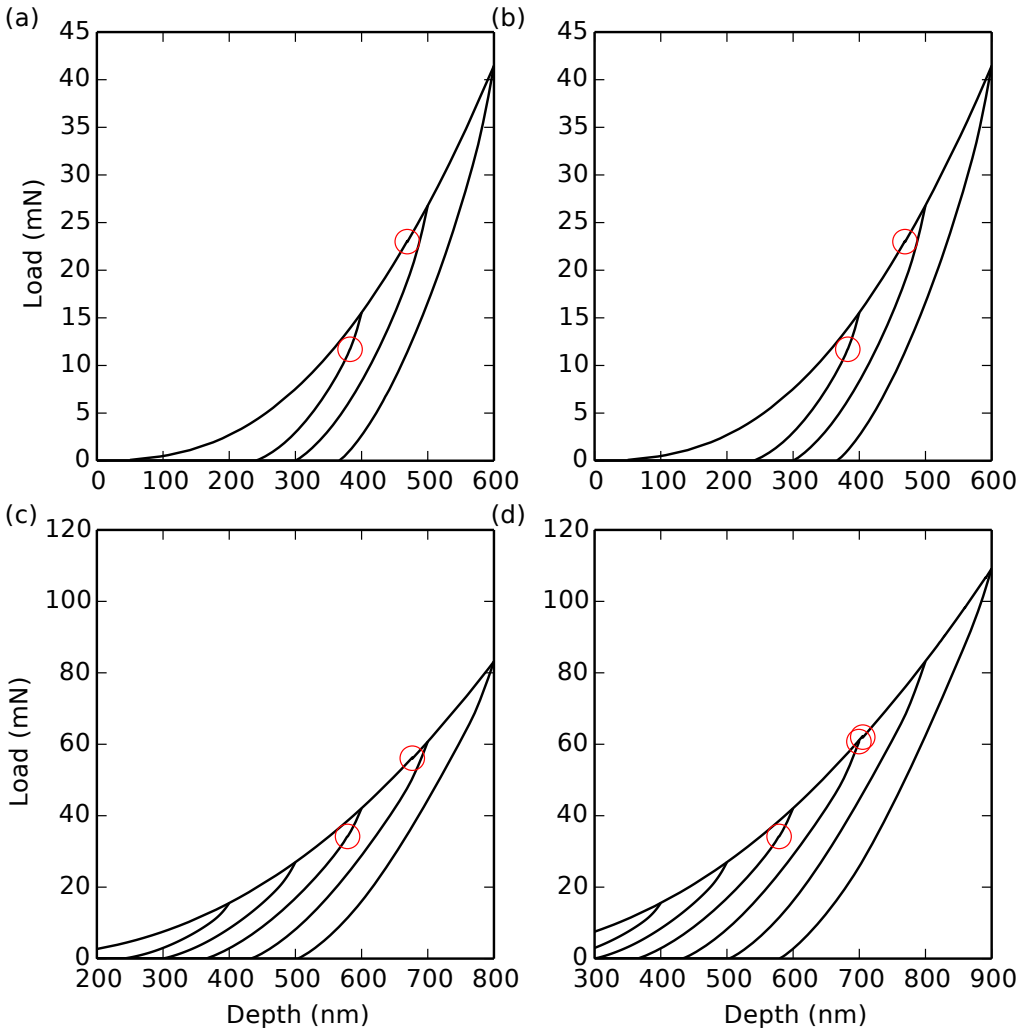

Figure 6.5: The indentation load-displacement response of the multilayer Al/SiC film with cohesive elements at the Al/Si interface with variations in normal and shear critical traction. (a) t_n^0=200 MPa, t_s^0=200 MPa (b) t_n^0=200 MPa, t_s^0=400 MPa (c) t_n^0=400 MPa, t_s^0=200 MPa (d) t_n^0=400 MPa, t_s^0=400 MPa. Red circles denote the load at which delamination occurs.

in these two sets of models is dominated by an tensile axial (normal) stress at the interface. In Figure 6.5(c), the load at which delamination occurs is increased. During loading (56 mN), damage initiation is caused by shear at the interface. During unloading (34 mN), damage initiation is dominated by a tensile axial stress at the interface. In Figure 6.5(d), delamination occurs at three separate loading conditions. First, delamination occurs during loading at 62 mN and damage initiation is driven by both axial and shear stresses. For both unloading-induced delamination events (34 and 61 mN) tensile axial stress is the main factor in damage initiation. From this set of data, it is observed that the delamination during loading can be attributed to both tensile axial and shear stresses, while delamination during unloading is dominated by tensile axial stress.

The load-displacement response for both versions of the multilayer Al/SiC film is shown in Figure 6.6. In this figure, 'bonded' refers to the original, perfectly bonded model, 'Al/Si' has cohesive elements only at the substrate interface, and 'Al/SiC' has cohesive elements at both substrate and between Al and SiC. The critical traction in both the normal and shear directions is assumed to be 200 MPa at the Al/SiC interface. In Figure 6.6(a), it can be seen that the load-displacement response is very similar for all three models. The peak load varies by less than 2%, even though delamination has occurred in the 'Al/Si' model. Figure 6.6(b) shows a comparison between the 'Bonded' and 'Al/SiC' model up to 700 nm. The response is similar until the 'Al/SiC' model undergoes delamination at the multilayer/substrate interface at 50 mN, resulting in a difference of 3% in peak load. Though cohesive elements are present at multiple Al/SiC boundaries, the delamination still occurs at the substrate. These images suggest that the presence of cohesive elements do not, in themselves, cause any significant difference in the load-displacement response of structure. Though the peak loads vary by less than 5%, a change in the projected contact area or unloading response can cause more substantial differences in derived hardness or Young's modulus.

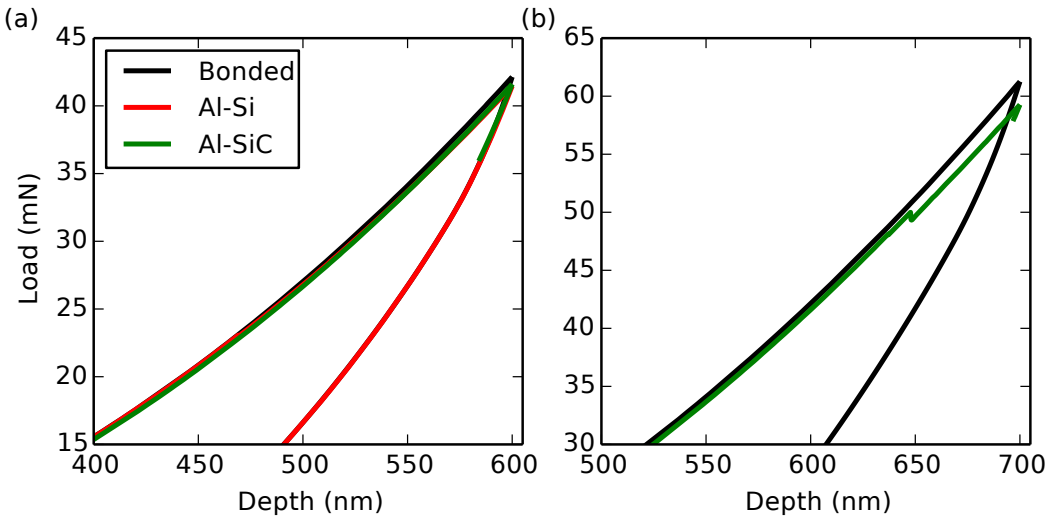

Figure 6.6: The indentation load-displacement response of the multilayer Al/SiC film with cohesive elements at the Al/Si interface and between Al/SiC layers for indentation depths of (a) 600 nm and (b) 700 nm.

Indentation-derived variables

The hardness as a function of indentation depth of the multilayer Al/SiC with and without cohesive elements is shown Figure 6.7 for a range of critical normal and shear tractions. In the figure, results for both cohesive element models are shown. Up to an indentation depth of 600 nm, the difference in the hardness result is small. Above 600 nm, the difference in derived hardness becomes larger, with a maximum change in hardness of -13%. A change in hardness comes from both a change in peak load (as shown in Figure 6.6(b)) as well as a change in the projected contact area. The cohesive elements, particularly post-delamination, allow the structure to move more freely, resulting in an increase in projected contact area.

Over a large portion of the indentation range considered, the hardness does not vary by more than 10%, even though delamination has occurred. The Young's modulus on the other hand is much more sensitive to delamination. The indentation-derived Young's modulus of the multilayer Al/SiC film with and without cohesive

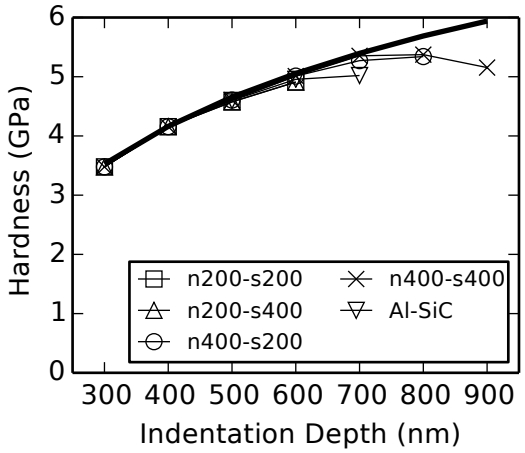

Figure 6.7: Indentation-derived hardness of the multilayer Al/SiC film for a range of critical normal and shear tractions. The curves 'n200-s200', 'n200-s400', 'n400-s200', and 'n400-s400' represent the critical normal and shear tractions, respectively, at the Al/Si interface. 'Al/SiC' represents the model with cohesive elements at both Al/Si and Al/SiC interfaces with critical tractions of 200 MPa. The perfectly bonded model is the solid line.

elements is shown in Figure 6.8. Results for cohesive elements at the substrate and substrate/layer boundaries are shown in the figure. At an indentation depth of 300 nm, the Young's modulus varies by as much as 6% and the difference grows to as large as 22% at 900 nm. The most significant difference in Young's modulus comes after delamination has occurred, i.e. when the slope of the modulus-depth response becomes negative. In all model variations, damage is initiated at multiple locations ($MAXSCRT = 1$, Equation 6.1, and $D < 1$, Equation 6.3) but delamination ($D = 1$) occurs only at the Al/Si interface.

Four of the five cases shown have cohesive elements only at the Al/Si interface. In general, the presence of the cohesive elements (pre-delamination) result in a decrease in the derived modulus. Similar to the hardness, this softening behavior can be attributed to multiple factors. First, the projected contact area increases as described above. For example, for the case of t_n^0=400 MPa and t_s^0=400 MPa, the projected

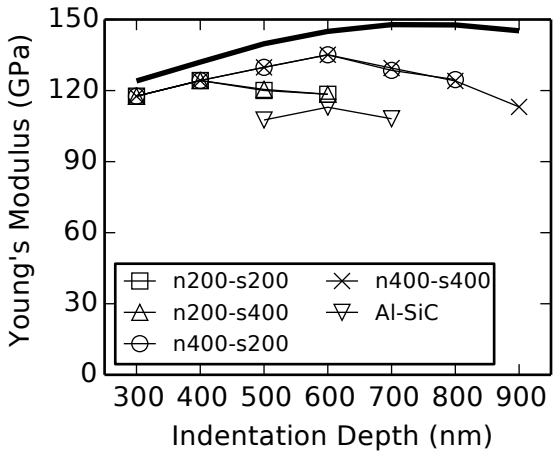

Figure 6.8: Indentation-derived Young's modulus of the multilayer Al/SiC film for a range of critical normal and shear tractions. The curves 'n200-s200', 'n200-s400', 'n400-s200', and 'n400-s400' represent the critical normal and shear tractions, respectively, at the Al/Si interface. 'Al/SiC' represents the model with cohesive elements at both Al/Si and Al/SiC interfaces with critical tractions of 200 MPa. The perfectly bonded model is the solid line.

contact area is 11% greater than the perfectly bonded model at an indentation depth of 900 nm. Second, the contact stiffness at the onset of unloading, S, decreases when the interface is modeled with cohesive elements. For the same material set (n400-s400), at an indentation depth of 900 nm, S has decreased by 15%. The combination of these two effects cause the large decrease in the indentation-derived Young's modulus. For the last case ('Al/SiC' - cohesive elements located at substrate and between layers) the change in modulus is even greater, 23-27% lower than the perfectly bonded model. As with the other four models, the change in modulus is due to the increase in the projected contact area and the decrease in the contact stiffness at the onset of unloading.

When assuming a perfectly bonded interface between materials, the SiC film imparts a constraint on the Al film. During indentation, the Al wants to flow away from the indentation sight. The bulk SiC, and the strong Al/SiC interface, force the

Al to deform plastically as it moves away from the indentation center. In addition, surrounding the SiC with Al allows the SiC to exhibit greater flexibility resulting in increased pile-up at the indentation location. Allowing for damage to occur effectively relaxes the constraints created by the Al and SiC multilayer. Prior to damage initiation and evolution, interfacial compliance relieves the constraint imposed by the SiC on the Al layers. The Al is now more able to flow away from the indentation center, effectively increasing the contact area. After damage occurs at the Al/Si interface, the contact stiffness decreases. The stiff substrate provides an additional constraint on the multilayer. Damage at the interface relaxes the influence of the Si substrate, causing the multilayer to decrease in stiffness, particularly during unloading. Lastly, damage during unloading can exacerbate the decrease in contact stiffness at the onset of unloading.

Indentation-induced damage

As discussed previously, damage initiation can be caused by either normal or shear tractions at the interface. To better understand how normal and shear stresses at the interface contribute to damage initiation, the normal and shear tractions at a single element during loading and unloading is examined. Figure 6.9 shows the normalized normal and shear traction response at a single element during loading and unloading, respectively. This data set in from the model variation with cohesive elements at only the multilayer/substrate interface. Both tractions are normalized by the critical normal and shear tractions, both of which are equal to 200 MPa for this data set. In this figure, the data is pulled from the first element to fail at the Al/Si interface. During loading and unloading, the element of interest is 1.8 and 1.6 μm, respectively, from the indentation center. This is the radial distance from the axis of indentation prior to deformation.

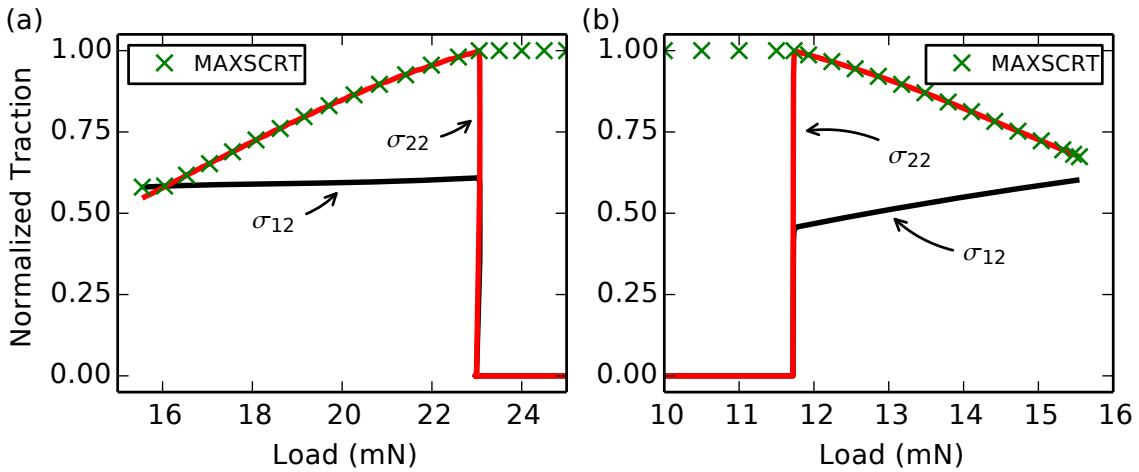

Figure 6.9: Normalized traction response in a cohesive element while (a) loading to 500 nm and (b) unloading from 400 nm. Both the critical normal and shear tractions are equal to 200 MPa.

The dominant traction leading to damage initiation in both loading and unloading is a tensile axial (normal) stress at the interface. The damage initiation criterion, `MAXSCRT`, is also plotted in this figure (see Equation 6.1). The damage initiation criterion follows the normal traction during both loading and unloading. In both cases, the shear traction is nearly half that of the critical shear traction. Previous studies [17] have shown that a large area of tensile axial stress is present at the Al/Si interface. For this given set of material parameters, it is an axial tensile stress that leads to damage initiation and delamination.

The indentation-derived Young's modulus was shown to be sensitive to the effect of interfacial sliding and delamination possible with cohesive elements at both the Al/Si and Al/SiC interfaces. Figure 6.10 shows the normalized normal and shear tractions in a cohesive element at the Al/Si interface during loading to 700 nm. The cohesive element is 1.8 μm from the axis of indentation. The loading behavior with multiple layers of cohesive elements (both Al/Si and Al/SiC) is different than that of a single layer of elements at the Al/Si interface. The cohesive elements allow more

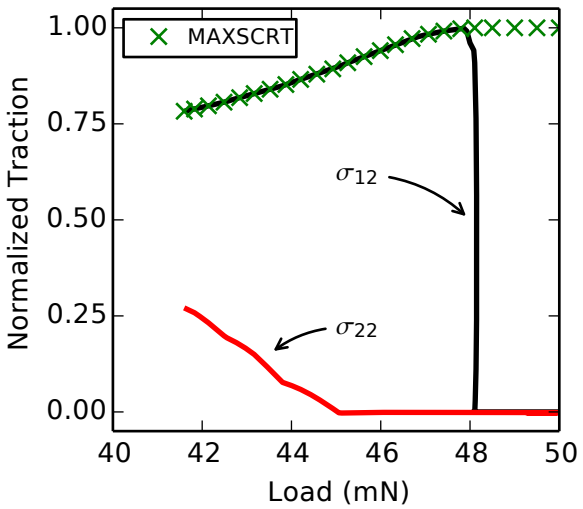

Figure 6.10: Normalized traction response in a cohesive element at the Al/Si interface during loading to 700 nm. Both the critical normal and shear tractions are equal to 200 MPa.

motion at the interface between layers which results in a reduction of the axial stress in the film. Though the axial stress has decreased, shear stress is still large and dominates the damage initiation at the Al/Si interface. Furthermore, as the shear stress increases, the axial stress begins to decrease. Therefore, damage initiation is dependent on shear stress when cohesive elements are used at multiple layers.

Analyzing the normal and shear stress in a single cohesive element at the Al/Si interface has shown that either stress can lead to damage initiation. In Section 6.3.2 it was shown that for an indentation depth of 600 nm, the perfectly bonded model has a modulus 18% greater than the modulus of the model with cohesive elements at only the Al/Si interface. The difference in modulus is attributed to an increase in projected contact area and a decrease of S. The decrease in S can be attributed to delamination prior to the onset of unloading. Figure 6.11 shows the axial stress state in both structures at 98% of the peak unloading. Between 98-100% is the range in which a linear regression is used to fit the load-displacement data to calculate S.

At 98% of peak load, the axial stress is much lower in the cohesive element model than the perfectly bonded model. Delamination allows the multilayer film to move away from the substrate freely during unloading; therefore, the contact stiffness at the onset of unloading is decreased.

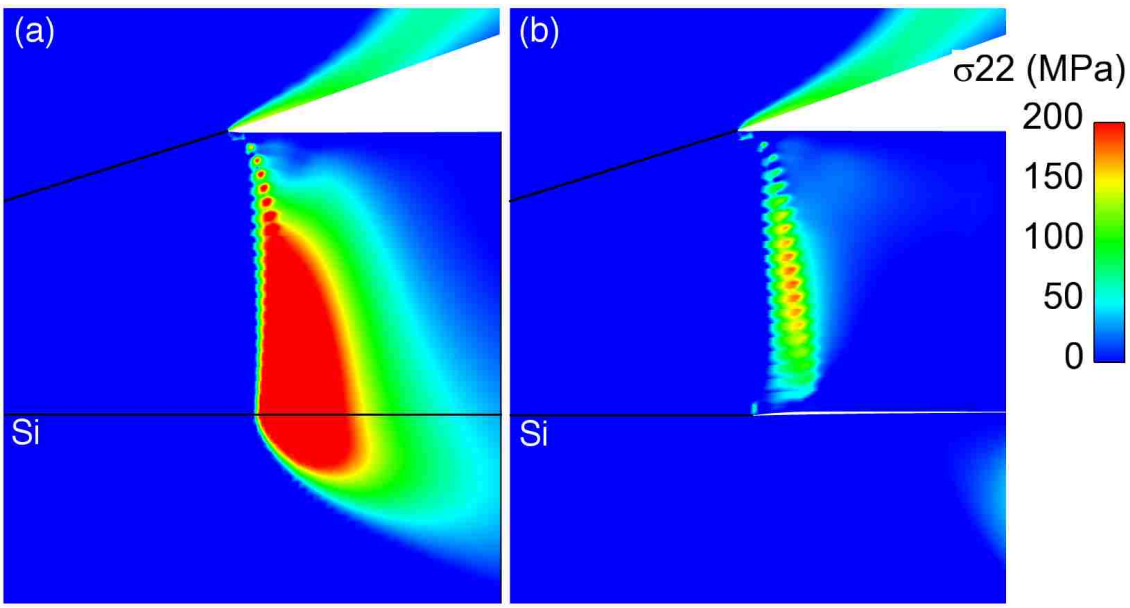

Figure 6.11: Axial stress (σ_{22}) in the multilayer Al/SiC at 98% of the peak load for an indentation depth of 600 nm for (a) perfectly bonded layers and (b) cohesive elements at the Al/Si interface.

A comparison of the axial stress state in the perfectly bonded model and the model with cohesive elements at both Al/Si and Al/SiC interfaces is shown in Figure 6.12 for an indentation depth of 700 nm at the peak load. The stress state in the multilayer with cohesive elements is much lower than the model with perfectly bonded interfaces. The axial stress in the multilayer decreases when cohesive elements are used at more than the multilayer/substrate interface (compare Figure 6.11(b) and Figure 6.12(b)). The interfacial compliance at the material boundaries allows the Al to flow more freely, leading to the decrease in stress. The decrease in stress is a contributing factor in the decrease in both indentation-derived hardness and Young's modulus.

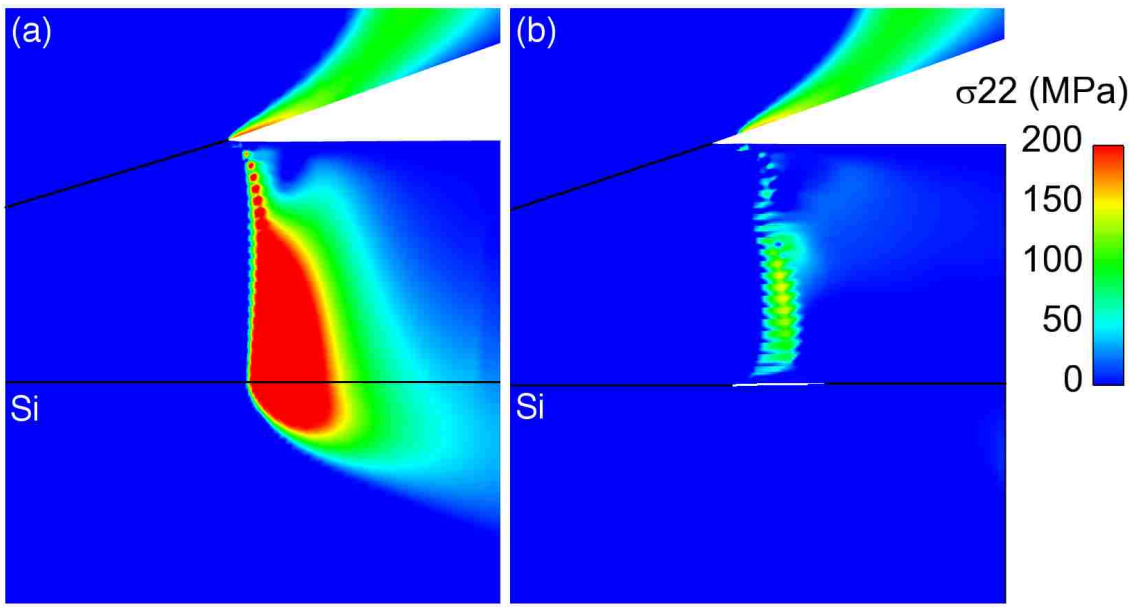

Figure 6.12: Axial stress (σ_{22}) in the multilayer Al/SiC prior to unloading for an indentation depth of 700 nm for (a) perfectly bonded layers and (b) cohesive elements at both the Al/Si and multiple Al/SiC interface.

To gain even greater insight into the stress state after damage initiation, the axial stress in the multilayer film is considered.

Figures 6.11 and 6.12 showed how damage prior to unloading affects the axial stress in the multilayer. The axial and shear stress in the structure post-unloading is also considered. In the following figures, unless otherwise stated, the critical normal and shear stress in the cohesive elements is equal to 200 MPa. Figure 6.13 shows a comparison of the axial stress in the multilayer film for perfectly bonded layers and cohesive elements at the Al/Si interface post-unloading for an indentation depth of 600 nm. Figure 6.13(a) shows the large axial tensile stress that extends through nearly every layer and into the substrate. Figure 6.13(b) shows that after damage has occurred, the volume of the multilayer subject to these high tensile stresses has decreased significantly. The large opening observed in Figure 6.13(b) is due to the unloading-induced tensile stress at the multilayer/substrate interface.

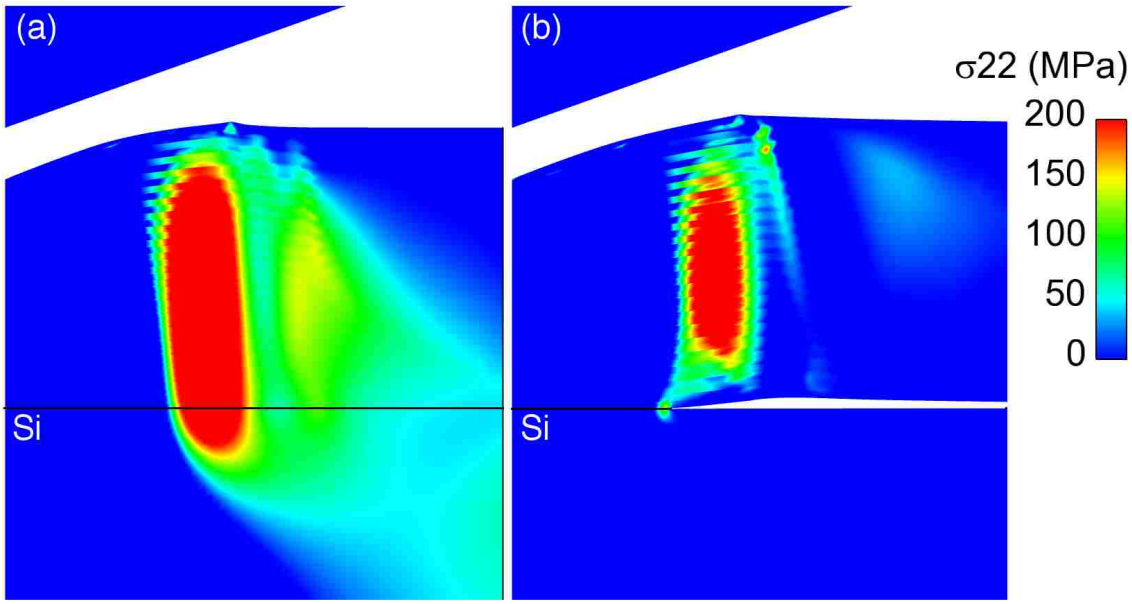

Figure 6.13: Axial stress (σ_{22}) in the multilayer Al/SiC post-unloading for an indentation depth of 600 nm for (a) perfectly bonded layers and (b) cohesive elements at the Al/Si interface.

Figure 6.14 shows the shear stress post-unloading for an indentation depth of 600 nm. The presence of a delamination at the Al/Si interface does not have a significant effect on the magnitude and distribution of shear stress in the structure. As discussed in the previous section, damage initiation and evolution is dominated by the axial (normal) stress at the Al/Si interface.

6.4 Conclusion

Delamination and void growth has been experimentally observed in Al/SiC multilayers subject to indentation loadings. Traditionally, the delamination and void growth is characterized post-indentation. The finite element method was used to study the effect delamination has on indentation-derived hardness and Young's modulus. Cohesive elements with a traction-separation relationship was used to facilitate delamination along

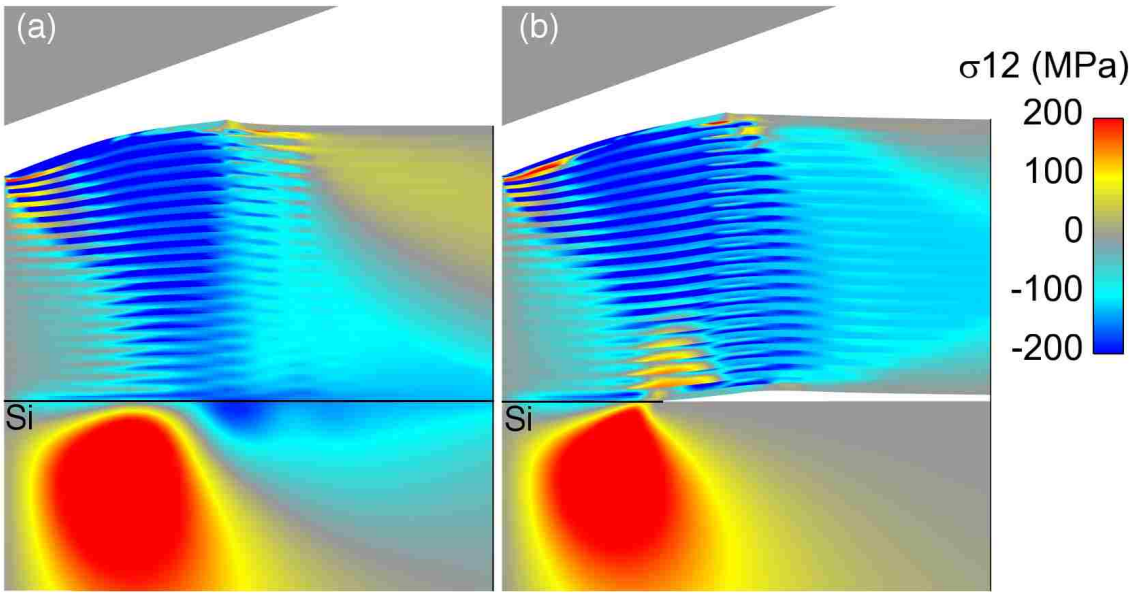

Figure 6.14: Shear stress (σ_{12}) in the multilayer Al/SiC post-unloading for an indentation depth of 600 nm for (a) perfectly bonded layers and (b) cohesive elements at the Al/Si interface.

material interfaces. A single-layer and multilayer film was considered. The single-layer Al film did not exhibit any delamination and the presence of cohesive elements did not adversely affect the indentation-derived variables. The multilayer Al/SiC model used cohesive elements at both the Al/Si and Al/SiC material boundaries. Delamination was observed numerically to be sensitive to the critical normal and shear stresses that define the cohesive traction-separation behavior. The load-displacement response of the multilayer film is not significantly different between perfectly bonded and cohesive material interfaces. This suggests that it may be difficult to experimentally observe delamination from solely load-displacement data.

Axial tensile stress was found to be the largest contributor to damage initiation and evolution. Delamination at the Al/Si interface resulted in a decrease in both indentation-derived hardness and Young's modulus, by as much as 22 and 27%, respectively. Hardness and Young's modulus decrease due to an increase in the

projected contact area and decrease in the contact stiffness at the onset of unloading. Interfacial sliding, facilitated by the presence of cohesive elements, causes a decrease in the axial stress throughout the structure. The decrease in axial stress contribute to changes in both the projected contact area and contact stiffness. Furthermore, a unique finding is that delamination may also occur during the unloading process of indentation, depending on the loading condition and critical tractions.

Chapter 7

Conclusions

Numerical and experimental studies have been performed to study the sensitivity of indentation-derived hardness and Young's modulus. Multilayer aluminum and silicon carbide films were studied in relation to their performance under indentation type loading. The thickness of each individual layer was assumed to be 50 nm with a thick Si substrate. It was shown that the multilayer has a much larger elastic modulus and hardness than homogeneous Al film. The multilayer film exhibits much more complex and interesting behavior than monolayer films.

Comparisons between multilayer Al/SiC and Al/SiO_2 films have been made. It was shown that the much stiffer and brittle SiC has a more significant effect than SiO_2 on the performance of the multilayer structure. Silicon dioxide, though brittle like SiC, has an elastic modulus similar to Al. During the unloading step of indentation, the softer SiO_2 does not provide the additional constraint on the Al that SiC does. Unloading-induced plasticity in the Al is also reduced when paired with SiO_2.

The mechanical behavior of thin films with undulating layers was considered. A multilayer film consisting of 61 undulating layers of alternating hard and soft material were subjected to overall uniaxial compressive loadings in the in-plane and

out-of-plane directions. The lateral (11 or parallel to the layers) and vertical (22 or perpendicular to the layers) loading resulted in quite different responses. It was shown that the presence of undulating layers does indeed affect the mechanical response of multilayer thin films.

Finite element models of alternating layers of Al/SiC on a Si substrate with undulating layer geometry were considered. The profile of each undulating layer was a regular waveform with wavelengths of 0.20, 0.40, and 0.67 μm and amplitudes of 12.5 and 25 nm. Two waveforms were used that were 180° out-of-phase of each other at the symmetry axis. It was shown that the variation in hardness and modulus is dependent on indentation depth and the phase of the waveform. The Young's modulus is most sensitive to the undulation frequency and amplitude at deep indentations. The presence of undulating geometry resulted in much more complex stress fields in both materials as well as enhanced unloading-induced plasticity in the metal layers. The increase in unloading-induced plasticity leads to greater uncertainty in the indentation-derived Young's modulus. The indentation-derived hardness and Young's modulus of the multilayer Al/SiC film was compared to existing experimental data of the same material system. Furthermore, due to the complexity of the local stress fields in the undulated layer geometry, there appears to be no unique correlation between uniaxial compression and indentation response. It is recommended that a series of indentations over an area of the specimen be conducted to gather sufficient data to reduce the effect of undulating layers.

The fundamental assumption of elastic indentation unloading was studied as it applies to multilayer thin films. It was shown that plasticity does increase in the Al during the unloading step, even during the initial unloading. The finite element method was used to model a purely elastic unloading event of the multilayer film. The difference between standard and enforced elastic unloading derived variables was presented. Through the parametric analysis the effect of unloading-induced

plasticity on indentation-measured modulus was quantified for the first time. For indentation depths greater than 500 nm, the standard and forced elastic unloading results differed by as much as 20%. Also, cyclic indentation was shown to alleviate the development of plastic strain during the initial unloading step. Based on these results, it is recommended that cyclic indentation be used for evaluating the indentation behavior of multilayer thin films.

Delamination has been observed experimentally in post-indentation SEM of the multilayer Al/SiC film. A model was created to elucide the effect of delamination on indentation-derived hardness and Young's modulus. Cohesive elements were used at the mulitlayer/substrate interface to provide a delamination mechanism. It was discovered that delamination is predominately driven by tensile axile stress at the multilayer/substrate interface. Both the hardness and Young's modulus of the film are sensitive to delamination, both of which decrease post-delamination. Delamination results in an increase in the projected contact area and a decrease in the contact stiffness at the onset of unloading. The axial stress throughout the film decreases significantly, both magnitude and distribution, after delamination occurs. The models prove that indentation-induced internal cracking can occur not just during unloading but unloading as well.

Chapter 8

Future Work

To gain a greater understanding of the imperfections of undulating geometry, it could be possible to study the surface waviness of sputtered aluminum through the controlled growth of grain sizes. Also, in the current study, the topmost Al surface was assumed flat. The effect this assumption, or lack of surface waviness, has on the indentation-derived variables is another possible extension of this study. Overall, greater uncertainty exists when using the indentation unloading response to determine the elastic modulus of multilayered thin-film composites. It was observed in this body of work that undulations can increase the distribution as well as magnitude of the EQPS in the metallic layers. It would be worthwhile to use the methods described in Chapter 5 to evaluate the effect of layer undulation plus unloading-induced plasticity on the indentation-derived Young's modulus. It is hypothesized that the undulations will lead to an increase in unloading-induced plasticity.

The primary method for investigation the multilayer film behavior in this dissertation has been the finite element method. A systematic experimental effort is a crucial step to better understand the multilayer film. Proposed experiments include quantifying the effects of material combination, thickness variations, film/substrate

combinations, and internal damage quantification through postmortem experimental visualization. Furthermore, performing cyclic indentation measurements to assess if the proposed methods in Chapter 5 generate the trend as predicted by modeling.

The delamination results shown in Chapter 6 are based traction-separation model parameters that merit further exploration. An expanded modeling effort, including a wider range of cohesive element parameters, can be used to determine if the finite element model can capture the experimentally observed cracking patterns. Furthermore, developing and implementing a more advanced damage initiation and evolution model for bulk Al and SiC would provide opportunity to study void nucleation and growth.

Appendices

Appendix A

Effect of Layer Thickness on Al/SiC Nanolaminates

The effect of SiC layer thickness on the indentation-derived mechanical properties of Al/SiC nanolaminates is evaluated using the finite element method. Lotfian et al. [63] has studied the layer thickness effect at various temperatures experimentally. To date, there has been no study of the effect of layer thickness using the finite element analysis. This analysis consists of five models, with Al/SiC thickness ratios ranging from 0.2 to 5.0. In all five models, the thickness of the Al layers are held constant and is 50 nm. The thickness of every SiC layer is 250 nm, 125 nm, 50 nm, 20 nm, and 10 nm (corresponding to thickness ratios of 0.2, 0.4, 1.0, 2.5, 5.0). Each model is loaded with the indenter described in Chapter 3 to depths from 100 nm to 1000 nm. Material properties and boundary conditions are the same as those used in previous models (3.2).

The finite element models of thickness ratios 2.5 and 5.0 (i.e. SiC thickness of 20 and 10 nm, respectively) failed to converge for indentation depths greater than 400 nm. The convergence failure is due to the vary thin layers of SiC. Thin layers of SiC begin

to buckle under indentation loading causing a bifurcation in the load-displacement response; therefore, leading to convergence difficulties. Lotfian [63] showed similar results for very thin layers of SiC. He showed that the SiC underwent substantial bending beneath the indenter. Though the thin SiC could generally sustain the large deformation, occasionally the SiC would fracture due to imposed shear.

The indentation-derived hardness for the multilayer Al/SiC film for a variety of thickness ratios is shown in Figure A.1. The trend is that as the SiC layer thickness increases, the hardness of the composite also increases. For thickness ratios greater than one, the SiC layers dominate the mechanical response of the film. For thickness ratios less than one, there is a mixed response. Shallow indentations show that the Al dominates the response. Past 200 nm, the thin SiC layers begin to contribute significantly to the hardness of the system.

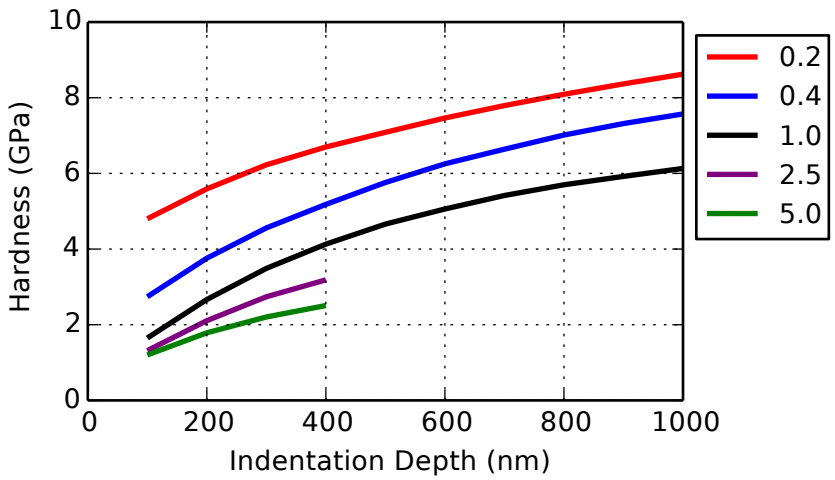

Figure A.1: Indentation-derived hardness of multilayer Al/SiC with varying Al-to-SiC thickness ratios.

Figure A.2 shows the indentation-derived Young's modulus for the multilayer Al/SiC film for a variety of thickness ratios. The elastic modulus of the series of thickness ratios is clearly dependent on the SiC volume fraction. As the thickness ratio decreases, the difference in predicted elastic modulus increases. The Young's

modulus of the system exhibits similar behavior to the hardness of the system, in regards to thickness ratios.

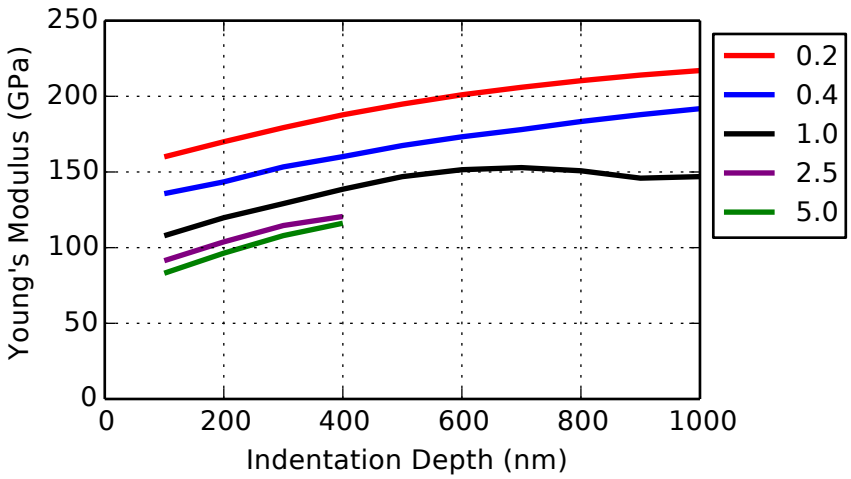

Figure A.2: Indentation-derived Young's modulus of multilayer Al/SiC with varying Al-to-SiC thickness ratios.

The unloading-induced plasticity at the top interface of the 10th layer of Al, 2 μm from the symmetry axis, is shown in Figure A.3 for indentation depth of 1000 nm. Only thickness ratios of 0.2, 0.4, and 1.0 are shown as thickness ratios greater than 1 did not converge at 1000 nm. At this location, the unloading-induced plasticity increases as the thickness of the SiC layers increase. During unloading, the mechanical constrain imposed by the thicker SiC result in a larger increase in plastic strain.

The increase in plasticity during unloading, as discussed in detail in Chapter 5, can affect the indentation-derived Young's modulus. Following the same procedure as outlined in Chapter 5, the indentation-derived Young's modulus was calculated for a perfectly *elastic* unloading step. The indentation-derived Young's modulus for both standard and enforced elastic unloading is shown in Figure A.4 for Al/SiC thickness ratios of 0.2, 1.0, and 5.0. In the figure, the solid lines represent the standard unloading result and the 'X' represent the enforced elastic unloading result.

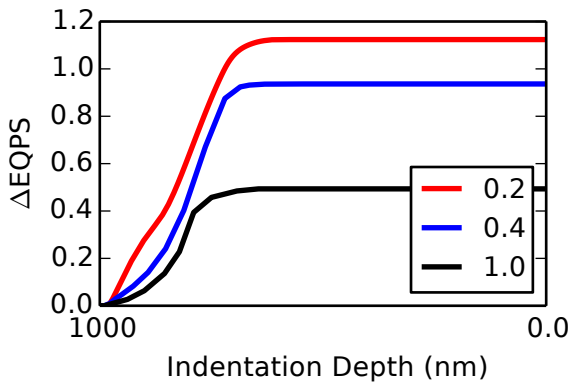

Figure A.3: Change in equivalent plastic strain (EQPS) during the unloading step for an indentation depth of 1000 nm.

For ratios greater than or equal to 1.0, the unloading-induced plasticity has little effect, particularly for indentation depths less than 600 nm. At indentation depths greater than 600 nm and for a thickness ratio of 1.0, there is significant difference in the derived Young's modulus (see Chapter 5 for further discussion on the differences for a ratio of 1.0). For a thickness ratio of 5.0, the difference in Young's modulus is insignificant. For a thickness ratio of 0.2 (SiC 5x as thick as Al), there is a measurable difference between the standard and enforced elastic unloading across the entire indentation range. The much thicker SiC layers effectively enforces a stronger constraint on the Al. During unloading, the thinner and softer Al must deform more to accommodate the much thicker SiC that remained elastic. It is this constraint on the Al from the SiC that causes the difference in derived modulus.

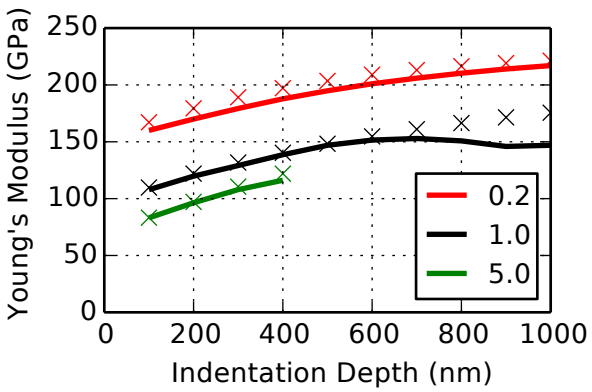

Figure A.4: Indentation-derived Young's modulus for both standard and enforced elastic unloading for various Al/SiC thickness ratios. The solid lines represent standard unloading and the 'X' represent enforced elastic unloading.

Appendix B

Experimental Study of Thin Film Aluminum and Silicon Carbide

The focus of this dissertation has been on using the finite element method to increase understanding of multilayer thin films. Though the simulations are able to provide valuable insight into the behavior of these composite materials, equally valuable information can be gleamed from fabrication of and experimentation on multilayer thin films. Efforts were made to fabricate and test monolayer Al and SiC films and multilayer Al/SiC films. This appendix will summarize the efforts as of March 2015 to fabricate and perform nanoindentation experiments on these films.

B.1 Thin Film Fabrication

Both Al and SiC films were deposited in monolayer and multilayer configurations. All Al and SiC samples were fabricated at the UNM Manufacturing Training and Technology Center (MTTC) clean rooms located in Albuquerque, NM. An AJA International, Inc. ATC Series Thin Film Deposition System was used for the

deposition. The Al and SiC layers were deposited by physical vapor deposition (magnetron sputtering) on a (1 1 1) Si substrate. The base pressure of the multi-gun sputtering chamber was 3.4 x 10^{-7} torr (4.5 x 10^{-4} Pa). Targets of pure Al (99.99%) and SiC (99.5%) provided by Kurt Lesker (Clairton, Pa) and were used for sputtering in an argon atmosphere, at an argon pressure of 3 mtorr(0.4 Pa). The Al was sputtered using a DC sputter gun while the SiC was sputtered using a RF sputter gun. Both the Al and SiC targets were presputtered to remove any surface oxide or other impurities. The Al was presputtered at 100 W for approximately 5 minutes and the SiC was presputtered at 200 W for approximately 5 minutes. Under these conditions, the deposition rates were 4.8 nm/min and 2.0 nm/min for Al and SiC, respectively. The deposition rate, and total thickness, as reported by the deposition system was verified using a Dektak stylus profilometer (Bruker Corp., Billerica, MA).

Four samples have been created to date. This includes a nominally 1 μm thick Al film, a nominally 1 μm thick SiC film, and two multilayer Al/SiC films. The first multilayer film was composed of seven alternating Al and SiC layers, each nominally 50 nm thick on a Si substrate. The second multilayer film was composed of 41 alternating Al and SiC layers, each 50 nm thick. Of these four samples, only the seven layer Al/SiC sample has been imaged prior to nanoindentation. Focused ion beam (FIB) and scanning electron microscopy (SEM) were used to inspect the cross-sectional and surface microstructure of the seven layer sample. A thin platinum layer was deposited on the sample prior to FIB machining to minimize ion beam damage.

The cross-section of the seven layer sample is shown in Figure B.1. The thickness of each layer is approximately 50 $\pm$ 10 nm. The layers exhibit significant amount of waviness, which increases away from the substrate. The waviness is believed to be caused by the deposition of polycrystalline Al [61]. The as-deposited Al has a columnar growth morphology, resulting in the observable roughness in both the materials. The SiC layer roughness follows that of the previously deposited Al [10].

To address the roughness of the deposited material, AJA suggests to maintain a plasma on both targets during the entire sputtering process, as opposed to striking plasma on a target only during deposition. To date, AJA suggestions have not been verified.

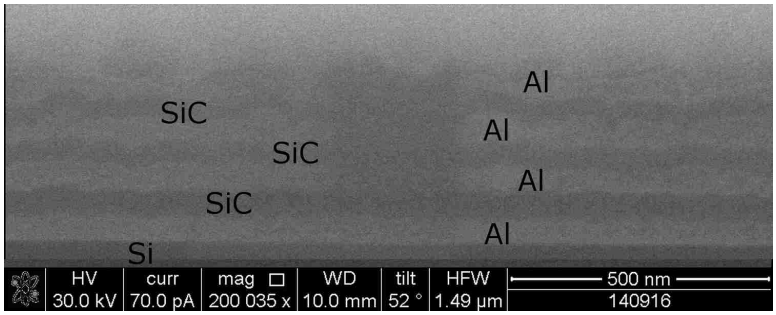

Figure B.1: SEM image of the FIB created cross-section of the seven layer Al/SiC multilayer film.

Figure B.2 shows the surface of the seven layer Al/SiC multilayer film at two magnification levels. The top layer of this multilayer sample is Al. The sputtered polycrystalline Al is porous. This may be contributed to high power levels and the porosity may be decreased by decreasing the sputtering power or decreasing chamber pressure.

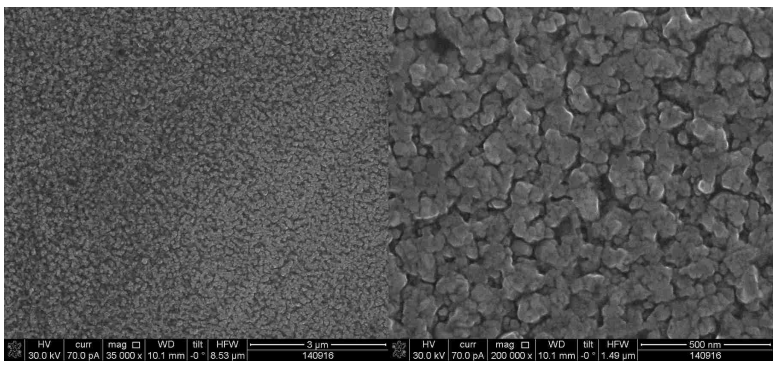

Figure B.2: SEM image of the surface layer of Al of the seven layer Al/SiC multilayer film at a resolution of 3 μm and 500 nm.

B.2 Experimental Nanoindentation

Nanoindentation experiments were performed on the Al and SiC monolayer films and the 41 layer Al/SiC film. The experiments were conducted using a NanoTest nanoindenter (Micro Materials, UK). A diamond Berkovich indenter was used for these experiments. The Young's modulus and hardness of the monolayer and multilayer films were calculated. The projected contact area used in these experiments was calculated from a 5^{th} degree polynomial from the diamond area function curves.

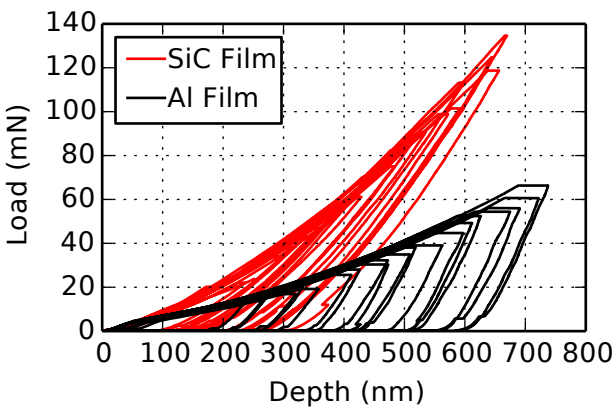

Figure B.3: Experimentally measured $P - h$ curves for Al and SiC monolayer films.

B.2.1 Monolayer Thin Films

Figure B.3 shows the measured load-displacement response for both monolayer Al and SiC films. As expected the measured load of the SiC film is much higher than the Al film. Also, the slope of the Al $P - h$ curve significantly changes at approximately 50 nm. The reason for this change is currently under investigation.

The experimentally derived hardness and Young's modulus for the monolayer Al and SiC films is shown in Figure B.4. Both of these samples are nominally 1.0 μm thick though this is yet to be verified. The Al film hardness is greater than expected

for sputtered Al (less than 1 GPa) [9]. The hardness of the SiC film is close to what is expected for sputtered SiC (20 GPa) [9]. The Young's modulus of both films is also different than expected. The modulus of the Al film is greater than expected and exhibits no substrate effect. The modulus of the SiC film is lower than expected based on the Young's modulus for sputtered SiC as reported in literature. Though both the hardness and modulus do not match the finite element results (Chapter 3) and reported values in literature [9, 61], the data is useful for gaining understanding into the actual geometry fabricated.

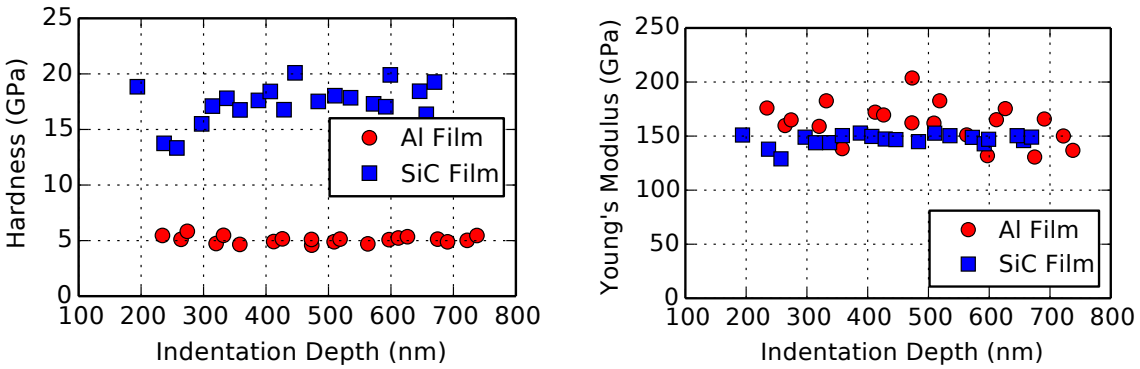

(a) Hardness

(b) Young's Modulus

Figure B.4: Experimentally derived hardness and Young's modulus of the Al and SiC monolayer films.

B.2.2 Multilayer Thin Films

A series of nanoindentation experiments were performed on the 41 layer Al/SiC sample. Indentation depth varied between 200 and 700 nm. Multiple measurements were made at each indentation depth (at different indentation sites). Each indentation site was sufficiently far from other indentation sites as not affect the local measurement. Additional cyclic indentation experiments were performed on this sample but the data is not included at this time.

The experimentally measured indentation-derived hardness and Young's modulus of the multilayer Al/SiC film, as well as finite element model results, are shown in Figure B.5. The hardness exhibits a small degree of substrate effect, as the hardness increases with indentation depth. The measured hardness is twice that of the predicted hardness from the model. The Young's modulus shown in the figure is not the reduced modulus as reported by the nanoindenter, it is the modulus of the specimen as calculated using Equation 2.7 with the same specimen Poisson's ratio and indenter properties as the finite element model. The measured Young's modulus shows good comparison to model data though the data is generally higher than the model results. Further study is underway to determine why the model and experimental data exhibit discrepancies. It is believed that the layer thickness may not be accurate for the fabricated geometry, causing the discrepancy between model and data.

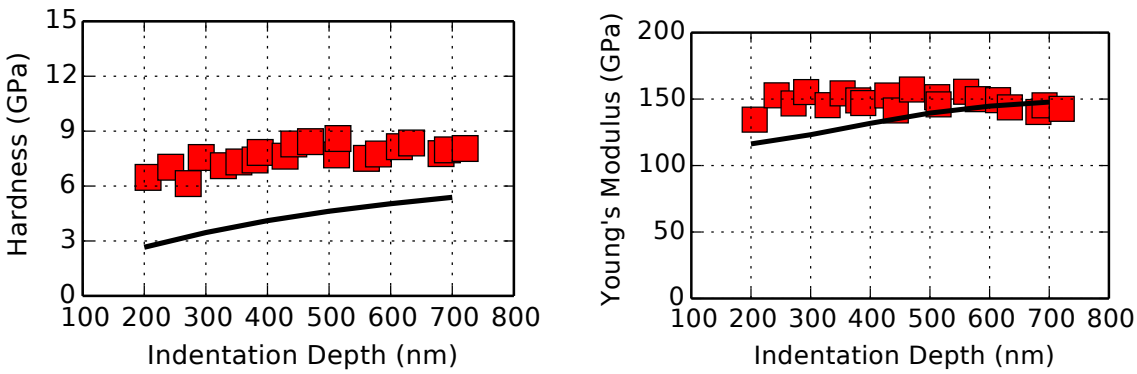

(a) Hardness

(b) Young's Modulus

Figure B.5: Experimentally derived hardness and Young's modulus of the multilayer Al/SiC film with 41 layers. The squares represent experimental data and the solid line represents finite element model results.

References

[1] A. Alpas, J. Embury, D. Hardwick, and R. Springer, "The mechanical properties of laminated microscale composites of Al/Al_2O_3," *Journal of Materials Science*, vol. 25, no. 3, pp. 1603–1609, 1990.

[2] T. C. Chou, T. G. Nieh, T. Y. Tsui, G. M. Pharr, and W. C. Oliver, "Mechanical properties and microstructures of metal/ceramic microlaminates: Part I. $Nb/MoSi_2$ systems," *Journal of Materials Research*, vol. 7, pp. 2765–2773, Oct 1992.

[3] T. C. Chou, T. G. Nieh, T. Y. Tsui, G. M. Pharr, and W. C. Oliver, "Mechanical properties and microstructures of metal/ceramic microlaminates: Part II. a $Mo/A1_2O_3$ systems," *Journal of Materials Research*, vol. 7, pp. 2774–2784, Oct 1992.

[4] C. H. Liu, W.-Z. Li, and H.-D. Li, "TiC/metal nacrous structures and their fracture toughness increase," *Journal of Materials Research*, vol. 11, pp. 2231–2235, Sep 1996.

[5] M. B. Daia, P. Aubert, S. Labdi, C. Sant, F. A. Sadi, P. Houdy, and J. L. Bozet, "Nanoindentation investigation of Ti/TiN multilayer films," *Journal of Applied Physics*, vol. 87, no. 11, pp. 7754–7757, 2000.

[6] J. H. Lee, W. M. Kim, T. S. Lee, M. K. Chung, B. ki Cheong, and S. G. Kim, "Mechanical and adhesion properties of A1/A1N multilayered thin films," *Surface and Coatings Technology*, vol. 133-134, pp. 220–226, 2000.

[7] M. A. Phillips, B. M. Clemens, and W. D. Nix, "Microstructure and nanoindentation hardness of Al/Al_3Sc multilayers," *Acta Materialia*, vol. 51, pp. 3171–3184, Jun 2003.

[8] J. Romero, A. Lousa, E. Martinez, and J. Esteve, "Nanometric chromium/chromium carbide multilayers for tribological applications," *Surface and Coatings Technology*, vol. 163-164, pp. 392–397, Jan 2003.

[9] X. Deng, C. Cleveland, T. Karcher, M. Koopman, N. Chawla, and K. K. Chawla, "Nanoindentation behavior of nanolayered metal-ceramic composites," *Journal of Materials Engineering and Performance*, vol. 14, pp. 417–423, Aug 2005.

[10] N. Chawla, D. R. P. Singh, Y.-L. Shen, G. Tang, and K. K. Chawla, "Indentation mechanics and fracture behavior of metal/ceramic nanolaminate composites," *Journal of Materials Research*, vol. 43, pp. 4383–4390, Jul 2008.

[11] D. Bhattacharyya, N. A. Mara, P. Dickerson, R. G. Hoagland, and A. Misra, "Compressive flow behavior of al-tin multilayers at nanometer scale layer thickness," *Acta Materialia*, vol. 59, pp. 3804–3816, June 2011.

[12] P. L. Sun, J. P. Chu, T. Y. Lin, Y.-L. Shen, and N. Chawla, "Characterization of nanaindentation damage in metal/ceramic multilayered films by transmission electron microscopy (TEM)," *Materials Science and Engineering A*, vol. 527, pp. 2985–2992, May 2010.

[13] M. Parlinska-Wojtan, S. Meier, and J. Patscheider, "Transmission electron microscopy characterization of TiN/SiNx multilayered coatings plastically deformed by nanoindentation," *Thin Solid Films*, vol. 518, no. 17, pp. 4890 – 4897, 2010.

[14] D. Wang, T. Kups, J. Schawohl, and P. Schaaf, "Deformation behavior of au/ti multilayers under indentation," *Journal of Materials Science: Materials in Electronics*, vol. 23, no. 5, pp. 1077–1082, 2012.

[15] W. C. Oliver and G. M. Pharr, "An improved technique for determining hardness and elastic modulus using load and displacement sensing indentation experiments," *Journal of Materials Research*, vol. 7, pp. 1564–1583, Jan. 1992.

[16] G. M. Pharr and A. Bolshakov, "Understanding nanoindentation unloading curves," *Journal of Materials Research*, vol. 17, pp. 2660–2671, Oct. 2002.

[17] G. Tang, Y.-L. Shen, D. R. P. Singh, and N. Chawla, "Indentation behavior of metalceramic multilayers at the nanoscale: Numerical analysis and experimental verification," *Acta Materialia*, vol. 58, no. 6, pp. 2033–2044, 2010.

[18] D. R. P. Singh, N. Chawla, and Y.-L. Shen, "Focused ion beam (FIB) tomography of nanoindentation damage in nanoscalee metal/ceramic multilayers," *Materials Characterization*, vol. 61, pp. 481–488, 2010.

[19] Y.-L. Shen, C. B. Blada, J. J. Williams, and N. Chawla, "Cyclic indentation behavior of metal-ceramic nanolayered composites," *Materials Science and Engineering A*, vol. 557, pp. 119–125, Nov 2012.

[20] J. V. Boussinesq, *Application des potentiels à l'étude de l'équilibre et du mouvement des solides élastiques*. France: Gauthier-Villars, 1885.

[21] H. Hertz, "On the contact of firm elastic bodies," *Journal für die Reine Angewandte Mathematik*, vol. 92, pp. 156–171, 1882.

[22] I. N. Sneddon, "The relation between load and penetration in the axisymmetric boussinesq problem for a punch of arbitrary profile," *International Journal of Engineering Science*, vol. 3, pp. 47–57, Aug. 1965.

[23] G. I. Pogodin-Alekseyev, "The modulus of indentation and hardness number determined by indentation with a pyramid," *Metal Science and Heat Treatment of Metals*, vol. 4, no. 7-8, pp. 352–353, 1962.

[24] M. F. Doerner and W. D. Nix, "A method for interpreting the data from depth-sensing indentation instruments," *Journal of Materials Research*, vol. 1, pp. 601–609, 1986.

[25] J. B. Pethica, R. Hutchings, and W. C. Oliver, "Hardness measurement at penetration. depths as small as 20 nm," *Philosophical Magazine*, vol. A48, pp. 593–606, 1983.

[26] W. C. Oliver, R. Hutchings, and J. B. Pethica, "Measurement of hardness at indentation depths as low as 20 nanometres," *ASTM STP 889*, pp. 90–108, 1986.

[27] A. Bolshakov and G. M. Pharr, "Inaccuracies in sneddon's solution for elastic indentation by a rigid cone and their implications for nanoindentation data analysis," in *Symposium CC Thin Films Stresses and Mechanical Properties VI*, vol. 436 of *MRS Proceedings*, 1996.

[28] J. C. Hay, A. Bolshakov, and G. M. Pharr, "A critical examination of the fundamental relations used in the analysis of nanoindentation data," *Journal of Materials Research*, vol. 14, pp. 2296–2305, June 1999.

[29] D. Tabor, "A simple theory of static and dynamic hardness," *Proceedings of the Royal Society of London A: Mathematical, Physical and Engineering Sciences*, vol. 192, no. 1029, pp. 247–274, 1948.

[30] N. A. Stilwell and D. Tabor, "Elastic recovery of conical indentations," *Proceedings of the Physical Society*, vol. 78, no. 2, p. 169, 1961.

[31] A. Bolshakov, W. C. Oliver, and G. M. Pharr, "An explanation for the shape of nanoindentation unloading curves based on finite element simulation," in *Symposium B2 Thin Films: Stresses and Mechanical Properties V*, vol. 356 of *MRS Proceedings*, 1994.

[32] W. C. Oliver and G. M. Pharr, "Measurement of hardness and elastic modulus by instrumented indentation: Advances in understanding and refinements to methodology," *Journal of Materials Research*, vol. 19, pp. 3–20, Jan. 2004.

[33] G. M. Pharr and W. C. Oliver, "Measurement of thin film mechanical properties using nanoindentation," *MRS Bulletin*, pp. 28–33, Jul 1992.

[34] A. J. Whitehead and T. F. Page, "Nanoindentation studies of thin film coated systems," *Thin Solid Films*, vol. 220, pp. 277–283, Nov 1992.

[35] Z. Wei, G. Zhang, H. Chen, J. Luo, R. Liu, and S. Guo, "A simple method for evaluating elastic modulus of thin films by nanoindentation," *Journal of Materials Research*, vol. 24, pp. 801–815, Mar 2009.

[36] B. Zhou and B. C. Prorok, "A discontinuous elastic interface transfer model of thin film nanoindentation," *Experimental Mechanics*, vol. 50, pp. 973–801, Jul 2010.

[37] B. C. P. B. Zhou, "A new paradigm in thin film indentation," *Journal of Materials Research*, vol. 25, pp. 1671–1678, Sep 2010.

[38] W. C. Oliver and G. M. Pharr, "Nanoindentation in materials research: past, present, and future," *MRS Bulletin*, vol. 35, pp. 897–907, Nov 2010.

[39] T. Saraswati, T. Sridharan, S. Mhaisalkar, C. D. Breach, and F. Wulff, "Cyclic loading as an extended nanoidentation technique," *Materials Science and Engineering A*, vol. 423, pp. 14–18, 2006.

[40] A. Tekaya, S. Labdi, and T. Benameur, "Quasi-static cyclic loadings induced inelastic deformation in a Zr-based bulk metallic glass under nanindentation," *Journal of Materials Science*, vol. 44, no. 18, pp. 4930–4938, 2009.

[41] A. Tekaya, H. A. Ghulman, T. Benameur, and S. Labdi, "Cyclic nanoindentation and finite element analysis of Ti/TiN and CrN nanocoatings on Zr-based metallic glasses mechanical performance," *Journal of Materials Engineering and Performance*, vol. 23, pp. 4259–4270, Dec 2014.

[42] W. R. LaFontaine, C. A. Paszkiet, M. A. Korhonen, and C.-Y. Li, "Residual stress measurements of thin aluminum metallizations by continuous indentation

and X-ray stress measurement techniques," *Journal of Materials Research*, vol. 6, pp. 2084–2090, 1991.

[43] G. M. Pharr, T. Y. Tsui, A. Bolshakov, and W. C. Oliver, "Effects of residual stress on the measurement of hardness and elastic modulus using nanoindentation," in *Symposium Materials Reliability in Microelectronics IV*, vol. 338 of *MRS Proceedings*, 1994.

[44] T. Y. Tsui, W. C. Oliver, and G. M. Pharr, "Influences of stress on the measurement of mechanical properties using nanoindentation: Part I. Experimental studies in an aluminum alloy," *Journal of Materials Research*, vol. 11, pp. 752–759, 1996.

[45] A. Bolshakov, W. C. Oliver, and G. M. Pharr, "Influences of stress on the measurement of mechanical properties using nanoindentation: Part II. Finite element simulations," *Journal of Materials Research*, vol. 11, pp. 760–768, Mar. 1996.

[46] D. R. P. Singh, X. Deng, N. Chawla, J. Bai, C. Hubbard, T. G, and Y.-L. Shen, "Residual stress characterization of Al/SiC nanoscale multilayers using X-ray synchrotron radiation," *Thin Solid Films*, vol. 519, pp. 759–765, 2010.

[47] G. Constantinides, K. S. R. Chandran, F.-J. Ulm, and K. J. V. Vliet, "Grid indentation analysis of composite microstructure and mechanics: Principles and validation," *Materials Science and Engineering A*, vol. 430, pp. 189–202, Aug. 2006.

[48] P. Trtik, B. Munch, and P. Lura, "A critical examination of statistical nanoindentation on model materials and hardened cement pastes based on virtual experiments," *Cement & Concrete Composites*, vol. 31, p. 705714, 2009.

[49] E. Martnez, J. Romero, A. Lousa, and J. Esteve, "Nanoindentation stress strain curves as a method for thin-film complete mechanical characterization: application to nanometric CrN/Cr multilayer coatings," *Applied Physics A*, vol. 77, no. 3-4, pp. 419–427, 2003.

[50] Y. Ma, Y. Zhang, H.-f. Yu, X.-y. Zhang, X.-f. Shu, and B. Tang, "Plastic characterization of metals by combining nanoindentation test and finite element simulation," *Transactions of Nonferrous Metals Society of China*, vol. 23, pp. 2368–2373, 2013.

[51] S. Liu, J. H. Huang, and Y. Gu, "Deconvolution of mechanical properties of thin films from nanoindentation measurement via finite element optimization," *Thin Solid Films*, vol. 526, pp. 183–190, 2012.

[52] M. S. Kashani, *Sources of error in relating nanoindentation results to material properties*. Doctoral dissertation, Wichita State University, Wichita, KS, USA, May 2010.

[53] J. Plücker, "Observations on the electrical discharge through rarefied gases," *The London Edinburgh and Dublin Philosphical Magazine*, vol. 16, p. 409, 1858.

[54] M. A. Meyers, P.-Y. Chen, A. Y.-M. Lin, and Y. Seki, "Biological materials: Structure and mechanical properties," *Progress in Materials Science*, vol. 53, pp. 1–206, Jan 2008.

[55] C. 73, "Nautiluscutawaylogarithmicspiral." `http://commons.wikimedia.org/wiki/File:NautilusCutawayLogarithmicSpiral.jpg#mediaviewer/File:NautilusCutawayLogarithmicSpiral.jpg`.

[56] L. Holland, *Vacuum Deposition of Thin Films*. New York, USA: John Wiley, 1956.

[57] C. F. Powell, J. H. Oxley, and J. John M. Blocher, *Vapor deposition*. New York, USA: John Wiley, 1966.

[58] "Sputtering.gif." `http://en.wikipedia.org/wiki/File:Sputtering.gif`.

[59] M. A. E. Khakani, M. Chaker, A. Jean, S. Boily, and J. C. Kieffer, "Hardness and Youngs modulus of amorphous α-SiC thin films determined by nanoindentation and bulge tests," *Journal of Materials Research*, vol. 9, pp. 96–103, Jan. 1994.

[60] D. L. Windt and J. A. Bellotti, "Performance, structure, and stability of sic/al multilayer films for extreme ultraviolet applications," *Applied Optics*, vol. 48, pp. 4932–4941, Sep 2009.

[61] X. Deng, N. Chawla, K. K. Chawla, M. Koopman, and J. P. Chu, "Mechanical behavior of multilayered nanoscale metal-ceramic composites," *Advanced Engineering Materials*, vol. 7, pp. 1099–1108, Dec 2005.

[62] G. Tang, Y.-L. Shen, D. R. P. Singh, and N. Chawla, "Analysis of indentation-derived effective elastic modulus of metal-ceramic multilayers," *International Journal of Mechanics and Materials in Design*, vol. 4, no. 4, pp. 391–398, 2008.

[63] S. Lotfian, C. Mayer, N. Chawla, J. Llorca, A. Misra, J. K. Baldwin, and J. M. Molina-Aldareguia, "Effect of layer thickness on the high temperature mechanical properties of Al/SiC nanolaminates," *Thin Solid Films*, vol. 571, pp. 260–267, Nov 2014.

[64] D. R. P. Singh and N. Chawla, "Scratch resistance of Al/SiC metal/ceramic nanolaminates," *Journal of Materials Research*, vol. 27, pp. 278–283, Jan 2012.

[65] F.-L. Wen and Y.-L. Shen, "Plastic deformation in multilayered thin films during indentation unloading: a modeling analysis incorporating viscoelastic response," *Mechanics of Time-Dependent Materials*, vol. 15, no. 3, pp. 277–291, 2011.

[66] X. Luo, G. Qian, and E. G. Wang, "Molecular-dynamics simulation of Al/SiC interface structures," *Physical Review B*, vol. 59, pp. 10 125–10 131, Apr 1999.

[67] C. R. Dandekar and Y. C. Shin, "Molecular dynamics based cohesive zone law for describing Al-SiC interface mechanics," *Composites: Part A Applied Science and Manufacturing*, vol. 42, pp. 355–363, Apr 2011.

[68] K. Gall, M. F. Horstemeyer, M. V. Schilfgaarde, and M. I. Baskes, "Atomistic simulations on the tensile debonding of an aluminum-silicon interface," *Journal of the Mechanics and Physics of Solids*, vol. 48, pp. 2183–2212, Oct 2000.

[69] C. R. Dandekar and Y. C. Shin, "Effect of porosity on the interface behavior of an Al_2O_3-aluminum composite: A molecular dynamics study," *Composites Science and Technology*, vol. 71, pp. 350–356, Feb 2011.

[70] G. Liu, A. Mouftiez, J. Lesage, and S. Panier, "A numerical fracture analysis of a stationary semi-circular interface crack during interfacial indentation test," *Surface and Coatings Technology*, vol. 201, pp. 2086–2091, Oct 2006.

[71] Y. Y. Sheng, "A simulation by using cohesive zone model for indentation test in thin-film/substrate systems," master of engineering, National University of Singapore, Singapore, 2007.

[72] C. C. Tasan, J. P. M. Hoefnagels, and M. G. D. Geers, "Indentation-based damage quantification revisited," *Scripta Materilia*, vol. 63, pp. 316–319, Oct. 2010.

[73] P. Wiecinski, J. Smolik, H. Garbacz, and K. J. Kurzydlowski, "Failure and deformation mechanisms during indentation in nanoscructured Cr/CrN multilayer coatings," *Surface and Coatings Technology*, vol. 240, pp. 23–31, Feb 2014.

[74] J. Chen and S. J. Bull, "Finite element analysis of contact induced adhesion failure in multilayer coatings with weak interfaces," *Thin Solid Films*, vol. 517, pp. 3704–3711, May 2009.

[75] J. M. Mook, R. Raghavan, J. K. Baldwin, D. Frey, J. Michler, N. A. Mara, and A. Misra, "Indentation fracture response of Al-TiN nanolaminates," *Materials Research Letters*, vol. 1, no. 2, pp. 102–108, 2013.

[76] S. Nekkanty, *Characterization of damage & optimization of thin film coatings on ductile substrates*. Doctoral dissertation, The Ohio State University, Columbus, OH, USA, 2009.

[77] K. R. Morasch, "Nanoindentation induced thin film fracture," master of science in materials science and engineering, Washington State University, Pullman, WA, USA, May 2005.

[78] A. Needleman, "A continuum model for void nucleation by inclusion debonding," *Journal of Applied Mechanics*, vol. 54, pp. 525–531, Sep 1987.

[79] V. Tvergaard and J. W. Hutchinson, "The relation between crack growth resistance and fracture process parameters in elastic-plastic solids," *Journal of the Mechanics and Physics of Solids*, vol. 40, pp. 1377–1397, Aug 1992.

[80] K. Park and G. H. Paulino, "Cohesive zone models: A critical review of traction-separation relationships across fracture surfaces," *Applied Mechanics Reviews*, vol. 64, pp. 060802–060802, 02 2013.

[81] A. Hillerboerg, M. Modeer, and P.-E. Petersson, "Analysis of crack formation and crack growth in concrete by means of fracture mechanics and finite elements," *Cement and Concrete Research*, vol. 6, pp. 773–781, Nov 1976.

[82] A. C. Fischer-Cripps, *Nanoindentation*. New York, USA: Springer, 2002.

[83] D. R. Lide, *Handbook of Chemistry and Physics*. Florida, USA: CRC, 76 ed., 1995.

[84] J.-L. Bucaille, S. Stauss, P. Schwaller, and J. Michler, "A new technique to determine the elastoplastic properties of thin metallic films using sharp indenters," *Thin Solid Films*, vol. 447448, no. 0, pp. 239 – 245, 2004. Proceedings of the 30th International Conference on Metallurgical Coatings and Thin Films.

[85] F. Maseeh, S. M. Gelston, and S. D. Senturia, "Properties of microelectronic silicon dioxide (SiO_2)," VLSI Memo 89-575, Massachusetts Institute of Technology, Cambridge, MA, USA, 1989.

[86] S. S. Choi, J. S. Kim, H. S. Cha, J. M. Park, J. Ahn, J. H. Jo, H. B. Chung, S. Chang, and B. W. Kim, "A novel anti-reflective structure with Al/SiO_2 stack films for metal layer patterning," *Journal of the Korean Physical Society*, vol. 33, pp. 104–107, 1998.

[87] I. Knorr, N. M. Cordero, E. T. Lilleodden, and C. A. Volkert, "Mechanical behavior of nanoscale Cu/PdSi multilayers," *Acta Materialia*, vol. 61, no. 13, pp. 4984 – 4995, 2013.

[88] G. Tang, D. R. P. Singh, Y.-L. Shen, and N. Chawla, "Elastic properties of metalceramic nanolaminates measured by nanoindentation," *Materials Science and Engineering: A*, vol. 502, no. 12, pp. 79 – 84, 2009.

[89] R. D. Jamison and Y.-L. Shen, "Indentation behavior of multilayered thin films: Effects of layer undulation," *Thin Solid Films*, vol. 570, Part B, no. 0, pp. 235 – 242, 2014. TACT 2013 International Thin Films Conference.

[90] Y.-L. Shen, *Constrained Deformation of Materials*. New York, USA: Springer, 2010.

[91] R. W. Cahn, *The Coming of Materials Science*. Oxford, England: Pergamon Press, 5th ed., 2001.

[92] V. J. Laraia and A. H. Heuer, "Novel composite microstructure and mechanical behavior of mollusk shell," *Journal of the American Ceramic Society*, vol. 72, no. 11, pp. 2177–2179, 1989.

[93] S. Ko, T. Dechakupt, C. A. Randall, S. Trolier-McKinstry, M. Randall, and A. Tajuddin, "Chemical solution deposition of copper thin films and integration into a multilayer capacitor structure," *Journal of Electroceramics*, vol. 24, no. 3, pp. 161–169, 2010.

[94] T. Koseki, J. Inoue, and S. Nambu, "Development of multilayer steels for improved combinations of high strength and high ductility," *Materials Transactions*, vol. 55, no. 2, pp. 227–237, 2014.

[95] Y. Sahin, "The effects of various multilayer ceramic coatings on the wear of carbide cutting tools when machining metal matrix composites," *Surface and Coatings Technology*, vol. 199, no. 1, pp. 112 – 117, 2005.

[96] L. Ghalandari and M. M. Moshksar, "High-strength and high-conductive Cu/Ag multilayer produced by ARB," *Journal of Alloys and Compounds*, vol. 506, no. 1, pp. 172 – 178, 2010.

[97] A. A. Voevodin, J. M. Schneider, C. Rebholz, and A. Matthews, "Multilayer composite ceramic-metal-DLC coatings for sliding wear applications," *Tribology International*, vol. 29, no. 7, pp. 559–570, 1996.

[98] M. P. Schmitt, A. K. Rai, R. Bhattacharya, D. Zhu, and D. E. Wolfe, "multilayer thermal barrier coating TBC architectures utilizing rare earth doped YSZ and rare earth pyrochlores," *Surface and Coatings Technology*, vol. 251, no. 0, pp. 56 – 63, 2014.

[99] A. Ziani, F. Delmotte, C. L. Paven-Thivet, E. Meltchakov, A. Jérome, M. Roulliay, F. Bridou, and K. Gasc, "Ion beam sputtered aluminum based multilayer mirrors for extreme ultraviolet solar imaging," *Thin Solid Films*, vol. 552, no. 0, pp. 62 – 67, 2014.

[100] S. Lotfian, M. Rodrguez, K. E. Yazzie, N. Chawla, J. Llorca, and J. M. Molina-Aldareguía, "High temperature micropillar compression of Al/SiC nanolaminates," *Acta Materialia*, vol. 61, no. 12, pp. 4439 – 4451, 2013.

[101] Y.-C. Wang, A. Misra, and R. G. Hoagland, "Fatigue properties of nanoscale Cu/Nb multilayers," *Scripta Materialia*, vol. 54, no. 9, pp. 1593 – 1598, 2006.

[102] A. S. Budiman, S.-M. Han, N. Li, Q.-M. Wei, P. Dickerson, N. Tamura, M. Kunz, and A. Misra, "Plasticity in the nanoscale Cu/Nb single-crystal multilayers as revealed by synchrotron laue X-ray microdiffraction," *Journal of Materials Research*, vol. 27, pp. 599–611, 2012.

[103] B. A. Galanov, O. N. Grigor'ev, Y. V. Mil'man, and I. P. Ragozin, "Determination of the hardness and Young's modulus from the depth of penetration of a pyramidal indentor," *Strength of Materials*, vol. 15, no. 11, pp. 1624–1628, 1983.

[104] R. D. Jamison and Y.-L. Shen, "Indentation and overall compression behavior of multilayered thin-film composites: Effect of undulating layer geometry," *Journal of Composite Materials*, 2015.

[105] S. Suresh, *Fatigue of Materials*. Cambridge, England: Cambridge University Press, 1998.

[106] T. Diehl, "Modeling surface-bonded structures with ABAQUS cohesive elements: Beam-type solutions," in *ABAQUS Users Conference*, 2005.